UNIVERSITY OF CALIFORNIA

Los Angeles

High-throughput analysis of single-cell force biology

A dissertation submitted in partial satisfaction

of the requirements for the degree

Doctor of Philosophy in Bioengineering

by

Ivan Pushkarsky

2017

ABSTRACT OF THE DISSERTATION

High-throughput analysis of single-cell force biology

by

Ivan Pushkarsky

Doctor of Philosophy in Bioengineering

University of California, Los Angeles, 2017

Professor Dino Di Carlo, Chair

Mechanical forces generated by cells play important functional roles within many physiological systems such as regulating local vascular resistance, producing cardiac contractions, and propelling intestinal contents. As a result, a multitude of disorders can be caused directly by malfunctioning cellular force generation including chronic conditions such as asthma, hypertension, and bowel disease. Such disorders place a significant burden on patient health and there is a paucity of effective drugs, arguably due to a lack of adequate tools for evaluating cellular force in research or in early drug discovery.

Existing approaches to measure cellular forces have been largely limited to biological research settings. Of these, the most widely used are traction force microscopy (TFM) and elastomeric micropost arrays (EMA). Although both approaches are useful for probing specific sub-cellular forces at low yields (usually 10s of cells per experiment), they were not intended to be used as high-throughput tools for rapidly conducting extensive pharmacological testing and have not been adopted by pharmaceutical companies for drug discovery. Specific barriers to adoption of such technologies include their relatively low throughput, complex experimental

procedures which are difficult to automate, and minimal control over cell morphologies which necessitates intensive, non-trivial data analysis and normalization. Production of these systems and their physical characteristics also complicate or entirely prevent integration with standard SLAS well-plate formats.

We developed a high-throughput phenotypic screening platform that met this need by measuring the relative strains induced by the contractile forces generated by up to 10^5 single-cells adhered to large arrays of elastomeric surface sensors. The method supports analysis of a variety of force-generating behaviors in both a standalone and the multiwell formats used for drug-discovery. This dissertation describes the fabrication of these novel substrates, provides several use-cases including studies of smooth muscle or cardiac muscle force biology at the single-cell level, and provides novel biological data regarding the phagocytic forces of individual human macrophages.

We conclude by demonstrating the integration of the platform into standard 96- and 384-wellplates and verify its feasibility as a drug discovery tool by performing a pilot high-throughput screen to identifying potential bronchodilatory compounds for asthma management. These results indicate this platform could aid in the discovery of not only new therapeutic compounds, but also of novel molecular mechanisms associated with disease.

The dissertation of Ivan Pushkarsky is approved.

Sherie L. Morrison

James Dunn

Song Li

Dino Di Carlo, Committee Chair

University of California, Los Angeles

2017

DEDICATION

To my mother.

In lieu of participating in Commencement, it's the least I can do…

TABLE OF CONTENTS

ACKNOWLEDGEMENTS

Chapter 1 is an adaptation of the introduction to Chapter 3.

Chapter 2 *Metallization and Biopatterning on Ultra-Flexible Substrates via Dextran Sacrificial Layers* has been reprinted with adaptions with permission from (Tseng, P., Pushkarsky, I. & Carlo, D. D. Metallization and Biopatterning on Ultra-Flexible Substrates via Dextran Sacrificial Layers. *PLOS ONE* 9, e106091 (2014).) Conceived and designed the experiments: PT DD. Performed the experiments: PT IP. Analyzed the data: PT IP. Contributed reagents/materials/analysis tools: DD. Contributed to the writing of the manuscript: PT IP DD.

Chapter 3 is a version of the work *Elastomeric sensor surfaces for high-throughput single-cell force biology* submitted for publication by Pushkarsky *et al.* to Nature Biomedical Engineering in April 2017 (In review at the time of this writing). I.P. and P.T. contributed equally to this work. P.T and D.D. conceived the method. I.P., R.D., P.O., S.M., and D.D. designed experiments. I.P. performed all experiments, developed the multi-well embodiment, optimized protocols, and wrote the image analysis software. D.B. assisted in substrate preparation and macrophage differentiation procedures. R.T. maintained chimeric antibody stocks. S.M. supplied all chimeric antibodies. J.L. constructed the finite element method model. R.D. supplied HTS equipment for dose-response experiments and provided technical advice on HTS procedures and on developing the multi-well plate embodiment. B.F assisted with HTS equipment and drug administration. P.O. performed MDC differentiation and advised experimental procedures. I.P., R.D., P.O., S.M., and D.D. interpreted the results. I.P. and D.D. wrote the manuscript.

ACKNOWLEDGEMENTS

Chapter 4 Contains sections reprinted with permission from the work (*Koziol-White, C. J. et al. Inhibition of PI3K promotes dilation of human small airways in a rho kinase-dependent manner. Br. J. Pharmacol. (2016). doi:10.1111/bph.13542*) C.J.K.W., E.J.Y., G.C., I.P., R.D.D., S.B.L., R.C.K., R.A.P.J and D.D.C. contributed to the experimental design. C.J.K.W., E.J.Y., G.C., J.Z., E.P., I.P., A.A. and R.C.K. performed experiments. C.J.K.W., E.J.Y., G.C., J.Z., E.P., I.P., A.A., B.E.H. and R.C.K. analysed the data. C.J.K.W. wrote the manuscript. E.J.Y., R.D.D., S.B.L., R.C.K., R.A.P.J and D.D.C. edited the manuscript. I.P. wrote a portion of the manuscript.

Chapter 5 contains sections from a work in preparation by Pushkarsky *et al.* entitled *High-throughput phenotypic screening of single-cell force generation.*

Additional Acknowledgements:

I owe especially great thanks to the following individuals without whose help I would not be in this position:

To Prof. Peter Tseng,
for laying the foundations of my project, as well as for heavy doses of badly needed tough love, alongside invaluable training and direction. There is no one better to learn the *art of lab* from.

To Prof. Robert Damoiseaux,
for providing on-demand expertise as well as hands-on efforts while we got this work off the ground. Looking forward to many more years of progress!

To Dr. Westbrook Weaver,
for teaching by example how to *own your work,* for my first taste of professional confidence, and always *keeping it 100* through continued friendship and support.

To Dr. Coleman Murray,
for being the older brother figure I've needed to stay in line and grow in maturity, always leading by example.

and most of all,

To Prof. Dino Di Carlo,
For providing more opportunities than I ever hoped for or deserved. I only hope you're starting to see returns on your many investments.

I've also been lucky enough to have built relationships with the following colleagues, and in many cases, friends (in no particular order):

Donghyuk Kim, Manjima Dhar, Jonathan Lin, Keegan Owsley, Oladunni Adeyiga, Edward Pao, Jaekyung Kim, Harsha Kittur, Jerry Wu, Claire Hur, Joseph de Rutte, Hamed Haddadi, Bryan France, Bobby Tofig, Lorna Tokanuga, Joe Zendejas, Hector Munoz,

and many others!

Lastly, I owe thanks to my family for their steady encouragement all along.

VITA

Education

UCLA, Los Angeles, CA
BS, Bioengineering 2012

Peer Reviewed Publications

Published

1. Pushkarsky I, Lui, Y, Weaver WM, Su T, Mudanyali O, Ozcan A, Di Carlo D. Automated single-cell motility analysis on a chip using lensfree microscopy**. Sci. Rep**. 4. 2014.

2. Tseng P, Pushkarsky I, Di Carlo D. Metallization and bio-patterning on ultra-soft substrates via dextran sacrificial layers. **PLoS ONE** 9, e106091 (2014).

3. Koziol-White C, Yoo E, Cao G, Zhang J, Papanikolaou E, Pushkarsky I, Andrews A, Himes B, Damoiseaux R, Liggett S, Di Carlo D, Kurten R, Panettieri R Jr. Inhibition of PI3K promotes dilation of human small airways in a rho kinase-dependent manner. **Br. J. Pharmacol.** (2016).

In Revision

1. Pushkarsky I, Tseng P, Black D, France B, Lin J, Trinh R, Scumpia P, Morrison S, Damoiseaux R, and Di Carlo D. Elastomeric sensor surfaces for high-throughput single-cell force biology. **Nat Biomed Engr**, 1st Reviews returned 5/19/2017

2. Edwin J. Yoo 1, Gaoyuan Cao , Cynthia J. Koziol-White , Christie A. Ojiacku , Krishna Sunder , Joseph A. Jude, James V. Michael, Hong Lam , Ivan Pushkarsky, Robert Damoiseaux, Dino Di Carlo, Steven S. An , Raymond B. Penn , and Reynold A. Panettieri, Gα12 Facilitates Methacholine -Induced Shortening in Human Airway Smooth Muscle By Modulating Phosphoinositide 3-Kinase-Mediated Activation In A RhoADependent Manner **Br. J. Pharmacol.** (2017). 1st Revision complete 06/01/2017.

In Preparation

1. Pushkarsky I, Robert Damoiseaux, and Di Carlo D. High-throughput force cytometry of single-cells for drug discovery using FLECS technology. Invited submission to **SLAS Technology**; In preparation.

Highlight Articles

1. Kunze A., Pushkarsky I., Kittur, H. & Carlo, D. D. Research highlights: measuring and manipulating cell migration. Lab Chip 14, 4117–4121 (2014).

2. Pushkarsky I., Tseng, P., Murray, C. & Carlo, D. D. Research highlights: microfluidics and magnets. Lab Chip, (2014)

3. Kong JE., Kahkeshani, S., Pushkarsky I. & Carlo, D. D. Research highlights: micro---engineered therapies. Lab Chip 14, 4585–4589 (2014).

4. Kim, D., Pushkarsky I., Tay, A. & Carlo, D. D. Research highlights: aptamers on a chip. Lab Chip 15, 1630–1633 (2015).

5. Tay, A. K., Dhar, M., Pushkarsky I. & Carlo, D. D. Research highlights: manipulating cells inside and out. Lab Chip 15, 2533–2537 (2015).

Conference Proceedings

Oral Presentations

1. Micro Total Analysis Systems (MicroTAS) 2014. San Antonio, TX, USA. Oct. 26-30, 2014. Arrayed force-phenotyping of single-cells for high-throughput screening and analysis.

2. Nano-Biotech Montreaux 2014. Montreaux, Switzerland. Nov. 17-19, 2014. Arrayed force-phenotyping of single-cells for high-throughput screening and analysis.

3. Society of Laboratory Automation and Screening (SLAS) 2016. San Diego, CA, USA. Jan 26-30, 2016. Elastomeric sensor surfaces for high-throughput screening

4. Society of Laboratory Automation and Screening (SLAS) 2017. Washington, DC, USA. Feb 4 - 8, 2017. Arrayed force-phenotyping of single-cells for high-throughput screening and analysis.

Selected Poster Presentations

1. Micro Total Analysis Systems (MicroTAS) 2015. Gyeongju, South Korea. Oct. 25-29, 2015. Arrayed force-phenotyping for high-throughput quantification of phagocytic forces

2. IEEE EMBS Micro/Nano Tech in Medicine 2016. Waikoloa, HI Dec. 12-16, 2016. A Elastomeric sensor surfaces for identifying novel treatments for asthma.

Awards

1. Student Travel Award, CYTO 2017 Conference, 2017
2. 1st Place Poster Award, IEEE EMBS MNMC, 2016
3. Tony B Travel Award, SLAS, 2017
4. SLAS Innovation Award Finalist (1 of 9), 2016
5. Tony B Travel Award, SLAS, 2016
6. NSF Graduate Research Fellowship Honorable Mention, 2015

Chapter 1:

Importance of cell-generated forces in health and disease

Cell-generated mechanical forces are essential to the fulfillment of a wide variety of biological functions. In fact, every cell type in the human body, ranging from platelets and lymphocytes to have clear roles involving force generation. At the cellular level, contractile forces are used in mechanotransduction[1], migration[2], and cytokinesis[3]. In addition, force generation is used by individual cells performing highly specialized functions such as phagocytosis by professional phagocytes[4], regulation of blood pressure by pericytes[5], and even in engagement – and killing – of target cells by cytotoxic lymphocytes[6]. Force is also a key player in clotting function of platelets[7].

Cells also coordinate to generate large collective forces as parts of highly organized tissues. This seen in the three types of muscle tissue[8] which are integral to physiological systems including smooth muscle organs (e.g. digestive, reproductive, and airway systems), cardiac muscle which is responsible for oxygenating the entire body, and the tissue enabling motor movements in organisms, the skeletal muscle.

When properly fulfilling these roles, cells generate forces that can be classified as falling within a *normal* range. However, various mechanisms including genetic mutations, developed allergies, or physical trauma can lead to cells and tissue generating unhealthy levels of force, whether it is producing insufficient force that restricts specific functionality, or excessive force which interferes with other normal processes. The scope of the severity of these diseases can range from mild discomfort, to chronic disability, to even death. Since all cells utilize mechanical force

in some capacity, there is an exceedingly broad vulnerability to developing these diseases at the organism level.

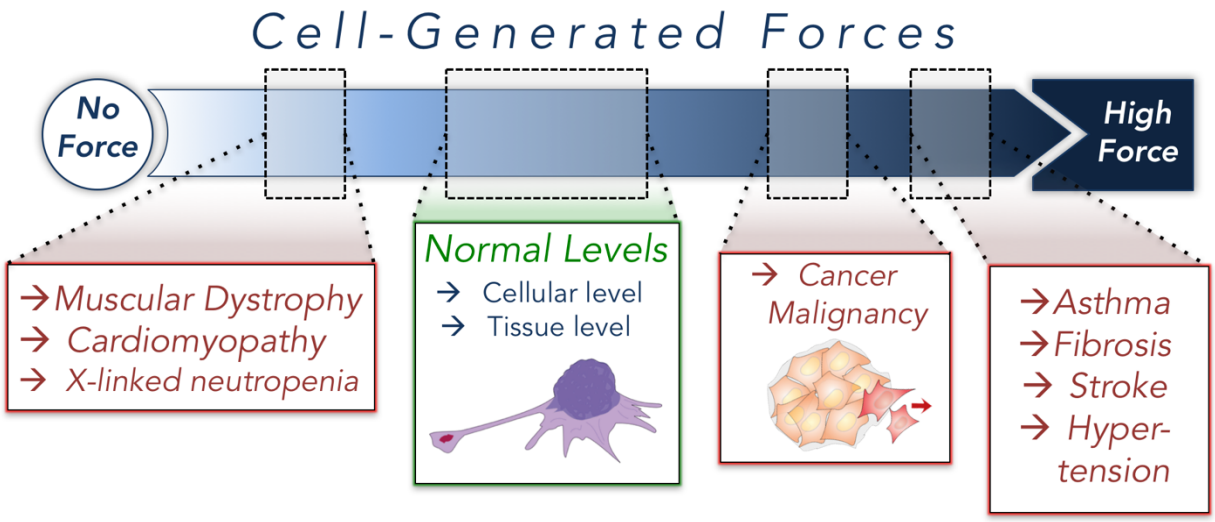

Figure 1-1. Illustration of the impact of improper cellular force generation on health

For each cell and tissue, there is a functionally "normal" or optimal magnitude of force generation. When these cells or tissues generate forces with magnitudes falling outside of this healthy range, whether manifesting as excessive force or as insufficient force, a variety of diseases may arise at the organism level. In general, these diseases relate to restriction of physiological function due to an insufficient force generating capacity such as in the case of cardiac insufficiency, or to interference of physiological function caused by altered mechanical environments, such as stiffened extracellular matrix due to highly contractile myofibroblasts, or excessively narrow airways or vasculature caused by unwanted or excessive contraction by smooth muscle cells or pericytes. In addition, force generation may also help enable malignant cells such as cancer.

Diseases arising from aberrant cellular force generation

Deregulated force generation can lead to a host of diseases. Excessive (high or undesirable) force generation is implicated in pathogenesis of asthma[9], fibrosis[10], stroke[11] and cancer[12], among others, whereas insufficient force generation lies at the root of lifestyle diseases like cardiac insufficiency and congenital defects such as X-linked neutropenia and muscular dystrophy.

A closer look at some of these diseases reveals the significant unmet clinical need that exists for producing therapies that can modulate cellular force generation:

Asthma

Most asthma symptoms result from airway narrowing in which airway smooth muscle (ASM) cell contraction and hypertrophy plays a dominant role in reduced lung function[13,14]. Accordingly, along with inhaled corticosteroids (ICS) that target the inflammatory mediators of increased airway constriction, long- and short-acting β2 adrenergic receptor agonists (LABAs and SABAs) have been the mainstay of asthma long-term management and short-term treatment of acute episodes. LABAs and SABAs cause smooth muscle relaxation through a combination of secondary effects including reduction of intracellular calcium, increased potassium channel conductance, and decreased myosin light chain kinase activity. Despite initial effectiveness, prolonged use of LABAs has been associated with airway hyper-responsiveness and increased asthma-related complications and mortality, such that LABAs carry a "black-box warning" and recent studies strongly recommend that LABAs are prescribed only in combination with ICS. Importantly, frequent use of LABAs are also associated with tolerance and reduced effectiveness of SABAs, which has severe clinical implications, given the emergency "rescue" use of SABA

inhalers by asthmatic patients. These risks underscore the urgent need for new classes of drugs for reversing bronchoconstriction in both children and adult populations.

Hypertension

Approximately one third of adults in the U.S. (75 million people) have high blood pressure, with an accelerating epidemic globally that is predicted to rise 50% by 2020 from 1 billion to 1.5 billion people. Hypertension is the number one modifiable risk factor for stroke and ischemic heart disease, two of the leading causes of death in the U.S.[15,16]. Consequently, there have been significant efforts to achieve blood pressure control through life style and pharmaceutical interventions. Although a range of classes of anti-hypertensive drugs are in use, about one quarter of patients under treatment for hypertension continue to have elevated BP and suboptimal control[17]. The high prevalence of resistant hypertension, in which hypertension is uncontrolled even with 3, and in some cases 5 antihypertensive drugs (including 1 diuretic), indicates the need for new classes of drugs and treatment approaches for inducing vasodilation[18].

Fibrosis

In liver fibrosis, research now directly links the contractile state of hepatic stellate cells (HSCs) to disease progression[19]. HSC-myofibroblast contractility leads to increased tissue stiffness which in turn stabilizes the myofibroblast phenotype, leading to more ECM deposition and increased stiffness resulting in a positive feedback loop and expansion of non-functional tissue[20,21]. Although liver fibrosis and progression to cirrhosis (dysfunction in hepatocyte function) accounts for only a small number of deaths per year, because of the chronic nature of the disease the direct costs in 2004 were estimated at $2.5 billion in the United States (when excluding patients

with hepatitis C infection)[22]. Currently, liver transplantation provides the only cure, but the accumulated costs per patient exceed those for even most cancers at $163,438[22]. This emphasizes the need to develop interventions at earlier stages of fibrosis to prevent cirrhosis and end-stage liver disease[23].

These are just a few examples of the chronic disorders arising from disrupted cellular force generation, yet they provide a powerful incentive for developing tools and methods to identify therapies that could help to beneficially modulate cellular force. Indeed, for several of these indications, existing treatments result in the relaxation of cellular contractility through established molecular pathways. However, the coupling of molecular pathways to the ultimate contractile strength is poorly understood and due to severe side-effects, tolerance development and outright resistance to treatment, new therapies are needed that act definitively on this mechanical cellular output. A scalable, general-use cellular force cytometer that could rapidly evaluate large screening libraries – and identify such candidates - has the potential to accelerate drug development efforts and anchor research in force biology.

Characteristics of an ideal general-use cellular force cytometer

In order to aid the study of aberrant force biology, and to help discover and develop new therapies to correct it, a tool that can directly access the force-generating phenotype is needed. Here, we set forth five design requirements for such a tool and provide justification for each. An ideal general-use cellular force cytometer should:

1. Have tightly-controlled parameters.

The method should exert a certain level of control of cell behavior such that any confounding variables (e.g. cell-cell contacts, variability in cell spread-area, etc.) are removed from the system and force-generation, alone, is isolated and quantified. This will ensure specificity and accuracy of the measurements.

2. Have a robust signal.

   The observed and measured signal should be easily discernible and clearly classifiable as a cellular force response, or otherwise, without uncertainty.

3. Provide high-throughput and be semi- or fully- automated in operation.

   To provide the necessary level of statistical significance, the system should aim to produce $\sim 10^2 - 10^3$ or more data points in each experiment. This will improve confidence in a given result and facilitate efficient progress. Clearly, these throughputs will be difficult to achieve if significant manual steps are needed. Therefore, the data analysis algorithm should be automatable.

4. Have exceptional sensitivity.

   Good sensitivity is desirable in such a system in order to detect even minor differences in force generation between e.g. similar cell types or low-dose treatments. Force biology is as-of-yet relatively understudied. It is conceivable that even small differences in this phenotype may be found to have disproportionate implications if present chronically when considering typical human lifespans.

5. Integrate with laboratory automation workflows.

   The volume of experiments, especially in the context of drug discovery, will quickly exceed what is reasonable for human workers to achieve unassisted. For example, industrial drug screening operations may test thousands of compounds each day. Thus, the system should have the potential to scale its productivity. Specifically, it should be formatted as a micro-titer plate or other standard format supported by laboratory robotics in order to integrate into the existing laboratory automation workflows.

Existing tools for measuring cellular forces

Given its importance, several techniques to assay contractility of cells have been developed. Perhaps the most widely used and developed is traction force microscopy[24,25]. In this approach a soft polymer substrate with embedded particles is used to map the forces applied by adherent cells. Forces applied by cells deform the underlying elastomeric surface and displace the embedded particles creating a deformation map that can be converted to a force map by solving an inverse problem assuming a mechanical model. Traction force microscopy is ideal for measurement of the detailed traction fields around individual irregularly adhering cells. However, because high-resolution imaging, complex image analysis, and re-imaging of each field following cell removal to obtain the un-deformed state of the substrate is required, only a few cells are usually measured per experiment. There have been recent efforts to increase the throughput of traction force microscopy. In one approach beads and cell placement[26,27] are pre-patterned to ease location finding and baseline calculation of the undeformed substrate after cell removal. In another approach transfecting target cells with labels to identify cell outlines[28] reduced the image analysis burden. Another clever approach makes use of labeled and patterned ECM on a soft acrylamide

substrate to track deformations of cells as they adhere in uniform labeled pattern[29]. Because of the difficulty of patterning on acrylamide and non-uniformity between ECM patterns this approach also required post-imaging following removal of cells to extract the un-deformed state. Even given these technological advances such approaches have demonstrated measurements of only ~20-50 cells per experiment, insufficient for evaluating heterogeneity in a population. Importantly, these smaller sample sizes also reduce the ability to discern minor effects of drugs and prevent accurate screening of a minority sub-population (e.g. progenitor cells in a phenotypically varied culture). Micropost arrays are also widely used to assay cellular force generation. In this technique thin elastomeric pillars support cell attachment and bend with cell-applied forces[30,31]. The discrete bending forces are calculated from high-resolution imaging of the deflections and known material properties and geometry of the pillars. Presumably, due to the high-resolution imaging required to assay the small pillar deflections in brightfield, published work using this technique have demonstrated measurements of at most a hundred cells per experimental condition.

Despite the usefulness of these methodologies, previous techniques have not been amenable to simple, high-throughput extraction of contractility measures from thousands of cells in parallel or in a multi-well format. Technological limitations that have prevented adopting current technologies for primary phenotypic screening include: (i) Non-uniform cell shape. Because cells adhere to substrates in random morphologies, analysis of forces applied by single-cells is often a painstaking and tailored process for each experiment. (ii) High-resolution imaging. The challenge of shape can be addressed by seeding cells onto micropatterned matrix, however, approaches to image small deflections of embedded beads or pillars requires high-resolution 40X magnification imaging, increasing time per cell analyzed significantly compared to 10X or 20X. (iii) Non-uniform pattern quality over large areas. Matrix patterning approaches on soft substrates

have only been developed recently, due to significant difficulties in transferring stable protein patterns onto soft substrates[29,32]. Additional hurdles arise when scaling micropatterning to the several fold increased footprint of SBS standard well-plates.

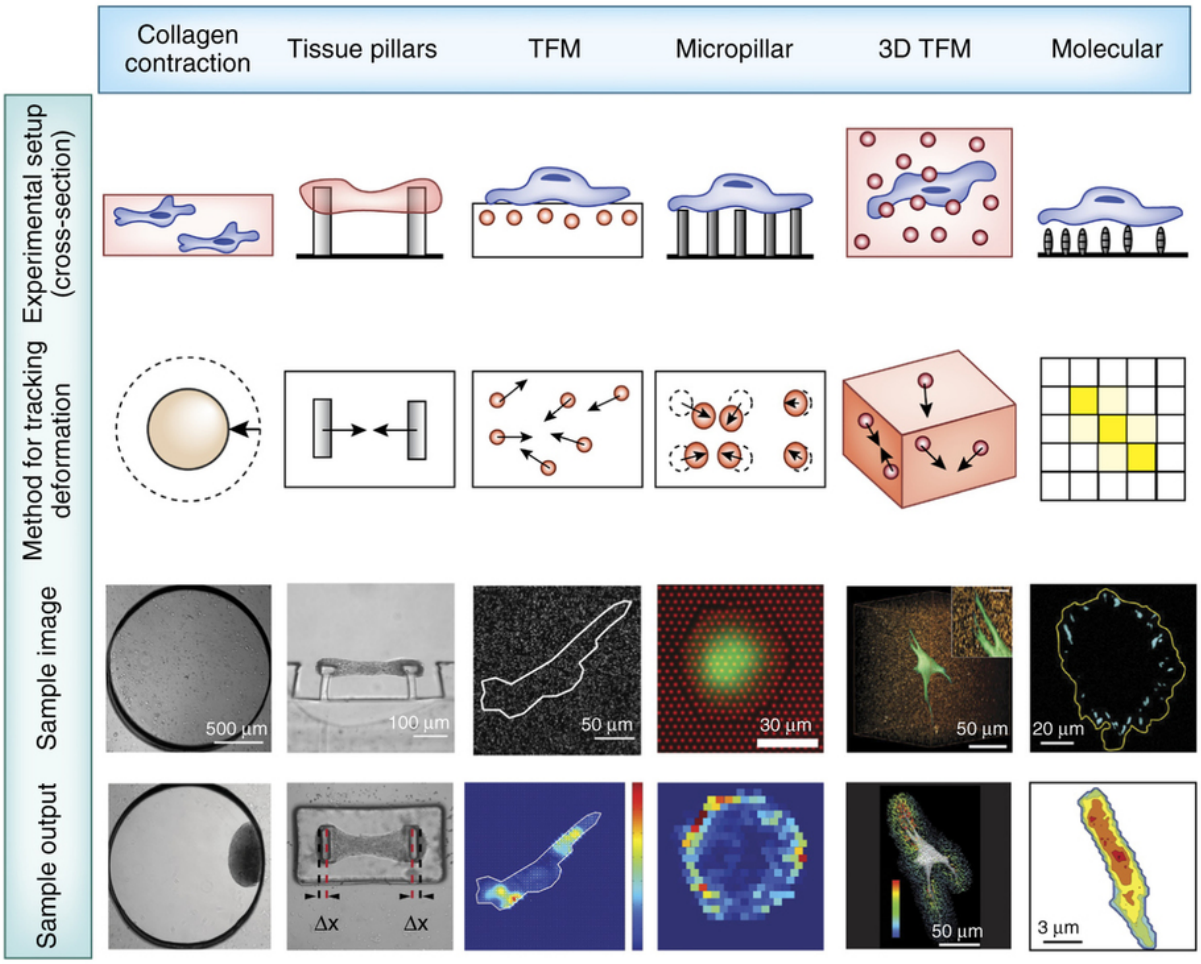

Figure 1-2: Existing tools for measuring cellular force generation

Adapted from ref 33 with permission from Nature Publishing Group.

A summary of some of the most widely used methods for measuring cellular force. Of these, TFM and micropillars are the most popular and well-studied.

In additional to having been used in a large collection of works, both techniques resolve subcellular force. However, a high degree of sophistication and engineering expertise is needed to fabricate these substrates and execute the methods. Analysis – which involves simultaneously tracking of perhaps hundreds of displaced markers, and extracting a strain field - is not straightforward, and require specific additional expertise. Furthermore, main steps and other factors described in the main text continue to prevent the adoption of these methods as high throughput drug discovery tools.

Conclusion

We conclude this opening chapter by reemphasizing that cellular force generation is a useful measure to evaluate disease state and therapeutics that target force generation selectively are clinically needed. Both quantitative screening approaches for therapeutics or genes that modulate cells' abilities to exert stresses, i.e. *cell contractility,* as well as robust methods to monitor the efficacy of potential treatments are important to develop. Importantly, since the functional cellular output drives these disorders, measuring force generation itself, and not a non-specific molecular surrogate such as calcium flux, is critical for maximizing the success of drug discovery.

In this opening chapter, we have discussed the strengths as well as the shortcomings of existing methodologies, and highlighted the need to overcome these limitations (requirements #3 and #5, in particular, have not been acceptably achieved). The next chapter will describe a novel microfabrication process we developed that will facilitate the development of a general-use cellular force cytometer that meets the requirements outlined herein.

Bibliography

1. Discher, D. E., Janmey, P. & Wang, Y.-L. Tissue cells feel and respond to the stiffness of their substrate. *Science* **310,** 1139–1143 (2005).

2. Fournier, M. F., Sauser, R., Ambrosi, D., Meister, J.-J. & Verkhovsky, A. B. Force transmission in migrating cells. *J. Cell Biol.* **188,** 287–297 (2010).

3. Burton, K. & Taylor, D. L. Traction forces of cytokinesis measured with optically modified elastic substrata. *Nature* **385,** 450–454 (1997).

4. Evans, E., Leung, A. & Zhelev, D. Synchrony of cell spreading and contraction force as phagocytes engulf large pathogens. *J. Cell Biol.* **122,** 1295–1300 (1993).

5. Hall, C. N. *et al.* Capillary pericytes regulate cerebral blood flow in health and disease. *Nature* **508,** 55–60 (2014).

6. Hui, K. L., Balagopalan, L., Samelson, L. E. & Upadhyaya, A. Cytoskeletal forces during signaling activation in Jurkat T-cells. *Mol. Biol. Cell* **26,** 685–695 (2015).

7. Myers, D. R. *et al.* Single-platelet nanomechanics measured by high-throughput cytometry. *Nat Mater* **16,** 230–235 (2017).

8. Harris, D. E., Work, S. S., Wright, R. K., Alpert, N. R. & Warshaw, D. M. Smooth, cardiac and skeletal muscle myosin force and motion generation assessed by cross-bridge mechanical interactions in vitro. *J. Muscle Res. Cell Motil.* **15,** 11–19 (1994).

9. Pelaia, G. *et al.* Molecular mechanisms underlying airway smooth muscle contraction and proliferation: Implications for asthma. *Respir. Med.* **102,** 1173–1181 (2008).

10. Huang, X. *et al.* Relaxin Regulates Myofibroblast Contractility and Protects against Lung Fibrosis. *Am. J. Pathol.* **179,** 2751–2765 (2011).

11. Yemisci, M. *et al.* Pericyte contraction induced by oxidative-nitrative stress impairs capillary reflow despite successful opening of an occluded cerebral artery. *Nat. Med.* **15,** 1031–1037 (2009).

12. Valencia, A. M. J. *et al.* Collective cancer cell invasion induced by coordinated contractile stresses. *Oncotarget* **6,** 43438–43451 (2015).

13. Pelaia, G., T. Renda, L. Gallelli, A. Vatrella, M. T. Busceti, S. Agati, M. Caputi, M. Cazzola, R. Maselli, andS. A. Marsico. 2008. Molecular mechanisms underlying airway smooth muscle contraction and proliferation: implications for asthma. Respir. Med. 102: 1173–81

14. Fredberg, J. J.. 2002. Airway narrowing in asthma: does speed kill? Am. J. Physiol. Lung Cell. Mol. Physiol. 283: L1179–80.

15. Merai R, Siegel C, Rakotz M, Basch P, Wright J, Wong B; DHSc., Thorpe P. CDC Grand Rounds: A Public Health

16. Approach to Detect and Control Hypertension. MMWR Morb Mortal Wkly Rep. 2016 Nov 18;65(45):1261-126 Yoon SS, Fryar CD, Carroll MD. Hypertension Prevalence and Control Among Adults: United States, 2011-2014. NCHS data brief, no 220. Hyattsville, MD: National Center for Health Statistics; 2015.

17. Cameron, A.C., Lang, N.N. & Touyz, R.M. Drugs (2016) 76: 1529. doi:10.1007/s40265-

18. Vongpatanasin W. Resistant Hypertension A Review of Diagnosis and Management. JAMA. 2014;311(21):2216-2224.

19. Pellicoro, A., P. Ramachandran, J. P. Iredale, and J. A. Fallowfield. 2014. Liver fibrosis and repair: immune regulation of wound healing in a solid organ. *Nat. Rev. Immunol.* **14**: 181–94.

20. Wells, R. G. 2005. The role of matrix stiffness in hepatic stellate cell activation and liver fibrosis. *J. Clin. Gastroenterol.* **39**: S158–61

21. Olsen, A. L., S. A. Bloomer, E. P. Chan, M. D. A. Gaça, P. C. Georges, B. Sackey, M. Uemura, P. A. Janmey, and R. G. Wells. 2011. Hepatic stellate cells require a stiff environment for myofibroblastic differentiation. *Am. J. Physiol. Gastrointest. Liver Physiol.* **301**: G110–8.

22. Neff, G. W., C. W. Duncan, and E. R. Schiff. 2011. The current economic burden of cirrhosis. *Gastroenterol. Hepatol. (N. Y).* **7**: 661–71.

23. Friedman, S. L. 1999. Evaluation of fibrosis and hepatitis C. *Am. J. Med.* **107**: 27–30.

24. Munevar, S., Y. Wang, and M. Dembo. 2001. Traction force microscopy of migrating normal and H-ras transformed 3T3 fibroblasts. *Biophys. J.* **80**: 1744–57.

25. Wang, J. H.-C., and J.-S. Lin. 2007. Cell traction force and measurement methods. *Biomech. Model. Mechanobiol.* **6**: 361–71.

26. Polio, S. R., K. E. Rothenberg, D. Stamenović, and M. L. Smith. 2012. A micropatterning and image processing approach to simplify measurement of cellular traction forces. *Acta Biomater.* **8**: 82–8

27. Liu, K., Y. Yuan, J. Huang, Q. Wei, M. Pang, C. Xiong, and J. Fang. 2013. Improved-throughput traction microscopy based on fluorescence micropattern for manual microscopy. *PLoS One*. **8**: e70122.

28. Marinković, A., J. D. Mih, J.-A. Park, F. Liu, and D. J. Tschumperlin. 2012. Improved throughput traction microscopy reveals pivotal role for matrix stiffness in fibroblast contractility and TGF-β responsiveness. *Am. J. Physiol. Lung Cell. Mol. Physiol.* **303**: L169–80.

29. Tseng, Q., I. Wang, E. Duchemin-Pelletier, A. Azioune, N. Carpi, J. Gao, O. Filhol, M. Piel, M. Théry, and M. Balland. 2011. A new micropatterning method of soft substrates reveals that different tumorigenic signals can promote or reduce cell contraction levels. *Lab Chip*. **11**: 2231–40.

30. Tan, J. L., J. Tien, D. M. Pirone, D. S. Gray, K. Bhadriraju, and C. S. Chen. 2003. Cells lying on a bed of microneedles: an approach to isolate mechanical force. *Proc. Natl. Acad. Sci. U. S. A.* **100**: 1484–9.

31. Fu, J., Y.-K. Wang, M. T. Yang, R. A. Desai, X. Yu, Z. Liu, and C. S. Chen. 2010. Mechanical regulation of cell function with geometrically modulated elastomeric substrates. *Nat. Methods*. **7**: 733–6.

32. Rape, A. D., W.-H. Guo, and Y.-L. Wang. 2011. The regulation of traction force in relation to cell shape and focal adhesions. *Biomaterials*. **32**: 2043–51.

33. Polacheck, W. J. & Chen, C. S. Measuring cell-generated forces: a guide to the available tools. *Nat. Methods* **13,** 415–423 (2016).

Chapter 2:

Biopatterning with high fidelity on ultra-flexible substrates via dextran sacrificial layers

This chapter describes a study performed on the development of a novel sacrificial microfabrication approach that enables precise and scalable production of uniform micropatterns consisting of various cell-adhesive biomolecules. The developed method, based on sacrificial dextran layers, enables the generation of biomloecular micropatterns of unprecedented quality on substrates as soft as 1-10 kPa, which can be visibly deformed by adhered, contracting cells, and thus lays the groundwork for the cellular force cytometer that is the central focus of this dissertation.

Polydimethylsiloxane (PDMS) forms the base of a large proportion of microdevices, and has seen extensive use in microfluidics[1-2], flexible electronics[3-8], and in developing cell-material interfaces[9-15]. A large proportion of traditional devices are fabricated using the standard formulation, a 10:1 ratio of polymer base to crosslinker that possesses an elastic modulus of approximately 2 MPa.

Ultra-flexible formulations of PDMS, which can be straightforwardly generated through increasing the base to cross-linker ratio up to 70:1, can typically achieve elastic moduli down below 3 kPa[14] which could have unique advantages for flexible electronics and as cell biology substrates. These flexible substrates, however, are relatively underutilized, particularly in terms of surface micromachining and in integration of these surfaces with complex microstructure. PDMS at this flexibility is unique to stiffer formulations in that they deflect under significantly lower stresses than standard PDMS,

and their viscoelasticity lends a minor self-healing quality to the layers. This could potentially yield a new avenue for flexible electronics, which often utilize composite structures of plastics and membranes of 10:1 PDMS. These ultra-flexible substrates have found the most use in cell biology, as PDMS moduli can approximate the moduli of tissues at ratios of 70 to 50:1 base to crosslinker ratios. At the elastic moduli created with these formulations, cells can significantly deflect the substrate on their own, without macroscopic stimuli. These substrates are diversely utilized for traction force microscopy[12,13,16] (measuring deflections generated by cells), stem cell differentiation[17], studying cell polarization[9], in which the goal is often to assay how stiffness of the substrata can affect cellular behavior[18].

In general, however, surface micromachining or patterning of PDMS at these extremely soft formulations is not straightforward due to complications in manipulating this layer. The main issue stems from the fact that PDMS at these formulations is typically tacky, non-specifically adheres over a wide variety of surfaces, and is generally difficult to pattern[19]. For example, siloxanes designed for this elastic modulus (such as Sylgard 527) are commonly used as adhesives. Standard methods of lithographically patterning standard PDMS[20] (such as with SU-8) are incompatible with soft formulations of PDMS due to layer incompatibilities with solvents, and large stresses that form during processing. Oxygen plasma exposure, often used to improve adhesion to stiffer formulations of PDMS, is similarly not directly amenable to patterning on ultra soft layers due to the formation of brittle, easily cracked oxide monolayers[21-22]. Direct contact printing approaches similarly lead to poor pattern transfer due to deformation of the underlying PDMS substrate, and nonspecific interactions between stamps and the substrate[19]. Microstructure is commonly

embedded in PDMS through physical demolding of PDMS from silicon substrates[23-25]. The same issues with stamping are encountered in demolding, as nonspecific interactions and the weak physical nature of soft PDMS often leads to significant deformation or destruction of the elastomer layer.

Water-soluble sacrificial layers have previously been studied as a method of releasing microstructure in surface micromachining[26]. These possess a number of advantages over traditional sacrificial layers, such as solvent or gas (ie. XeF2) based methods, namely their convenience in deposition and preparation (spin-coating, and low temperature baking), and the broad compatibility of the aqueous release step. This release step also potentially makes this compatible with a number of ultra soft (elastic modulus < 30 kPa) hydrogels and polymers.

Polyvinyl alcohol has seen initial work as either an intermediate, transfer carrier[27] for delicate structure fabricated on one substrate to another, or in transferring protein patterns onto PDMS and acrylamide hydrogels[19]. Despite its durability (it is stable as a free membrane), we found direct printing on these materials to be difficult due to poor adhesion of microstructure to native layers.

In this work, we utilize water-soluble dextran thin films coated on rigid silicon wafers as a direct template for the stable lithographical patterning and deposition/adsorption of micro- and nano-scale features. We found dextran, with proper surface treatment, to be a stable and durable host for these complex microstructures (Fig. 2-1). Features patterned by this method are treated (if required), and directly crosslinked and/or embedded within ultra-flexible PDMS (50 to 70:1) during its crosslinking step, in

contrast with previous approaches. Samples can be subsequently detached by sacrificial etching of dextran in water. In particular, this approach allows potentially destructive steps (including plasma treatments, thick film lithography processing) to take place on dextran instead of ultra-flexible PDMS layers, yielding clean, composite structures of PDMS and micropatterned materials. For example, plasma-treated dextran layers were also an excellent substrate for contact printing proteins, which transferred readily with minimal applied weight and contact time. Dextran layers are directly compatible with solvent-based lithographical processing of negative photoresists, for example developers such as polypropylene glycol monomethyl ether acetate, solvent rinses (acetone, methanol, isopropanol), and solvent-based photoresist strippers (n-methyl pyrrolidinone)[26].

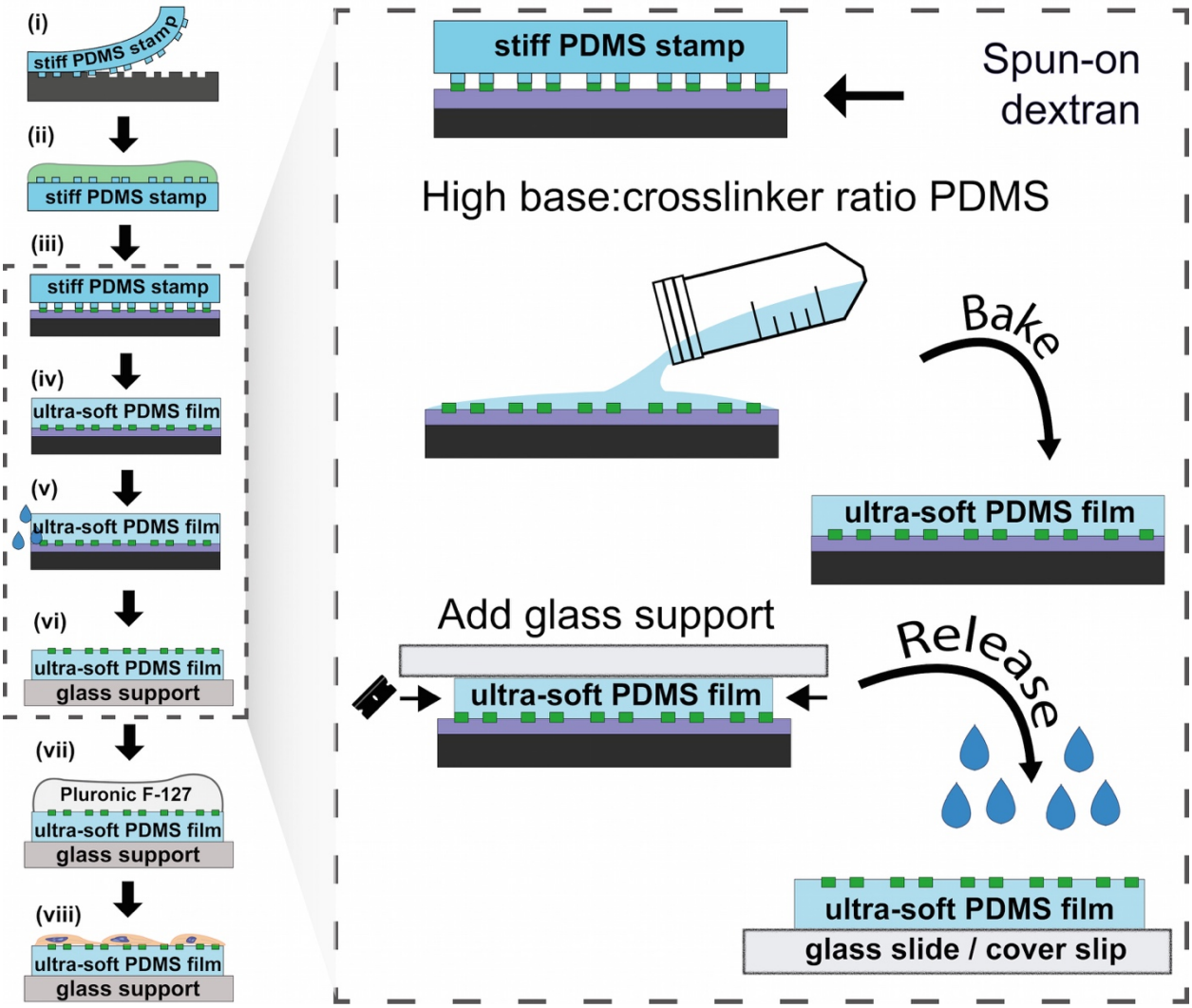

Figure 2- 1. Process flow for dextran-based surface micromachining of ultra-soft PDMS

Dextran is spun and dried on silicon pieces, before deposition of various micro- and nano-structures of ECM proteins or other biomolecules.. PDMS is subsequently cross-linked directly above these substrates, micromachined PDMS is released in water.

Notably, the wide range of chemical moieties that can be conjugated to the dextran used as the sacrificial layer for PDMS substrates allows tuning of wetting/surface adsorption characteristics of the elastomer beyond those of standard PDMS. We found that this approach stably integrated epoxy, proteins, metals, and particles into PDMS of variable stiffness, and we utilized composite structures generated by this method to pattern cells, measure deflections induced by cells, and study cell self-patterning in dual material systems.

Results

Transfer of dextrans and proteins into PDMS

We utilized the direct crosslinking of PDMS above dextran sacrificial substrates to integrate both dextran and proteins into PDMS. Strong bonding between dextran/protein and the PDMS network is encouraged by a number of interactions, including 1) a strong molding effect due to the high mobility of PDMS monomers during the initial prepolymerization stage of the interaction, and 2) covalent bonding between proteins and the PDMS through a so-called "poisoning" of the catalyst used in Sylgard 184 formulations of PDMS by various protein side chains, namely amino- and thiol- bearing amino acids[28-29], yielding covalent bonds between the siloxane network and the proteins.These effects help stabilize the introduction of dextran polymers (directly from the thin film layer), and patterned protein into the PDMS matrix. Once PDMS films were cured at room temperature (typically over 5 to 7 days), the dextran thin films were sacrificed directly in deionized water. Samples could finally be dried gently under a stream of pressurized air.

Dextran introduced onto PDMS surfaces by this method shifted both wetting and surface adsorption characteristics of the substrate. For example, introduction of simple dextran polymers onto PDMS slightly reduced initial contact angles (from 110 degrees to 90 degrees), but also significantly increased the retention of water onto these substrates (Fig. 2-2). This is likely due to the high water absorbing nature of dextran polymers. This could be clearly quantified by agitating water droplets, as contact angles uniformly dropped to 40 degrees after shock. We similarly investigated the introduction of amino bearing dextran polymers into PDMS, and their effect on wetting characteristics. Surfaces embedded with amino-dextran possessed initial contact angles of 40 degrees without need of agitation (Fig. 2-2). More valuably, dextran-mediated surface shifts were stable, and these substrates responded similarly at 1 day and 30 day exposure to air, conditions that would inevitably result in hydrophobic recovery of surface-treated PDMS.

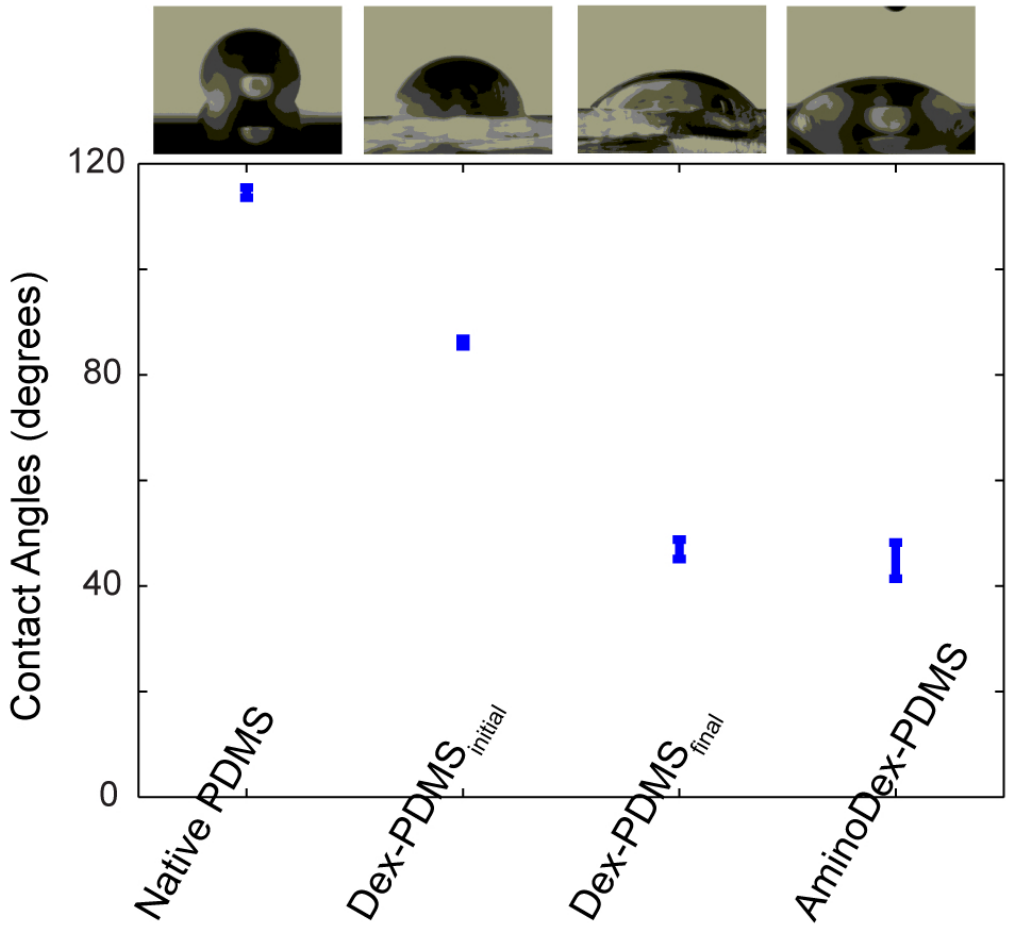

Figure 2-2. Contact angle of various formulations of dextran-PDMS.

Introduction of dextran onto the PDMS surface increases the wetting of the substrate, depending on formulation of PDMS, and absorption of water into the embedded dextran.

The protein adsorption characteristics of dextran films can vary significantly with the deposition process[30-31]. Interestingly, the presence of unconjugated dextran polymer on PDMS (both untreated and plasma-treated) had little effect on the adsorption of fibrinogen, which we assayed by measuring fluorescent intensity of stabilized protein. Introduction of

amino-dextran, however, significantly increased the adsorption of fibrinogen, possibly due to electrostatic interactions between the negatively charged fibrinogen, and positively charged amino-dextran (Fig. 2-3). Conjugated dextrans are fairly common and commercially available, and our results suggest that dextran embedding may be an alternative method of stably modifying the surface characteristics of PDMS and introducing stable functional groups.

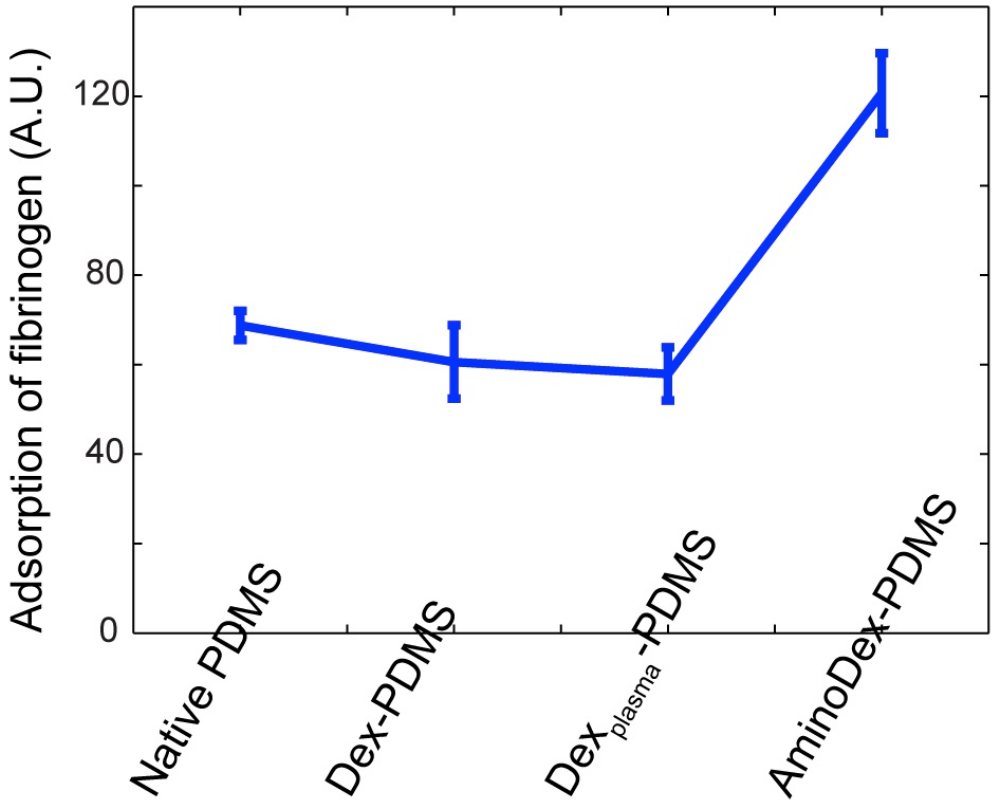

Figure 2-3. Adsorption characteristics of various formulations of dextran-PDMS (60∶1).

Unmodified dextran-embedded PDMS possesses similar adsorption to native PDMS, while amino-modified dextrans heavily adsorb fibrinogen.

Fibronectin could further be integrated into PDMS via micro-contact printing on top of dextran thin films prior to PDMS curing over the entire assembled surface (Fig. 2-4). A short plasma treatment of the dextran thin film (5 to 10 seconds) significantly improved the ease and fidelity of this step, although it was not explicitly necessary. Proteins robustly transferred during the PDMS (50 to 70:1) crosslinking, likely aided by the poisoning and crosslinking to the PDMS via poisoning of the crosslinker as discussed earlier. This provides a noticeable advantage over previous work with PVA, as an intermediary sulfo-SANPAH conjugation step was required for proper stabilization of the protein pattern. This approach could be presumably extended to a variety of contact printed proteins.

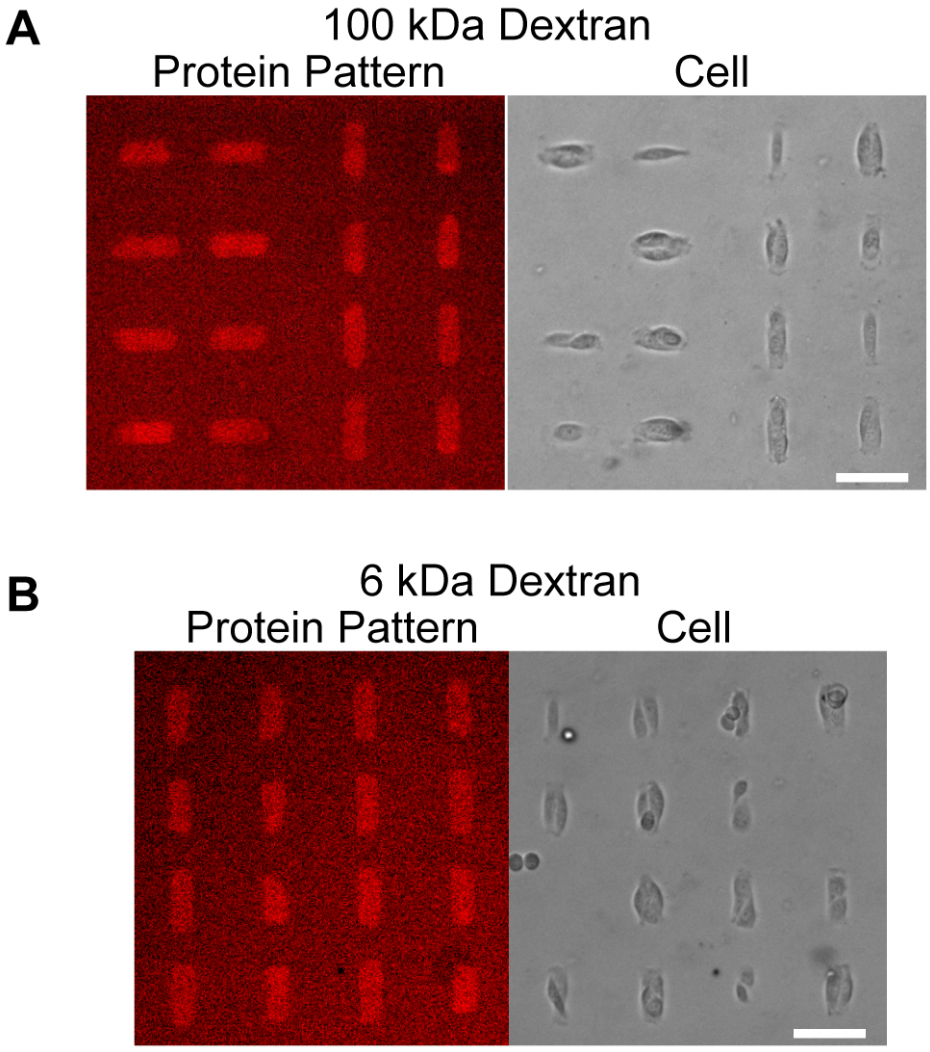

Figure 2- 4. Cell patterning.

a) and b) Live-cell images of cells cleanly patterned on fibronectin islets following 2 days of culture for both 100 kDa and 6 kDa dextran formulations. Scale bar is 60 µm.

We tested the fidelity of these patterns over up to 5 days, with the use of several molecular weights of dextran, both 100 kDa and 6 kDa. On both these formulations, cells localized exclusively to fibronectin patterns during the time frames of the experiment. Protein pattern transfer and reproducibility were effectively 100 % (Fig. 2-5) Individual

protein patterns stamped over .5 cm transferred with high reproducibility down to at least 8 μm. As protein patterns are separated via a contact-less method, the fidelity of the pattern reproduction is directly dependent on the stamping protocol.

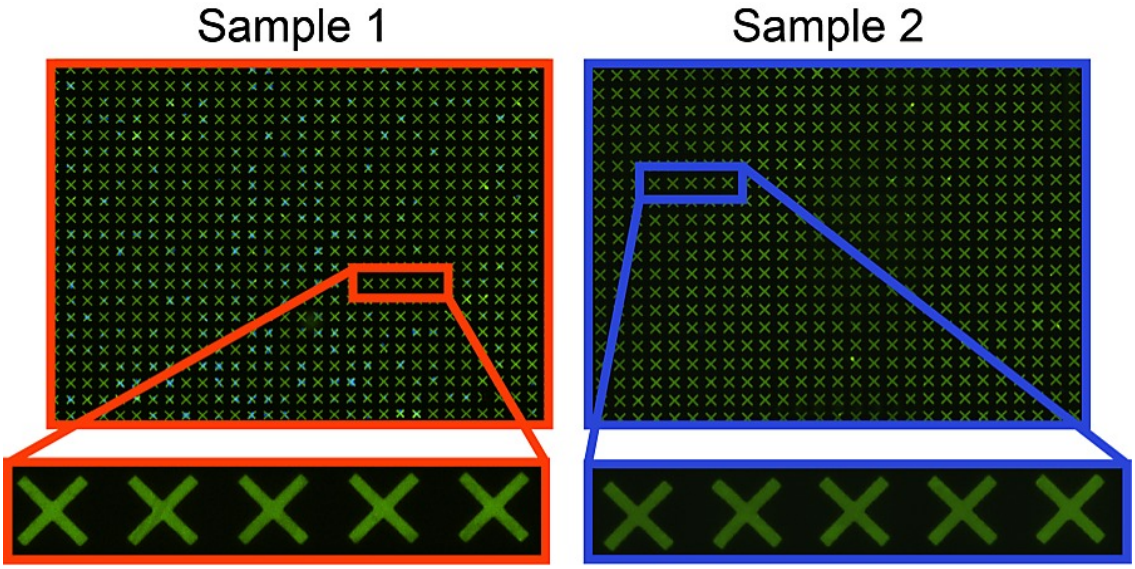

Figure 2-5: Repeatability of protein micro-patterning via sacrificial dextran layers.

Two separately prepared protein-patterned PDMS samples (65∶1). The consistency seen in the blown-up patterns demonstrates the robustness and repeatability of this patterning approach. Defects in individual patterns were particularly rare, occurring in <1% of patterns. The proteins used in the shown patterns are equal parts fibronectin and fibrinogen-Alexa Fluor imaged using 2 s exposure time with a 10X objective.

We ran preliminary assays on cell viability and growth on dex-PDMS substrates (Fig. 2-6) Cells grown on 10:1 PDMS, 60:1 PDMS, and 60:1 dex-PDMS had similar cell viabilities at day 1 and day 3 (all greater than 90%), and cells seemed to proliferate at similar rates (> 1 population doubling in a 40 hour time frame).

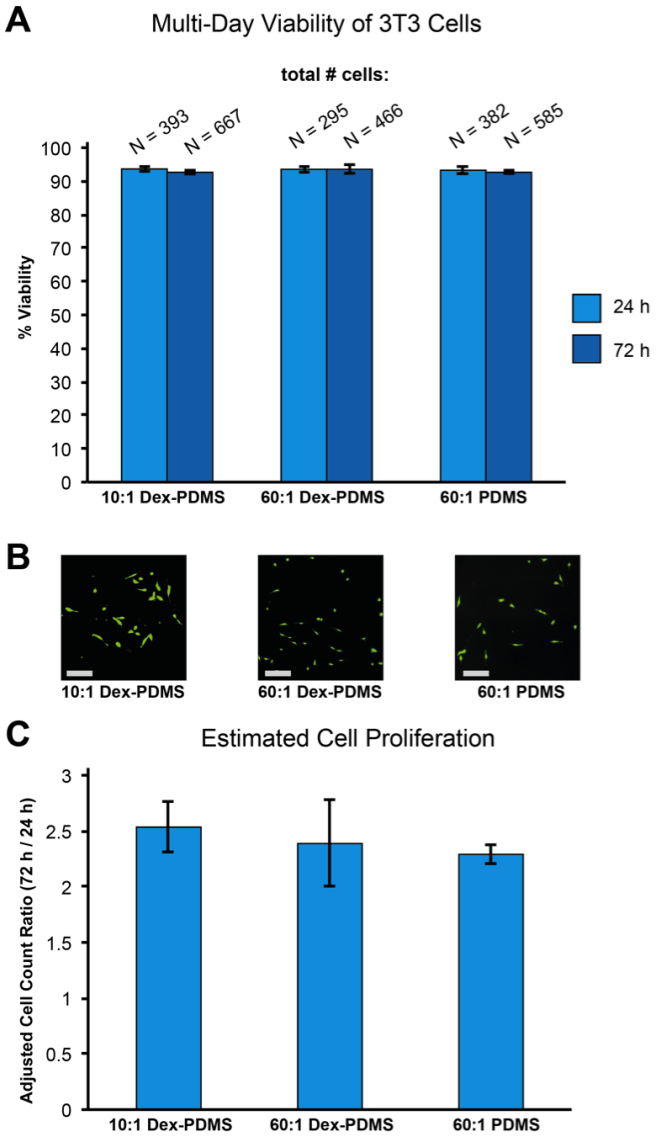

Figure 2-6: Cell survivability on dex-PDMS.

3T3 cells were cultured on dex-PDMS (60∶1 and 10∶1) and native PDMS (60∶1) for 24 hours and 72 hours. (A) Mean percentage cell viability defined as live cells over total cells counted. Cell viability was high (>90%) on all substrates at both 24 hours and 72 hours post-seeding. (B) Representative images of live 3T3 cells on each substrate at 72 hours post-seeding, stained with Calcein AM fluorescent dye. Scale bars are 250 µm. (C) Mean estimated cell proliferation, defined as the total number of live cells at 72 hours divided by the total number of live cells at 24 hours. The calculated ratio was adjusted by multiplication with the ratio of the used volumes (3/2). Proliferation was similar in all cases as cells underwent approximately one doubling (p>>.05). The error bars indicate standard deviation.

In additional to servicing as a temporary rigid scaffold for forming micropatterns composed of ECM proteins, we found that dextran layers were also serviceable as sacrificial layers for embedding epoxies, microparticles and metals into ultra-soft PDMS. These other experiments are described in detail elsewhere as they are not the focus of this dissertation[32].

Conclusions

In this work, we have detailed the use of dextran thin films as a sacrificial template for complex micropatterned features and microstructures, and subsequently utilized these to perform surface micromachining on ultra-soft PDMS (50 to 70:1 base to crosslinker). Dextran served to diversely generate patterns of epoxy, metal and protein, and as a substrate for adsorption of particles. By crosslinking PDMS above these substrates, and subsequently removing dextran with water, these structures stably integrated onto PDMS surfaces. This could be further stabilized by the use of molecular adhesives, such as APTES, and allyltriethoxysilane. To demonstrate the usefulness of this technique, we demonstrated proof-of-concepts over a range of applications to stably shift PDMS surface properties, pattern cells, study cell response to composite material structures, and finally to measure deflections induced during cellular contractions.

We believe that this methodology can be expanded to a suite of different nanostructures and materials as a means of surface micromachining both PDMS and other ultra-soft materials. The dual capabilities of shift surface properties with formulations of dextran, and introducing patterned microstructure could be utilized both in biological

studies and in developing flexible electronics, particularly those which require low elasticity (i.e. biomedical applications, or biointerfacing).

In the following chapters, we build upon this technique for generating stably-embedded protein micropatterns in ultra-soft PDMS to create an integrated platform for assaying cell-generated forces in a rapid, high-throughput and automated manner.

Materials and Methods

Preparation of dextran thin films

Dextran (100 kDa and 6 kDa, from Sigma Aldrich) were diluted into deionized water at a concentration of 20 % w/v, and spun (at 1,500 to 2,000 rpm) onto plasma-activated silicon wafers to agoal thickness of approximately 1 μm. Samples were dried on a hotplate at 150 ºC, and sectioned into pieces for subsequent microfabrication steps. Amino-dextran (70 kDa, Invitrogen) was diluted at 10 % w/v, poured onto silicon substrates, and subsequently dried overnight in a fume hood.

Preparation of Dex-PDMS and measurement of surface characteristics

PDMS (10:1 for contact angle measurements, and 60:1 for adsorption studies) was mixed, degassed, and poured onto dextran (100 kDa) or amine-conjugated dextran substrates, and allowed to crosslink at room temperature over 5 days. Samples were excised, and ultra-soft PDMS (60:1) slabs were mechanically stabilized by application of a backing glass coverslip. Dextran layers were subsequently dissolved overnight in deionized water, or phosphate-buffered saline to yield Dex-PDMS substrates.

Contact angles were measured by a goniometer. Dex-PDMS exhibited contact angle hysteresis which depended on length of prior exposure to water. Final contact angle was

determined following application of moderate shock to the substrate which served to initially wet the substrate, and uniformly reduced the contact angle of droplets.

Protein adsorption studies were conducted with fluorescent fibrinogen (Alexa fluor 568 conjugated, Invitrogen). 25 μg/mL protein was pipetted above substrates, and incubated at room temperature for 30 minutes. Fluorescent intensity was subsequently determined via a Nikon inverted fluorescence microscope.

Preparation of protein patterned PDMS

Protein stamps were fabricated by patterning KMPR photoresist (Microchem) on silicon (10 μm thick), and subsequently crosslinking and demolding of PDMS. Stamps were inked with a mixture of fibronectin, and fibrinogen-Alexa fluor (10 μg/mL, 30 minutes), and dried with pressurized air. Dextran substrates (100 kDa and 6 kDa) were activated via air plasma (Harrick) for 5 seconds, and immediately stamped with protein for 5 minutes. PDMS (60:1) was then poured above substrates, and crosslinked at room temperature over at least 5 days before dextran layers were dissolved in PBS overnight, and subsequently blocked in 1 % Pluronic F127 (Sigma) for 1 hour.

Cell culture

Cells (3t3, ATCC CCL-92) were cultured using standard protocols. Cells were grown in complete medium, trypsinized, seeded onto substrates, and allowed to attach and spread over 1 hour. Samples were subsequently washed in complete medium.

Cells seeded on protein patterned PDMS were imaged using bright-field and fluorescence microscopy over a 4-day time frame.

Bibliography

1. Ng JMK, Gitlin I, Stroock AD, Whitesides GM (2002) Components for integrated poly(dimethylsiloxane) microfluidic systems. Electrophoresis 23: 3461–3473. doi:10.1002/1522-2683(200210)23:20<3461::AID-ELPS3461>3.0.CO;2-8.

2. Xia Y, Whitesides GM (1998) Soft Lithography. Annu Rev Mater Sci 28: 153–184. doi:10.1146/annurev.matsci.28.1.153.

3. Kim D-H, Rogers JA (2008) Stretchable Electronics: Materials Strategies and Devices. Adv Mater 20: 4887–4892. doi:10.1002/adma.200801788.

4. Khang D-Y, Jiang H, Huang Y, Rogers JA (2006) A Stretchable Form of Single-Crystal Silicon for High-Performance Electronics on Rubber Substrates. Science 311: 208–212. doi:10.1126/science.1121401.

5. Mannsfeld SCB, Tee BC-K, Stoltenberg RM, Chen CVH-H, Barman S, et al. (2010) Highly sensitive flexible pressure sensors with microstructured rubber dielectric layers. Nat Mater 9: 859–864. doi:10.1038/nmat2834.

6. Gray DS, Tien J, Chen CS (2004) High-Conductivity Elastomeric Electronics. Adv Mater 16: 393–397. doi:10.1002/adma.200306107.

7. Yoon J, Baca AJ, Park S-I, Elvikis P, Geddes JB, et al. (2008) Ultrathin silicon solar microcells for semitransparent, mechanically flexible and microconcentrator module designs. Nat Mater 7: 907–915. doi:10.1038/nmat2287.

8. Hung PJ, Jeong K, Liu GL, Lee LP (2004) Microfabricated suspensions for electrical connections on the tunable elastomer membrane. Appl Phys Lett 85: 6051–6053. doi:10.1063/1.1835553.

9. Prager-Khoutorsky M, Lichtenstein A, Krishnan R, Rajendran K, Mayo A, et al. (2011) Fibroblast polarization is a matrix-rigidity-dependent process controlled by focal adhesion mechanosensing. Nat Cell Biol 13: 1457–1465. doi:10.1038/ncb2370.

10. Balaban NQ, Schwarz US, Riveline D, Goichberg P, Tzur G, et al. (2001) Force and focal adhesion assembly: a close relationship studied using elastic micropatterned substrates. Nat Cell Biol 3: 466–472. doi:10.1038/35074532.

11. Lee JN, Jiang X, Ryan D, Whitesides GM (2004) Compatibility of Mammalian Cells on Surfaces of Poly(dimethylsiloxane). Langmuir 20: 11684–11691. doi:10.1021/la048562+.

12. Iwadate Y, Yumura S (2008) Actin-based propulsive forces and myosin-II-based contractile forces in migrating Dictyostelium cells. J Cell Sci 121: 1314–1324. doi:10.1242/jcs.021576.

13. Gutierrez E, Tkachenko E, Besser A, Sundd P, Ley K, et al. (2011) High Refractive Index Silicone Gels for Simultaneous Total Internal Reflection Fluorescence and Traction Force Microscopy of Adherent Cells. PLoS ONE 6: e23807. doi:10.1371/journal.pone.0023807.

14. Ochsner M, Dusseiller MR, Grandin HM, Luna-Morris S, Textor M, et al. (2007) Micro-well arrays for 3D shape control and high resolution analysis of single cells. Lab Chip 7: 1074–1077. doi:10.1039/b704449f.

15. Ostuni E, Chen CS, Ingber DE, Whitesides GM (2001) Selective Deposition of Proteins and Cells in Arrays of Microwells. Langmuir 17: 2828–2834. doi:10.1021/la001372o.

16. Iwadate Y, Yumura S (2008) Molecular dynamics and forces of a motile cell simultaneously visualized by TIRF and force microscopies. BioTechniques 44: 739–750. doi:10.2144/000112752.

17. Trappmann B, Gautrot JE, Connelly JT, Strange DGT, Li Y, et al. (2012) Extracellular-matrix tethering regulates stem-cell fate. Nat Mater 11: 642–649. doi:10.1038/nmat3339.

18. Tseng P, Di Carlo D (2014) Substrates with Patterned Extracellular Matrix and Subcellular Stiffness Gradients Reveal Local Biomechanical Responses. Adv Mater 26: 1242–1247. doi:10.1002/adma.201304607.

19. Yu H, Xiong S, Tay CY, Leong WS, Tan LP (2012) A novel and simple microcontact printing technique for tacky, soft substrates and/or complex surfaces in soft tissue engineering. Acta Biomater 8: 1267–1272. doi:10.1016/j.actbio.2011.09.006.

20. Guo L, DeWeerth SP (2010) An Effective Lift-Off Method for Patterning High-Density Gold Interconnects on an Elastomeric Substrate. Small 6: 2847–2852. doi:10.1002/smll.201001456.

21. Béfahy S, Lipnik P, Pardoen T, Nascimento C, Patris B, et al. (2010) Thickness and Elastic Modulus of Plasma Treated PDMS Silica-like Surface Layer. Langmuir 26: 3372–3375. doi:10.1021/la903154y.

22. Gou H-L, Xu J-J, Xia X-H, Chen H-Y (2010) Air Plasma Assisting Microcontact Deprinting and Printing for Gold Thin Film and PDMS Patterns. ACS Appl Mater Interfaces 2: 1324–1330. doi:10.1021/am100196z.

23. Adrega T, Lacour SP (2010) Stretchable gold conductors embedded in PDMS and patterned by photolithography: fabrication and electromechanical characterization. J Micromechanics Microengineering 20: 055025. doi:10.1088/0960-1317/20/5/055025.

24. Lee KJ, Fosser KA, Nuzzo RG (2005) Fabrication of Stable Metallic Patterns Embedded in Poly(dimethylsiloxane) and Model Applications in Non-Planar Electronic and Lab-on-a-Chip Device Patterning. Adv Funct Mater 15: 557–566. doi:10.1002/adfm.200400189.

25. Lim KS, Chang W-J, Koo Y-M, Bashir R (2006) Reliable fabrication method of transferable micron scale metal pattern for poly(dimethylsiloxane) metallization. Lab Chip 6: 578. doi:10.1039/b514755g.

26. Linder V, Gates BD, Ryan D, Parviz BA, Whitesides GM (2005) Water-soluble sacrificial layers for surface micromachining. Small Weinh Bergstr Ger 1: 730–736. doi:10.1002/smll.200400159.

27. Karlsson JM, Haraldsson T, Carlborg CF, Hansson J, Russom A, et al. (2012) Fabrication and transfer of fragile 3D PDMS microstructures. J Micromechanics Microengineering 22: 085009. doi:10.1088/0960-1317/22/8/085009.

28. Heyries KA, Marquette CA, Blum LJ (2007) Straightforward Protein Immobilization on Sylgard 184 PDMS Microarray Surface. Langmuir 23: 4523–4527. doi:10.1021/la070018o.

29. Kishi K, Ishimaru T, Ozono M, Tomita I, Endo T (2000) Development and application of a latent hydrosilylation catalyst. IX. Control of the catalytic activity of a platinum catalyst by polymers bearing amine moieties. J Polym Sci Part Polym Chem 38: 804–809.

30. Farrell M, Beaudoin S (2010) Surface forces and protein adsorption on dextran- and polyethylene glycol-modified polydimethylsiloxane. Colloids Surf B Biointerfaces 81: 468–475. doi:10.1016/j.colsurfb.2010.07.059.

31. Yu L, Li CM, Liu Y, Gao J, Wang W, et al. (2009) Flow-through functionalized PDMS microfluidic channels with dextran derivative for ELISAs. Lab Chip 9: 1243.

32. Tseng, P., Pushkarsky, I. & Carlo, D. D. Metallization and Biopatterning on Ultra-Flexible Substrates via Dextran Sacrificial Layers. *PLOS ONE* 9, e106091 (2014).

Chapter 3:

Elastomeric sensor surfaces for high-throughput single-cell force biology

In Chapter 1, we highlighted importance of cell-generated forces in human health and disease and outlined the requirements for a general-use cellular force cytometer. As discussed, several current approaches to studying cell generated forces – specifically, traction force microscopy (TFM)[1,2] and elastomeric micropost arrays (EMA)[3] - have provided valuable insight into the localization and magnitudes of cell traction forces, typically in small quantities of cells, in numerous studies[4-7]. However, these methodologies were optimized primarily for mapping out subcellular forces rather than for rapidly profiling large cell populations with single-cell resolution, and are often difficult to operate[8] and computationally expensive and therefore have not been adapted for large-scale cell classification, clinical diagnosis, industrial drug discovery, or rapid dose-response analyses (in particular, they fail to satisfy requirements #3 and #5).

In Chapter 2, we described a novel fabrication process for generating high-fidelity adhesive protein micropatterns that could simultaneously control cell shape, spread area and contacts, and gauge the cell's contractile output via displacements of the micropattern boundaries. This chapter describes the integration of the sacrificial dextran protein micropatterning approach into a powerful, ready-to-use single-cell force cytometer that fulfills the requirements we set forth.

Our aim was to develop a platform that focused on assaying whole-cell contractions for hundreds to thousands of cells at a time, reasoning that subcellular spatial resolution may not be necessary to adequately characterize the force-response of a cell population and thus it could be conceded in favor of a significant reduction in computational and operational complexity, and greatly improved overall throughput that could provide population level statistics. In addition to

enabling simple and streamlined analyses that would be amenable to the large-scale implementations discussed above, we also emphasized the need to measure contractility at the single-cell level in order to resolve any functional heterogeneity present in a sample and to have the capability to link the functional output of a given cell to its own molecular phenotype. To create such a system, we built upon the concept of micro-patterning on elastic surfaces which previously was introduced to control cell spreading while performing TFM measurements[9,10] and in one instance, as a method of transducing pattern deformations into absolute force based on an initial calibration that also required TFM[11].

We developed a novel microfabrication approach with which we can routinely produce large arrays of uniformly shaped, fluorescently-labeled adhesive micropatterns embedded in ultra-soft elastomeric surfaces with the high fidelity offered by stamping on rigid surfaces. In this system, each adhesive micropattern may be deformed by a single adhered cell and thus serves as a unique surface sensor for cellular contraction.

In this work, the fabrication and operational principles of the platform are described and the technique's ability to resolve contractile differences among cell populations despite operating at the whole-cell level is validated. Linking of molecular features to functional output on a per-cell basis is also demonstrated and an unexpected relationship between smooth muscle cells and a specialized actin is revealed. To expand use to pharmacological interventions, the sensor surfaces are integrated into a multi-well plate format to facilitate high-throughput studies and utilized in that embodiment to titrate a myosin inhibitor and to examine the cellular-level functional responses of human airway smooth muscle to asthmatic agonists. Finally, the molecular compositions of the micropatterns are tuned to explore force-generating immunological responses in primary human phagocytes and these forces are quantified. It is shown for the first time that specific inhibition of

phosphoinositide 3-kinase p110δ reduces phagocytic force generation in primary human macrophages. The presented system achieves throughputs that are up to two orders of magnitude higher than previously demonstrated and is shown to be compatible with a wide range of cell types. All demonstrations sample >100 cells (and up to several 1000) per experiment. At this point in its development, the platform should be ready for immediate adoption for biological research and screening applications involving cellular force generation.

Results

Principles of the FLECS platform

The micro-engineered Fluorescently-Labeled Elastomeric Contractible Surfaces (FLECS) platform consists of a thin glass-backed elastomeric film with controlled elasticity that is precisely patterned with large arrays of fluorescent adhesive ligands (>240 patterns per mm^2) prepared using sacrificial layers[12] (Fig. 3-1). The non-patterned regions of the film are blocked with Pluronic F-127 to restrict cell adhesion to the controlled area of the micropatterns, which deterministically orient the cell forces and eliminate random cell-cell contacts. Cells adhering to these micropatterns contract the underlying elastomeric film and displace the micropattern boundaries (Fig. 3-1a, Movies S1, S2). These displacements, which reflect the applied forces, are visualized using fluorescent microscopy.

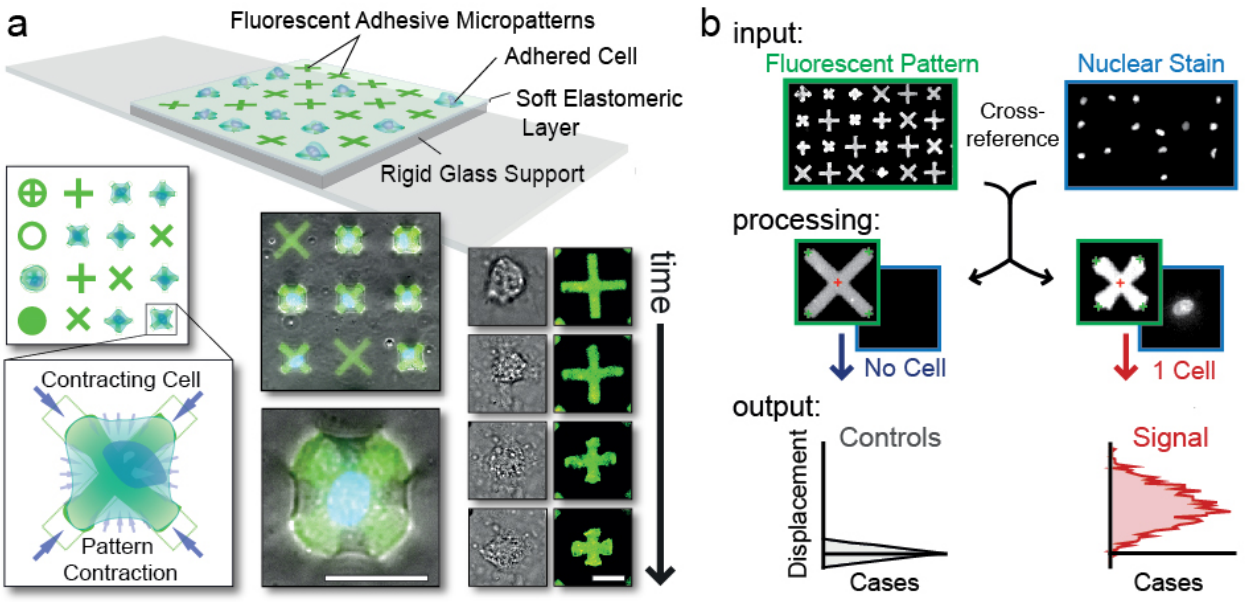

Figure. 3-1: Schematic of the FLECS cytometry system

(***a***) *TOP: Platform schematic showing cells adhered to functionalized adhesive micropatterns embedded into a thin glass-supported elastomeric film. LEFT: Top view showing multiple pattern shapes and a blow-up of a cell contracting an "X" pattern and inwardly displacing its terminals. BOTTOM: Overlay of fluorescent patterns and phase contrast images of adhered contracting cells. RIGHT: Time-lapsed images of a contracting cell and the underlying micropattern. Scale bar represents 25 µm.* (***b***) *Image analysis workflow.* ***.*** *INPUT: Image sets of the micropatterns (set 1) and the stained cell nuclei (set 2). PROCESSING: Algorithm (i) identifies and measures all micropatterns in image set 1, (ii) cross-references the positions of each micropattern in image set 2 and (iii) determines whether 0, 1, or >2 nuclei (i.e. cells) are present. OUTPUT: Mean center-to-terminal displacements of the micropatterns containing a single nucleus (i.e. 1 cell) are compared to the median of the corresponding measurement of all un-displaced patterns containing 0 nuclei (i.e. un-occupied patterns) and the differences are plotted as a horizontal histogram.*

The sacrificial patterning approach we use yields uniform micropatterns (>99% pattern reproducibility, see: Fig. 2-5, Chapter 2); as such, non-displaced micropatterns, i.e. micropatterns unoccupied by adhered cells, serve as baseline measurements. An image processing algorithm implemented in MATLAB locates all micropatterns in an image set, determines whether or not they contain cells based on nuclear counterstaining, and calculates the characteristic dimension (d) of each micropattern occupied by exactly 1 or 0 cells. (For the "X" pattern used in most of our experiments, this dimension is the mean center-to-terminal length). Then, the single-cell displacement data (displacement = median($d_{baseline}$) - d_i, for each cell i) are plotted in horizontal histograms to allow simple visual comparisons between distributions (Fig. 3-1b, Fig. 3-2).

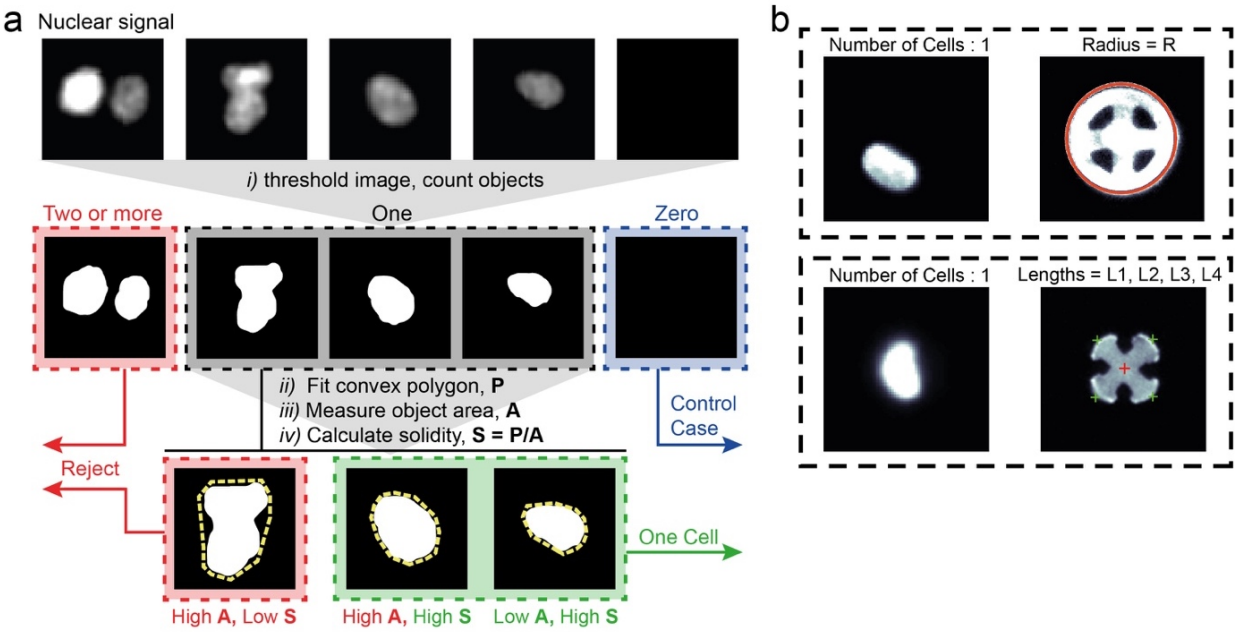

Figure 3-2: Cell counting algorithm and data storage.

(a). The input image is thresholded and the independent objects present in the frame are counted. Images with counts of >1 and 0 are classified appropriately,

while those with counts of exactly 1 have the smallest possible convex polygon (P) fitted to the object, and the fraction of the area of this polygon (P) that is occupied by the object area (A), called 'solidity' (S=P/A) is calculated. Smaller objects are more likely to be a single nucleus. Larger objects are more often multiple nuclei so they must have a high solidity (characteristic of the general shape of a nucleus), to be considered one cell. Using these gates, single objects are sorted with 99% sensitivity and >90% specificity. (b) Representative images of the data stored for each experiment. In addition to a .mat file storing the numerical data, an image file is created for every pattern processed in every experiment. These files are indexed such that they can be specifically looked up or even removed from the data set if they represent noise (e.g. defective pattern).

In this work, the two-component Sylgard 184 silicone elastomer is used for the thin film. However, we found other silicone elastomers to be functional alternatives. The substrate elasticity, which does not affect micropattern quality, is modulated by varying PDMS base to cross-linker ratios. Once prepared, these functionalized elastomeric substrates have a shelf-life of greater than one year at room temperature.

Evaluation of tonic whole-cell contraction in adherent cells

In developing the FLECS system we made the important assumption that whole-cell contraction measurements, which are certainly coarser than the subcellular force localization provided by the TFM and EMA approaches, are not only still useful, but are alone sufficient for reliably discerning contractile differences among cell populations. To evaluate this assumption, we examined the contraction profiles of human multi-potent mesenchymal stem cells (hMSCs),

which are known to exert large contractile forces and interrogate mechanical cues in their environment[9, 10], and their differentiated progeny. For these studies, the symmetric "X" pattern was chosen because it symmetrically focuses cell adhesions to its four narrow terminals thus spatially concentrating the cell forces to produce quantifiable displacements of those terminals towards the pattern center[13]. Importantly, patterning also conserved cell shape which is known to influence the way cells generate traction forces[14]. We anticipated that these micropattern displacements would be accurately representative of the contractile forces produced by a given cell as a whole.

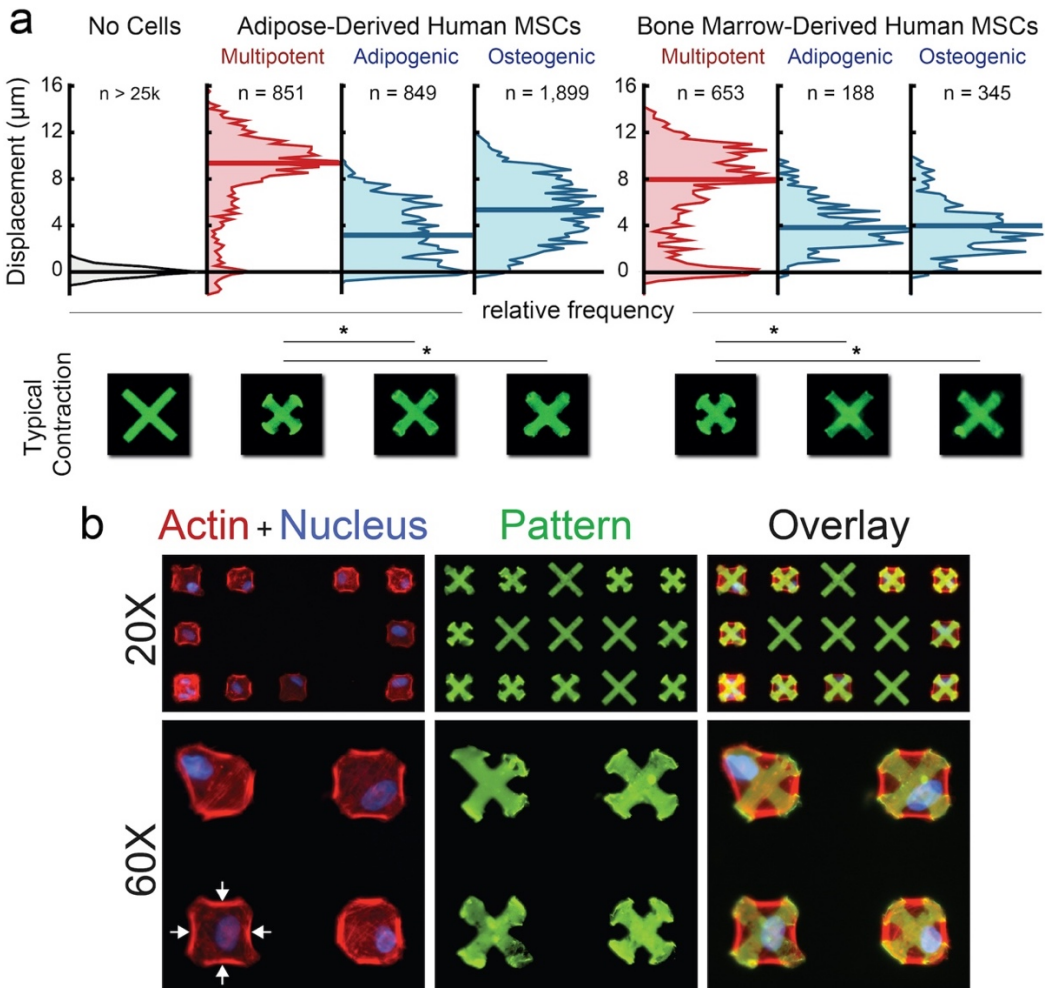

Figure 3-3: Whole-cell contractility of primary human mesenchymal stem cells and progeny

(**a**) Primary human adipose- or bone marrow-derived mesenchymal stem cells (MSCs) exhibited much higher contractile responses than either committed lineage 8 hrs post-seeding. Non-contractile subpopulations are seen amongst the MSCs indicating heterogeneity and potentially low purity that results from standard separation methods. N represents the number of cells. A typical contracted pattern representing approximately the median case from each distribution is shown below. (**b**) Overlays of fluorescent images of contracted patterns (green), phalloidin–stained actin (red) and nuclei (blue) of adipose-derived multi-potent MSCs showing three instances of cells fully spread over the patterns and actin stress fibers that route stresses to the vertices of the "X" patterns. Scale bar represents 25 μm.

As expected, the hMSCs spread uniformly to occupy these micropatterns and formed actin stress fibers that bridged adjacent terminals (Fig. 3-3b). A diagonal micropattern dimension of 70 μm was determined to be optimal for maximizing the dynamic range when testing cells of this size. Regardless of tissue of origin, hMSCs in a multipotent state produced significantly higher steady-state micropattern displacements suggesting more force generation than seen in either set of differentiated hMSCs (Fig. 3-3a). Previously, Fu *at al.* demonstrated high forces in differentiating hMSCs that peaked in the first day of culture but decreased consistently over the following 7 days[15]. Our results are in agreement with this trend as they reveal significantly lower forces in MSCs following longer differentiation times (i.e. at 14 days as in our experiment). The congruence between our respective findings indicates that whole-cell contraction measurements are indeed reflective of traction forces obtained using subcellular methods. Importantly, the

FLECS platform makes it possible to analyze all cells present in a sample without pre-selection, in one automated procedure. This enabled the measurement of 180 to >1500 cells per condition (rather than 13-26 cells) and identified a smaller sub-population of weakly contractile cells in each multi-potent stem cell sample.

Encouraged by this result, we applied the FLECS technology to study additional physiologically important contractile cells. Of particular interest were smooth muscle cells (SMCs) – the myocytes that comprise the tissues lining the walls of hollow organs like the urinary, intestinal and reproductive tracts, airways, and vasculature. Considering the multitude of disorders arising from abnormal smooth muscle contractility including asthma, hypertension, and bowel disease[16], a tool to rapidly characterize the native or induced contractility of a large population of SMCs would be invaluable for research and drug development purposes.

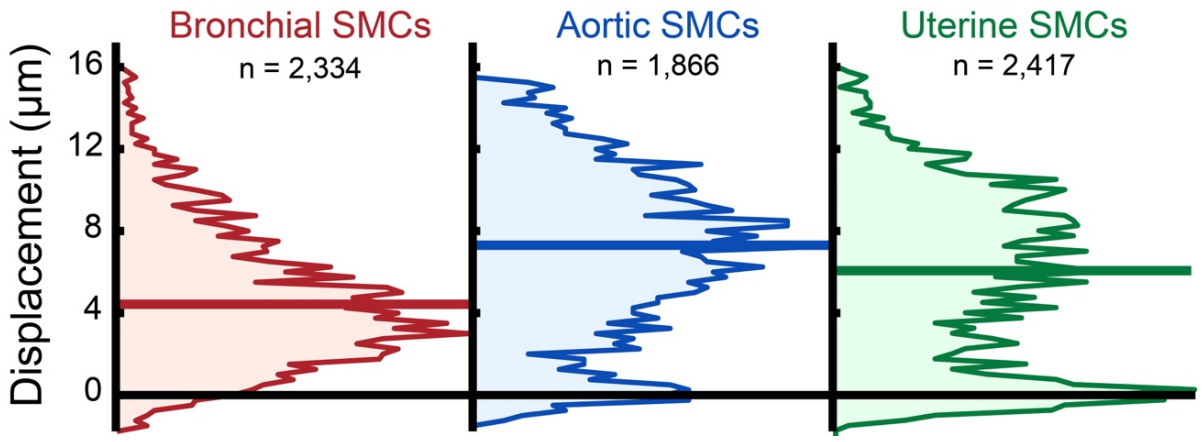

Figure 3-4: Contractility of primary human smooth muscle cells.

Contractility of primary human smooth muscle cells (SMCs) taken from the bronchiole, aorta and myometrium.. (a) Aortic and uterine smooth muscle cells

demonstrated higher tonal contractile potential than bronchial cells, reflecting the different functions of these tissues despite similar structures. A significant non-contractile population was identified among uterine SMCs perhaps due to contamination by non-SMCs from the site of isolation. This subpopulation may also indicate such cells may exist in multiple phenotypic states e.g. contractile or proliferative. N indicates number of cells in each distribution.

We looked at three sets of primary human SMCs —bronchial SMCs (BSMCs), aortic SMCs (ASMCs) and uterine SMCs (USMCs) — and found that all three uniformly spread over and contracted the 70 μm "X" patterns, producing measurable displacements. Interestingly, ASMCs and USMCs, on average, exhibited greater steady-state contractions than BSMCs suggesting higher native force generation by those cells in the absence of stimuli (Fig. 3-4). This may be explained, in part, by the fact that both of these tissues clearly generate force to perform their functions, whether in vasoregulation (ASMCs) or uterine contraction during labor (USMCs), whereas BSMCs do not have a clear contractile function in healthy persons. A larger subpopulation of weakly contracting cells was also identified in the USMC distribution, likely due to the relative difficulty of isolating pure populations from this complex tissue, compared to the tube-like aorta and bronchioles. These experiments demonstrate that this method is suitable for studying the force biology of smooth muscle cells. Further experiments with other cell types including various human and murine fibroblasts, and cancer cell lines indicated that this method is applicable to adherent mammalian cells in general, although the optimal micropattern dimensions sometimes varied.

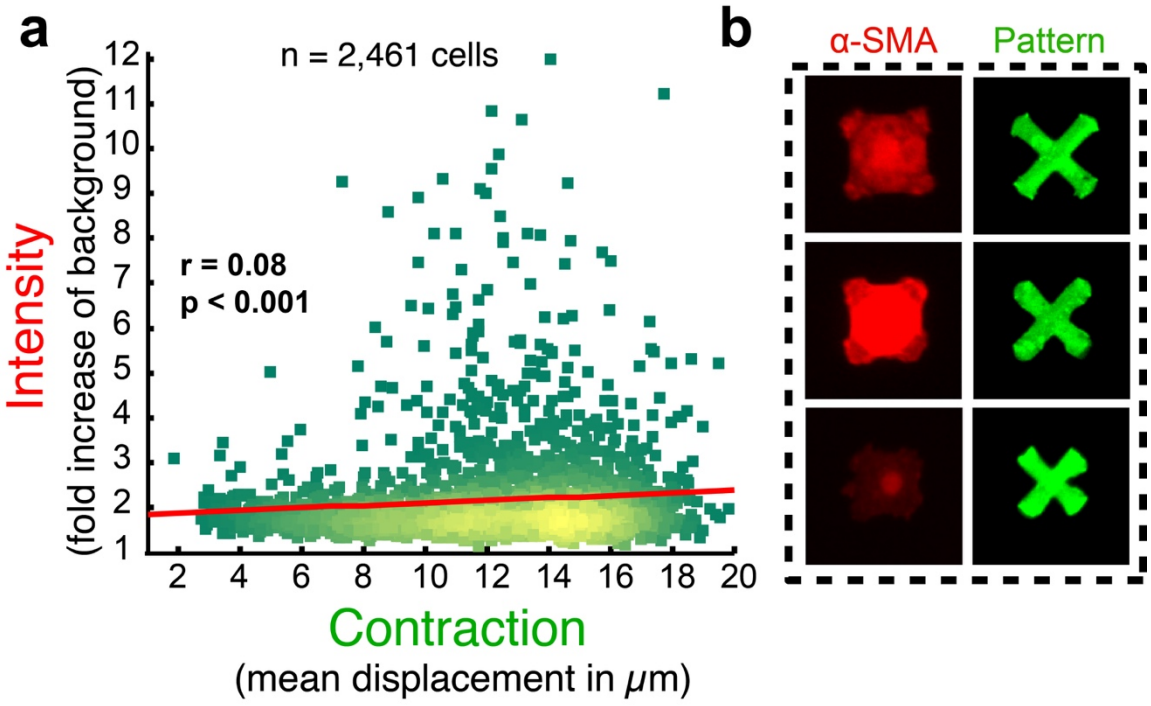

Figure 3-5: Cell-by-cell correlation of functional and molecular phenotypes

*(**a**) Correlation of the functional contractile output of primary uterine smooth muscle cells to their expression of α-smooth muscle actin (α-SMA). Each data point represents the mean micropattern displacement and relative fluorescent intensity of stained α-SMA of a single cell. (**b**) Three cells chosen from the scatterplot representing distinct relationships between contractility and relative quantities of α-SMA. Overall, no strong positive trend is observed.*

Using the FLECS workflow, cells may be imaged live or fixed in their contracted state and subsequently phenotypically profiled. Since the cells are confined to micropatterns with known positions and boundaries, an algorithm can be used to quantify molecular biomarkers associated with a functional output (e.g., contraction) at the single-cell level over a population of cells. We applied this analysis to determine the functional importance of α-smooth muscle actin

(α-SMA) in USMCs expecting that since α-SMA is used to identify SMCs post-extraction, and has been linked to enhanced matrix remodeling in fibroblasts[17,18], that it should be a reliable indicator of cell contraction and scale accordingly. Surprisingly, we found that although there was a higher frequency of outlier brightly stained cells displaying above-median tonic contraction, α-SMA staining levels and contraction were not strongly correlated at the population level (across a sample of >2,400 cells), having a Pearson coefficient $r = 0.08$ ($p<0.001$)(Fig. 3-5). Whether the trend holds for stimulated rather than tonic contraction, or whether it is similar in other smooth muscle cells remains to be seen. However, this finding indicates that in at least one cell type, molecular characterization is insufficient in providing functional information about the cells, and that a functional assay such as the one presented here, is needed.

Assay parallelization enables pharmacological studies

The FLECS platform may also be implemented in the multi-wellplate format to achieve a substantial degree of parallelization without significant increases in fabrication labor or manual imaging requirements. The 96-wellplate embodiment of our platform (containing >6000 70 μm "X" patterns per well) lends itself to standard laboratory automation workflows and offers a practical solution to performing highly-parallelized assays (Fig. 3-6A) such as studies of contractile stimuli and relaxants which often require many doses and replicates.

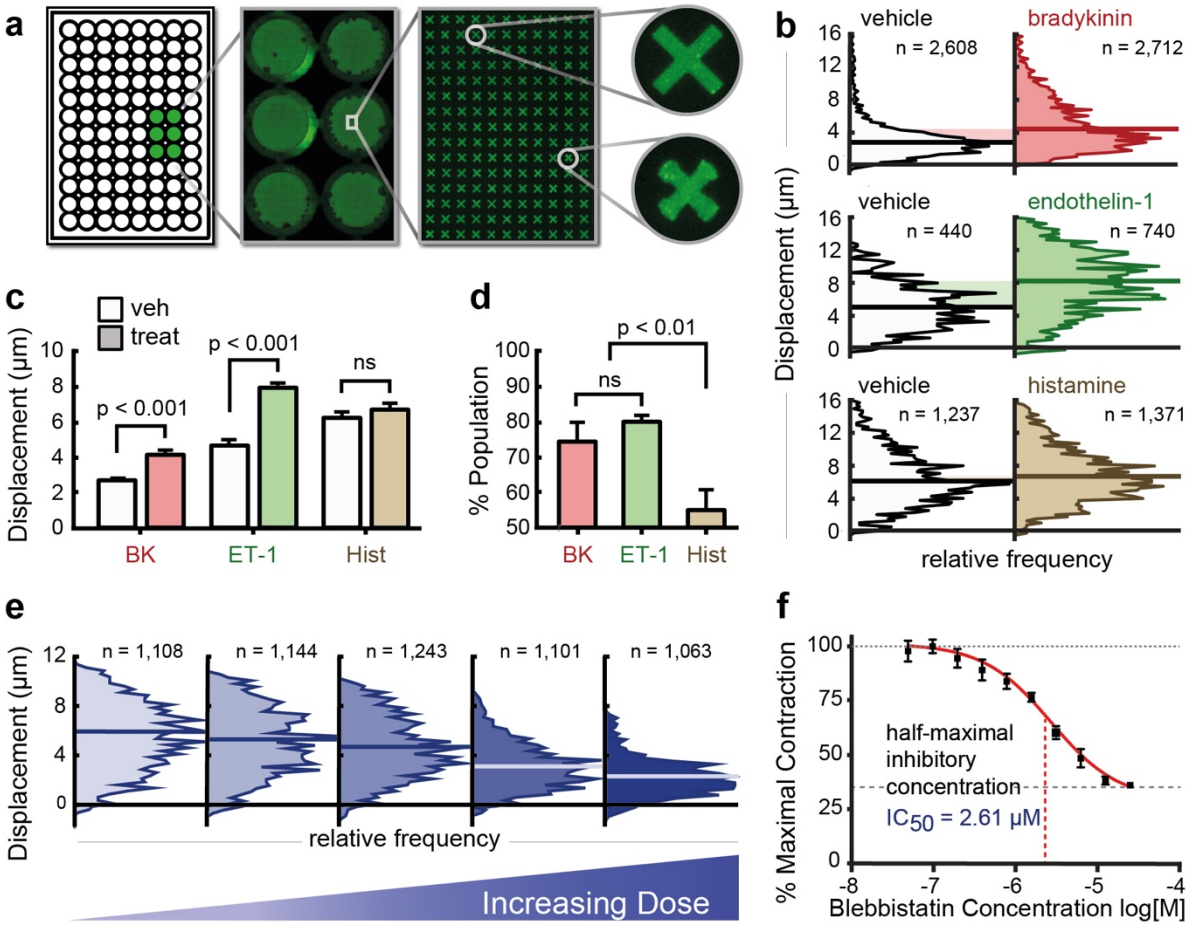

Figure 3-6: Microtiter plate format enables highly-parallelized single-cell contractility measurements in high-throughput

*(**a**) 96-well plate implementation. Left to right: Well-plate footprint; large stitched image of 6 adjacent wells each containing a micro-pattern array; blow-up of a single well revealing a high fidelity pattern array; blow-ups of an un-occupied (top) and contracted (bottom) pattern. (**b**) Contractility distributions of HASM treated with either control solution or a pro-contractile agonist (1 µM BK, 100 nM ET-1 or 100 µM Hist). Each plot represents the pooled data from 4 technical replicates. Substantial increases in contraction across the population are seen in cells treated with bradykinin and endothelin-1 but not histamine. (**c**) Graphs showing median levels of contraction for the*

plots in (b). Bars represent mean of the 4 replicates + standard error of the mean (SEM). ***(d)*** *Percentage of cells from a treated population exhibiting contractions greater than the median of the corresponding untreated population. This analysis indicates similar potency among bradykinin and endothelin-1, and little effect from histamine.* ***(e)*** *Representative distributions of single-cell responses to increasing doses of blebbistatin. Plots comprise pooled data from 4 technical replicates of each condition.* ***(f)*** *Dose-response curve over 3 decades in which we identify an IC_{50} of 2.61 μM. Error bars represent SEM. N represents number of cells in each distribution.*

We used this parallel (FLECS-Plate) format to survey the relative potency of three of the main mediators of bronchoconstriction involved in asthma on human airway smooth muscle (HASM) cell contractility. Previous work demonstrated that challenges with bradykinin or histamine[19] as well as with endothelin-1[20] induced cytosolic calcium concentration ($[Ca^{2+}]_i$) changes in HASM cells. Using magnetic twisting cytometry, Hubmayr *et al*. also showed that both bradykinin and histamine markedly increased HASM cell stiffness[21]. We investigated whether $[Ca^{2+}]_I$ changes and cell stiffening were robust indicators of cell contraction — which is the mechanical basis of airway narrowing in symptomatic asthma.

Bradykinin (BK) and endothelin-1 (ET-1) but not histamine (Hist) were found to increase contraction in HASM cells (Fig. 3-6b-c). When looking at population level shifts we found that BK and ET-1 had very comparable effects on single-cell contraction, with both stimulating about 50% more cells to contract above the control median levels (Fig. 3-6d). However, challenge with Hist did not yield observable increases in contraction at the population level.

To rule out the possibility that Hist operates through a slower acting pathway, we continuously monitored the micropatterns for a longer time period of up to 30 mins after treatment. Virtually all imaged cell-occupied micropatterns within wells treated with both BK and ET-1 were observed to contract beyond the baseline over the first 5 to 20 mins after addition and sustained these increases until beyond 30 mins, at which point a small subset of micropatterns began expanding again. In wells treated with Hist, the large majority of micropatterns did not exhibit noticeable unidirectional changes at any point, while a small population showed a slight increase in contraction which occurred over the first 10 minutes, peaking at 15 minutes before reversing. Movies S3-S5 depict a small region of a site from wells treated with 1 μM BK, 100 nM ET-1, and 100 μM Hist, respectively.

Our findings indicate that Hist may act through a tissue-level pathway to induce shortening or that Hist is not as potent as BK or ET-1, which are themselves similarly potent, in potentiating contractions in isolated HASM cells. These functional differences were observed despite similar indications in upstream molecular signaling and mechanobiology. In general, this analysis not only suggests that $[Ca^{2+}]_I$ flux and cell stiffening may not be correlated with robust cell shortening, but also that there may be substantial functional heterogeneity within a cell population that could be resolved only with single-cell resolution and extensive sampling.

Functional drug dose-response evaluation

The FLECS-plate, which uses the industry-standard wellplate form factor, was engineered specifically for its compatibility with the existing automation and screening infrastructure, i.e. liquid handling robotics, plate handling robotics and high-content imaging systems. Such an implementation enables automated, rapid, and high resolution dose-response

characterization of effectors of cellular contractility. Here, we evaluate this capability by titrating the effects of the myosin II inhibitor, blebbistatin, on contracting HASM cells using a 10-step, 2-fold dilution scheme and vehicle controls with 4 technical replicates for each (equating to 44 independent measurements) on a single functionalized 96-well FLECS-plate (Fig. 3-6e). As expected, addition of the drug produced a restorative effect on the cell-contracted micropatterns (Movie S6), which was dose-dependent. We observed low variability across the replicates, and by fitting a sigmoidal curve to these data, we calculated an IC_{50} of 2.61 μM which quantitatively matches previously reported values[22,23] (Fig. 3-6f). These results demonstrate that automating (and scaling) the FLECS assay is feasible and yields robust readouts. Thus, when leveraging laboratory automation systems, we expect the FLECS-plate will facilitate automated screens of large drug libraries to help identify new candidates for correcting malfunctioning cellular contractility, and enable potency characterization of promising hits. The single-cell resolution should also help reveal any differential, bimodal, or other non-Gaussian responses to modulators at the population level.

Measuring spontaneous and electrically-paced cardiomyocyte contractions

FLECS supports measurement of phasic contractions, such as beating cardiomyocytes. We demonstrate this by seeding newly isolated neonatal rat ventricular myocytes (NRMVs) on "X" patterns or rod-shaped patterns and either monitoring spontaneous beating, or applying electrical pacing pulses and quantifying the magnitudes of their contractions (Movies S8-S10). We were able to resolve rhythmic and arrhythmic, single-cell, sub-second contraction and contractile strength in individual NRVMs (Fig. 3-7). This modality is currently being used to explore factors involved in cardiomyocyte maturation for applications in disease modeling.

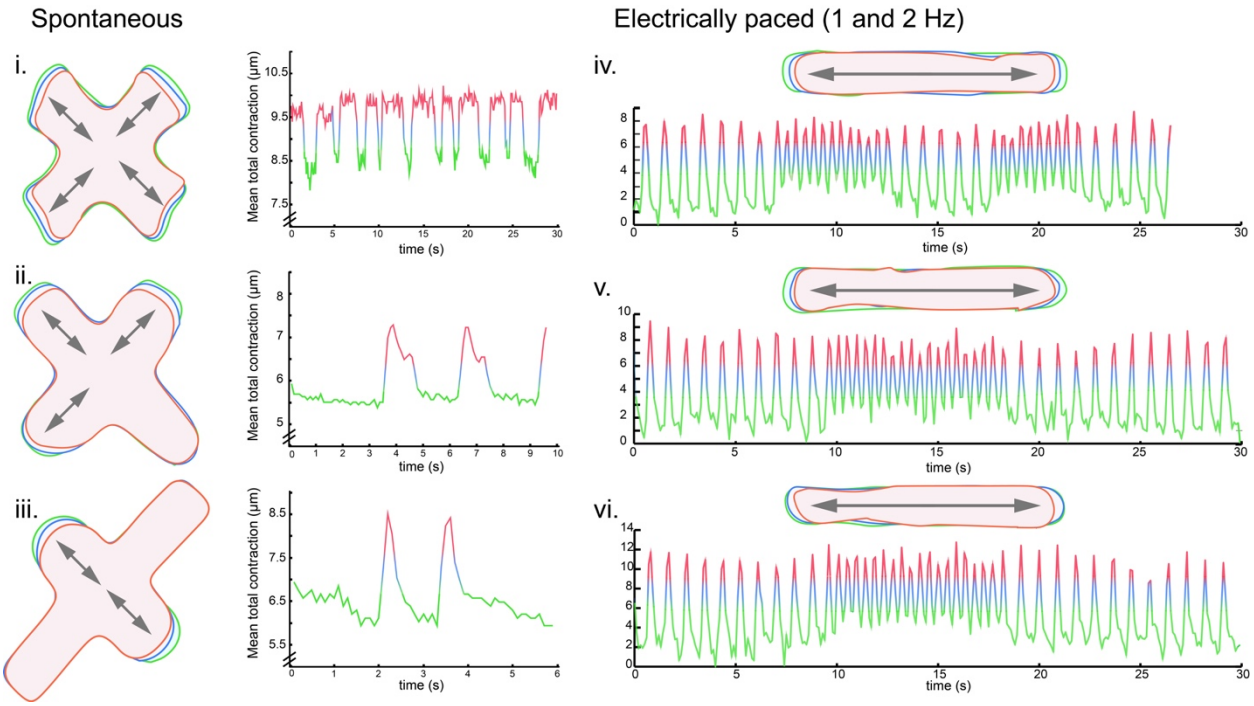

Figure 3-7: Traces of live beating single neonatal rat ventricular myocytes.

Freshly isolated neonatal rat ventricular myocytes seeded on fibronectin-fibrinogen patterns were observed to phasically contract without stimulation approximately 6 hours after seeding (i. – iii.) or were paced using pulsatile 12V/cm electric fields (iv. – vi.) at frequencies alternating between 1 Hz and 2 Hz. The diagrams show outlines of representative cell-occupied micropatterns spanning the range of observed motion between the basal tonic contraction (green) to the maximal contraction (red). The real-time videos corresponding to cases i. and iv. can be found in Movie S9 and S10, respectively. Cardiomyocytes showed heterogeneity in spreading behavior on "X" patterns, so pseudo-one-dimensional rod patterns were used (right). Here, the behavior was conserved, as all cells spread along this single dimension.

Passive and active forces applied by adhered primary human phagocytes

Proper physiological function depends not only on coordinated cell contractions occurring at the tissue level, but also on forces generated independently by single-cells. This is particularly evident in leukocytes which, along with chemical mechanisms, use mechanical forces in both innate and adaptive host defense. Extravasation and transmigration[24], spreading[25], and mechanosensing[26–28] are all force-generating processes performed by certain leukocytes during immune response. In adaptive immunity, mechanical force is used for initiation and stabilization of the immune synapse[29] , and in the case of cytotoxic T-cells, it directly contributes to the killing of target cells[30]. In innate immunity, mechanical forces direct phagocytosis – the process by which phagocytes internalize and destroy foreign pathogens. In addition to constituting one of the first lines of defense, this process also plays an important housekeeping role in tissues and during healing. Operating at the single-cell level, our new tool is suited to measure phagocytic forces and here we do this in primary human macrophages.

We induced frustrated phagocytosis of our patterns by opsonizing them with chimeric IgG containing human Fc regions. We first embedded dansylated bovine serum albumin (DNS-BSA) into the elastomeric surface, and then incubated the surfaces with anti-dansyl chimeric IgG (hIgG). This surface functionalization reliably induced a phagocytic response: human monocyte derived macrophages (MDMs) rapidly adhered, spread over, and contracted the opsonized patterns and maintained the contraction for up to 16 hours (Movie S7).

Using these micropatterned immune complexes, we sought to determine whether the phagocytic forces supplied by MDMs were modulated by the quantity of the presented stimulus. To answer this question, we patterned the hIgG in three circular shapes with equal diameters (54

μm), to control cell-spread area, but successively less total antibody. Rather than adjusting the concentration of hIgG, which is difficult to quantify when bound, we instead altered the interior shape geometries between completely filled, partially filled, or having only an outer ring. The MDMs spread uniformly over micropatterns of each shape and, interestingly, the phagocytic forces was not observed to differ significantly between the three cases (Fig. 3-8c). This result agrees with previous work showing that Fc density has little effect on cellular decisions to phagocytose targets larger than 2 μms[31], and suggests that like the triggering of cytokine secretion in T cells[32], the phagocytic pathway leading to force generation acts in a digital manner, turning on completely at a certain threshold, but not scaling with opsonin signal quantity.

Next, we tested the hypothesis that forces involved in FcR-mediated phagocytosis should exceed the forces initiated by other adhesive opsonins, which can be similarly patterned with our fabrication process. Phagocytic contractions of hIgG "X" micropatterns were compared to contractions of micropatterns embedded with either fibrinogen (Fg) or vitronectin (Vn), both of which are molecules that support long term macrophage adhesion but with less understood immunological roles[33,34]. Non-opsonized DNS-BSA micropatterns were also used as a negative control for Fc-mediated response.

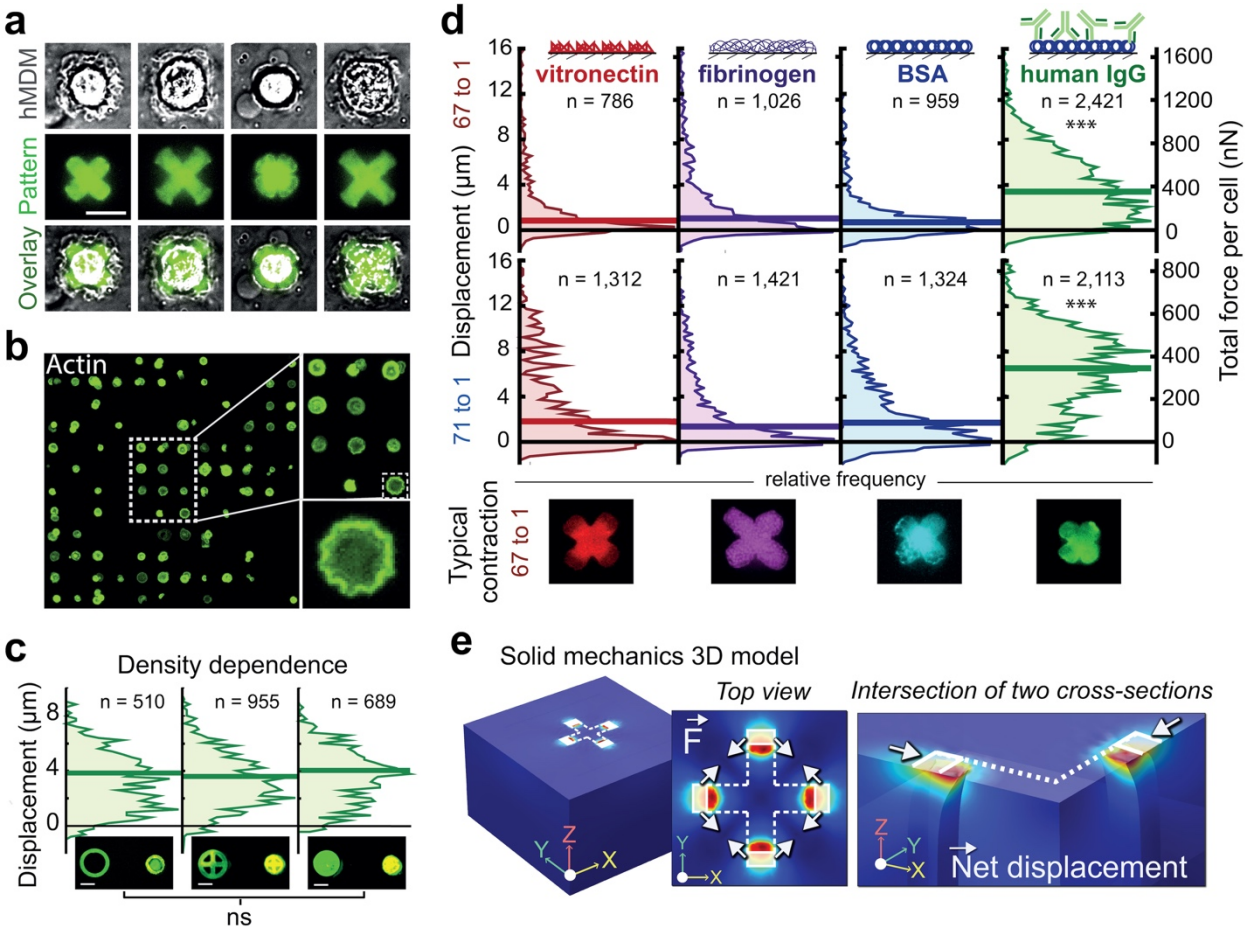

Figure 3-8: Measuring phagocytic forces generated by individual human macrophages

*(**a**) Representative images of hMDMs on hIgG cross patterns showing a range of phagocytic responses. (**b**) Representative image of actin-stained hMDMs spread over circular patterns in an array. High rates of single-cell pattern coverage are achieved. (**c**) Phagocytic contraction of i) ring, ii) cross and iii) filled hIgG circular patterns. The three distributions of single-cell responses were not significantly different. (**d**) Opsonin-dependence in phagocytic contraction. Vitronectin, fibrinogen, BSA, and hIgG were patterned in 50 μm cross shapes on a stiffer, 67:1 base:crosslinker (B:C) (top) and softer*

71:1 (bottom) substrate. HIgG elicited the most contractile response from the largest fraction of macrophages, consistent with the role and urgency of antibody opsonization in immunity. Left Y-axis represents displacement in μm; Right Y-axis represents applied forces in nN. A typical pattern representing each distribution in the 67:1 B:C case is shown below. N represents number of cells in each distribution shown in (c) and (d). ***(e)*** *Finite element method modeling of forces exerted by a phagocytosing macrophage. Forces were modeled as boundary loads on a linear elastic material, exerted between all pairs of adjacent terminals of the cross pattern. The shape of the non-displaced pattern is outlined in white and the 5μm by 10 μm area over which force is applied is shaded. LEFT: Complete geometry comprising a 150 μm by 150 μm elastic material with 90 μm thickness. MIDDLE: The top view showing the the direction of applied tangential forces, indicated by the arrows. RIGHT: Cross-sectional view of one quarter of the geometry at 50% opacity highlighting the response of the material to the boundary load and indicating the direction of net displacement. Note: Internal columns of material are depicted only to emphasize the displaced geometry due to applied forces and do not represent real boundaries in the material*

Compared to the other ligands, hIgG micropatterns experienced the largest contractions covering a broad range of magnitudes while micropatterns composed of Fg, Vn, and DNS-BSA generally experienced very little contraction, confirming our hypothesis. However, for each of these three other conditions, there was a small subpopulation of MDMs that did apply substantial contractile force, producing micropattern displacements that spanned the full range of magnitudes seen in the hIgG case. Although unexpected, it is conceivable that a subset of the MDMs, which were initially differentiated from a heterogeneous pool of monocytes[35], may become activated by these molecules through interactions with other (non-FcR) receptors, ultimately converging in

downstream signaling pathways leading to phagocytosis. Previous work demonstrating a limited role of vitronectin in enhancing target clearance by alveolar macrophages supports this interpretation[36].

Taking the micropattern displacements and material properties as inputs, we employed finite element method (FEM) solid mechanics modeling to approximate the forces that were applied onto the micropatterns, finding that MDMs engaged in FcR-mediated phagocytosis generated median forces of ~350 nN while a number of outlier cells were capable of forces as large as 1 μN (Fig. 3-8d-e). Force magnitudes in this range were also observed in small numbers MDMs seeded onto Fg, Vn and DNS-BSA, although the medians for each of these populations were significantly less, never exceeding 100 nN. Force magnitudes falling in the 10^{-7} N range have previously been reported for other human cells including mesenchymal cells, HUVECs[15], and keratinocytes[37]. It is expected that macrophages are capable of producing contractile forces of these magnitudes in the act of phagocytosis since the adhesive strengths of certain bacteria were found to approach the μN range[38]. This analysis represents the first direct quantification of the contractile forces involved in the closure of the phagocytic cup.

We also investigated whether IgG subclass dictated phagocytic force generation in MDMs. Immunoglobulin G (IgG) is a combination of four distinct IgG subclasses called IgG1, IgG2, IgG3, IgG4. Although highly conserved, these subclasses vary in their hinge regions which are involved in binding both FcR and the C1q subcomponent of the C1 complex[39]. A recent study also reported minor differences in their ability to stimulate phagocytic uptake of *Salmonella* bacterial cells by a monocytic cell line[40]. We asked whether these differences were triggered at the force-generation level. Using a humanized panel of the four subclasses of IgG antibodies we found that all four subclasses induced significant increases in phagocytic force over the non-opsonized controls,

without significant differences between them. We observed a similar result for another phagocyte, matched immature monocyte-derived dendritic cells (MDDCs) derived from the same patient (Fig. S5). Although a greater proportion of MDDCs possessed basal contractile activity than MDMs, their stimulated contractile force generation to all opsonized micropatterns was significantly greater than the non-opsonized controls, and similar to that of MDMs. Overall, the range of forces generated by both phagocytes in response to all four IgG subclasses were comparable. It is not entirely surprising that MDMs and MDDCs produced similar forces since both are professional phagocytes with the same general targets e.g. bacteria, parasites, debris. However, these results suggest that if phagocytic uptake efficiency does indeed differ among the subclasses, it is not a result of differences in force-generation.

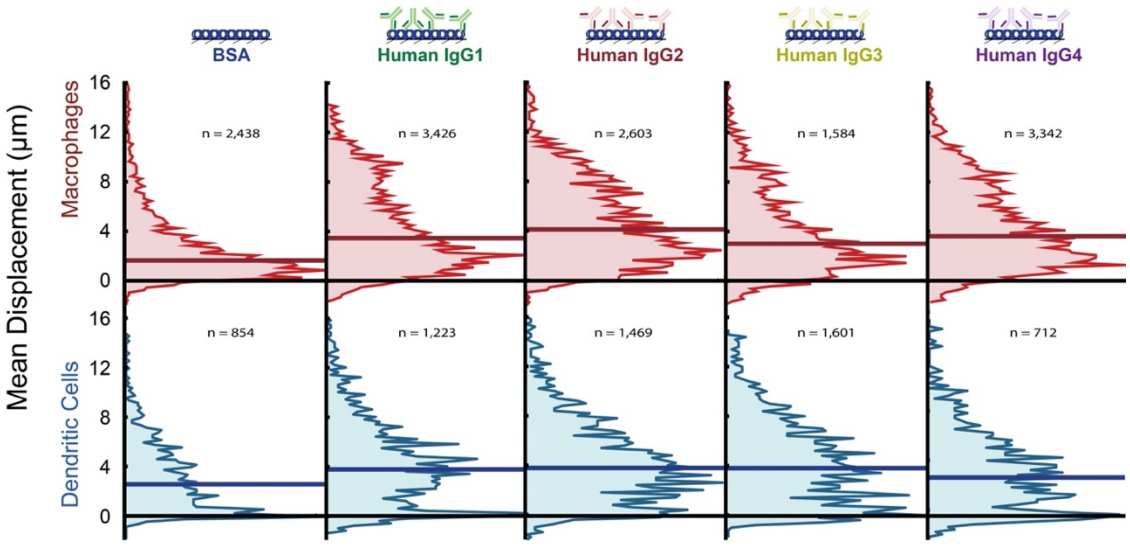

Figure 3-9: Comparison of phagocytic forces generated by human monocyte-derived dendritic cells and macrophages engaged in phagocytosis forces.

Patient-matched monocyte-derived macrophages (MDMs) and dendritic cells (MDCs) on patterns opsonized with various IgG isotypes. Although a greater

proportion of MDDCs possessed basal contractile activity than MDMs, their stimulated contractile force generation to all opsonized micropatterns was significantly greater than the non-opsonized controls, and similar to that of MDMs. No obvious differences in force-generation are observed across these isotypes and MDCs are observed to produce forces comparable to MDMs. This results indicate that IgG glycosylation patterns may not greatly contribute to the force-generating steps in phagocytosis.

Pharmacological inhibition of actin polymerization but not of phagosome acidification reduces phagocytic force

Actin polymerization has long been known to be required for phagocytosis, with target uptake assays showing that actin inhibitors greatly reduce phagocytic efficiency, particularly with Fc-opsonized targets[41]. Considering the direct involvement of actin polymerization in phagosomal formation and closure, it would seem logical that the inhibition of polymerization would reduce the phagocytic force. Following its closure, the internal phagosomal pH progressively decreases to create an intolerable environment and to activate pH-sensitive proteases, enhancing its microbicidal activity[42]. It remains unknown whether there is feedback between phagosome maturation and the sustained maintenance of a phagocytic force. We used the FLECS platform to both confirm the direct role of actin polymerization in phagocytic force generation and also to determine whether disruption of phagosomal acidification (a late-stage event) fed back into the control of the earlier mechanical stages of phagocytosis. In these experiments, we treated MDMs with either cytochalasin D or with chloroquine at three doses to block actin polymerization or phagosomal acidification, respectively. MDMs were either seeded directly into drug-containing medium or incubated with drug after achieving steady-state phagocytic contraction.

As expected, incubation with cytochalasin D at all tested doses substantially decreased the measured phagocytic contraction, while pre-treatment completely prevented any measureable contraction. This confirmed that actin polymerization is required for force-generation capacity during phagocytosis. Treatnent with chloroquine at any stage did not have a noticeable effect on the mechanical output of the macrophages, indicating the early-stage mechanical encapsulation and late–stage chemical maturation involved in phagocytic clearance are uncoupled in both the long-term and short-term.

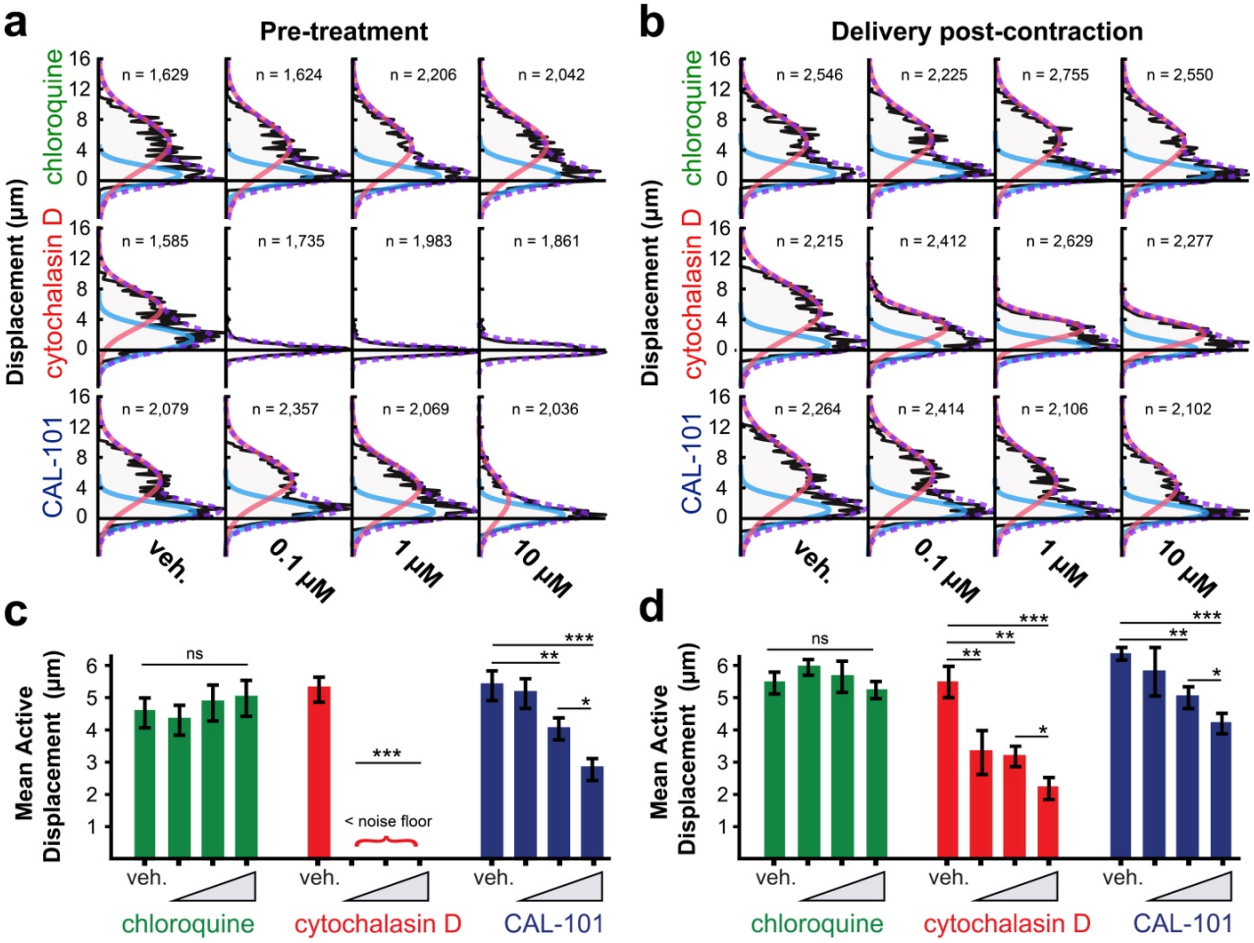

Figure 3-10: Effects of chloroquine, cytochalasin D and CAL-101 on hMDM contractile force

*(**a**) Contraction distributions of hMDMs engaging IgG-opsonized micropatterns pre-treated with DMSO or with three doses of each drug. (**b**) Contraction distributions of hMDMs engaging IgG-opsonized micropatterns incubated with DMSO or with three doses of each drug for 15 minutes after reaching steady-state contraction. In (a) and (b) Data are pooled from 4 technical replicates. A bimodal distribution was observed reflecting an "active" phagocytosing population (red curve) and a weakly adhered, inactive population (blue curve). A mixed Gaussian distribution is fitted to each plot to obtain information about the active populations which is used for quantification. N represents the number of cells in each distribution shown in (a) and (b). (**c**) and (**d**) median contraction levels of the active populations in (a), (b), respectively. Bars represent mean of 4 replicates + SEM. of no treatment and treatment with DMSO control.*

PI3K inhibition reduces the forces generated during FcR-mediated phagocytosis

Finally, we investigated the role of a specific phosphatidylinositide 3-kinase (PI3K) isoform, p110δ, in phagocytic force. Among their other functions in immunity, PI3Ks are also regulators of phagocytosis where they drive the re-arrangement of actin necessary for phagosome formation[43,44]. Class 1A PI3Ks – the p110α, p110β and p110δ isoforms -- positively regulate the small G protein Rac1[45], which coordinates actin organization and is required for FcR-mediated phagocytosis[46–48]. Of these, the p110δ isoform has also been shown to selectively reduce phosphorylation of Akt which is an upstream effector of FcR-mediated phagocytosis[49] and negatively regulate the PI3K antagonist, PTEN, in murine macrophages[50]. Thus, we posited that PI3Kδ inhibition would attenuate the forces generated in FcR-mediated phagocytosis. To evaluate

this, we subjected hMDMs contracting our hIgG micropatterns to three steps of 10-fold dilutions of the selective p110δ inhibitor, CAL-101.

We found that at the effective dose (ED) of 1 μM, compared to the vehicle control, CAL-101 produced statistically significant relaxations in micropatterns occupied by the active population of macrophages and at 10 μM the effect was even more pronounced indicating a dose-dependent response. Although pre-treatment with CAL-101 produced a more robust relaxation at all doses, the post-contraction incubation revealed the rapid onset of this effect (which became noticeable within 15 mins of compound addition), and corroborated the requirement of PI3K activity for sustained force generation. This observation shows for the first time that PI3K plays a direct role in phagocytic force generation. The partial suppression of baseline phagocytic force at the ED is consistent with reports that PI3K inhibition blocks phagocytosis of large targets but not smaller ones[43]. It is also possible that the redundant functions of the other class 1A PI3Ks helped to mitigate the relaxing effects of this selective p110δ inhibition. This observation is important to consider in terms of potential immunosuppresive side-effects of CAL-101 which, at the time of this writing, is in Phase 3 clinical trials for treatment of chronic lymphocytic leukemia (Clinical Trials Identifier NCT01539291).

Discussion

We introduce an integrated biosensor platform that enables robust, high-throughput analysis of large populations of contractile cells, with independently tunable material stiffness, pattern shape, and molecular composition, allowing it to be tailored to a broad range of cell types and their functions. This technology offers two principal advantages over existing methods for studying force biology of individual cells.

First, FLECS provides a tremendous increase in throughput, as demonstrated by the high N obtained in each experiment. We achieve this by reducing imaging time, simplifying the image processing problem, and eliminating manual cell selection and inspection steps. Unlike TFM and EMA which typically require 40X or 60X magnification and sometimes multiple time-points (e.g. stressed and unstressed), we obtain high resolution measurements using 10X images collected at a single time-point. Since our fundamental measurement is of micropattern shape change – which we have demonstrated is sufficiently informative of cellular force generation – the computational problem involves only binary image operations which are substantially simpler and more parallelizable than algorithms performing reconstruction of traction forces from strain fields. In contrast to TFM and EMA[51] where the user typically must locate and outline each cell that is to be analyzed, all such image processing is handled by our algorithm -- from locating all cells, to establishing baseline contraction levels, to calculating cell-induced substrate displacements and displaying the data.

As a result, a single experiment can yield hundreds to thousands of single-cell data points for uniformly adhered cells providing the statistical confidence required in drug discovery and candidate characterization, and even identification of new sub-populations within a cell preparation thought to be a single phenotype.

Second, the barrier-to-entry for biological laboratories studying force biology is lowered. Due to the comparative ease of substrate fabrication, control over cell adhesion, and simpler imaging requirements, many of the noted difficulties associated with operating the TFM and EMA technologies are simplified. As recently reported[8], TFM has strict protocol parameters to prevent the overlap of displacement fields generated by neighboring cells, and in addition to increasing computational expense, TFM calculations have been called complex and nuanced and require

significant expertise to properly implement. Our system avoids these complexities since the cells self-arrange onto our micropatterns, which are both spatially and mechanically segregated, and analysis of their displacements is intuitive and automated.

Furthermore, EMA fabrication can be technically challenging for labs not well trained in micro-fabrication since the silicon masters must have exact planar (post diameter) and depth (post height) dimensions which need to be confirmed using additional equipment post-fabrication for accurate force calculations. In comparison, preparation of PDMS stamps is relatively simple as there are no hard geometric constraints on the molds. Unlike EMA substrates, PDMS stamps are reusable indefinitely. Functionalizing the pillars is also non-trivial[8] and, more importantly, not always reliable since highly contractile cells can de-adhere adsorbed matrix from PDMS (Movie S8). Our sacrificial approach covalently embeds matrix proteins into the elastomeric films, preventing this issue.

Although the concept of inferring cellular forces from changes in micropattern shape has been proposed before by Tseng et al.[11], their initial work was limited to a proof-of-principle demonstration due primarily to the technical difficulty of generating robust micropatterns on ultrasoft substrates and their dependence on TFM. Our unique fabrication approach, in which proteins are first robustly stamped onto a stiff surface, overcomes the technical limitations that have precluded wide usage of this method by cell biology labs. We achieve superior micropattern uniformity (Fig. 2-5) over large areas (e.g. entire SLAS standard footprint) which allows normalization of cell-deformed micropatterns to be automated using the non-occupied micropatterns found in the same image set, rather than requiring cell removal, additional imaging and manual image registration. Noise resulting from geometric inconsistencies in the micropatterns is also largely removed, greatly improving the overall quality of the measurements.

Significantly, our materials cover a wider range of mechanical properties without compromising micropattern quality (e.g. lower than the 7 kPa limit reported by Tseng *et al.)* and support bonding to polystyrene bottomless well-plates, enabling parallelization.

FLECS has unique research and industrial applications. For example, the functionalization of our sensors with immunological molecules enables the study of phagocytosis of large targets. Whereas traditional phagocytosis assays are endpoint measurements that look at the total engulfment by phagocytes of exclusively smaller targets, our larger surface-bound targets are a good model for phagocytosis of tissue-like structures such as biofilms or tumor cells embedded in tissue. In addition to quantifying phagocytic force, this method could help determine which factors can lead to improved immune cell disruption of such pathogenic tissue-like structures.

This work also represents the first implementation of a cell traction force measurement technology in a high-throughput phenotypic screening configuration that maintains single-cell resolution. This development is significant since pharmaceutical companies currently lack the tools to access this force-generating phenotype in a drug discovery setting, despite the growing need for the development of new therapies for conditions related to aberrant cellular force-generation. Applications of this technology to such drug discovery is already ongoing and it is in this area that we anticipate our platform will have the greatest clinical impact.

Materials and Methods

Preparation of patterned ultra-soft substrates

The wafer-scale process is shown in Figure S6 and has been described in detail previously[23]. Briefly, a dextran solution (70 kDa from Sigma Aldrich) in deionized water was spin-coated onto plasma-activated silicon wafers and baked until dehydration to yield dextran substrates. Chrome photomasks containing arrays of micro-patterns were designed using L-Edit software, fabricated off-site, and used to pattern SPR 220 photoresist on separate silicon wafers. PDMS (Sylgard 184) at 10:1 ratio of base:crosslinker was cast onto the patterned wafer, cross-linked and demolded yielding stamps with positive pattern features. Adhesive biomolecule (e.g. ECM protein) solution was added to the stamp surface, incubated for 1 hr, and air-dried immediately before stamping. The stamped adhesive molecule or a co-stamped molecule was conjugated with a fluorescent moiety. Dextran substrates were activated with a brief plasma treatment and stamped with the biomolecule-adsorbed PDMS stamps for 5 minutes. Ultra-soft PDMS mixture (55:1 to 71:1) was spin-coated (1200 rpm, 20 s) over the stamped dextran-coated silicon, and cured (24 hrs RT followed by 7 days at 65 °C). Once cured, the substrate may be stored stably at room temperature for >9 months.

Releasing substrates and seeding with cells

To begin an experiment, the substrate is mounted onto cover glass (where the PDMS layer is in contact with the cover glass) and placed into saline solution to release the soluble dextran layer and yield a glass-backed elastomeric thin-film with embedded proteins. These substrates may

be fabricated to match the area of a standard SLAS well-plate footprint (~ 3 x 4.5 in) and mounted onto a bottomless polystyrene 96-well plates (Griener One Bio). Following fabrication, the sample is sterilized by washes in strong base followed by washes in sterile deionized water. Non-patterned regions are blocked in a 0.5% solution of Pluronics F-127 (45 mins, RT) and cells of interest are seeded. For live imaging experiments, Hoechst 33342 nuclear stain is added to the culture medium (1 μg mL^{-1} final concentration). If cells are to be fixed, the nucleus is stained after fixation. The sample is washed to remove non-adhered cells after 2 hr. At the conclusion of the experiment, the sample is either left unfixed or fixed in 4% paraformaldehyde solution at RT for 1 hr and mounted using DAPI-infused mounting medium, and imaged.

Imaging and image analysis

In our experiments, fluorescent patterns (green or red channel) and cell nuclei (blue channel) were imaged at 10X magnification with a Nikon fluorescent microscope in fixed-sample experiments, or with the ImageXpress® Micro XL High-Content Imaging System fluorescent microscope with 10X magnification in live experiments performed using the multi-well plate format. Image processing was performed with MATLAB.

A separate algorithm was developed for analyzing each pattern type. For experiments using cross ('X') patterns, a template is used to locate all patterns in all frames. The mean distance between the center and each terminal of each pattern comprises a data point. For experiments using circular patterns, the native MATLAB function *imfindcircles()* is used to identify all circular shapes in each frame and measure their radii. The presence or absence of a stained nucleus at the corresponding *xy* location of the nuclear image determines whether a given pattern is used for the

control data, experimental data, or is rejected as having multiple cells (Fig. 3-2). All experimental data measurements were zeroed to the median of the measurements of control case patterns yielding net displacement histogram plots. Raw measurements are also saved in a *.mat* format.

During processing, a file containing (i) an image of each cross pattern marked at the computed center and vertices, or an image of each circular pattern overlaid with the circle fitted by the *imfindcircles()* function, alongside (ii) an image of the corresponding nuclear signal labeled with the computed cell count, is created and saved for each pattern-nuclear signal pair for later viewing and quality control (Fig. 3-2b).

Study on mesenchymal stem cells:

Cell Culture and Differentiation

Human mesenchymal stem cells (hMSCs) derived from bone marrow or adipose tissue (StemPro) were maintained in MesenPRO RS™ Medium. Differentiation was induced by 14 day culture in adipogenic (StemPro Adipogenesis Differentiation Kit) or osteogenic (StemPro Osteogenesis Differentiation Kit) inductive medium as described in the manufacturer's manual. Trypsin-EDTA (.05%) was used to resuspend cells at the start of the experiment. Seeding and culturing on FLECS substrates was done in Dulbecco's modified Eagle medium (DMEM, Invitrogen) supplemented with 10% MSC Qualified FBS, 100 units mL^{-1} penicillin and 100 μg mL^{-1} streptomycin. Early passages (<7) of hMSCs were used in all experiments.

Substrate Parameters

Cross shaped patterns (70 μm diagonal, 10 μm bar thickness) spaced at 100 μm center-to-center vertical and horizontal distances were used for this experiment. Substrates we prepared by adsorbing 0.5 mL of 30 μg mL^{-1} fibronectin and 30 μg mL^{-1} Alexa Fluor 488-conjugated fibrinogen solution to each of six 22mm x 22mm stamps for 45 mins before stamping dextran-coated wafers. PDMS was mixed at a 55:1 base to crosslinker ratio.

Experimental Procedure

Substrates were housed in 6-well plates during the experiment. Cells were seeded by pipetting cell suspensions directly over the substrates. After 1hr, non-adhered cells were washed away. Cells were fixed with warmed 4% paraformaldehyde and the substrates were mounted onto glass slides using DAPI-infused mounting medium (ThermoFisher P-36931) 8 hours after seeding and later imaged.

Actin Staining

Following fixation and prior to mounting, a subset of all MSC samples were permeabilized with 0.25% Triton X-100 (Sigma) for 10 mins and incubated with 1:500 Alexa fluor-568 phalloidin (ThermoFisher, A12380) in PBS for 20 minutes at RT.

Study on tonic traction forces supplied by primary human smooth muscle cells:

Cell culture

Cryopreserved human primary bronchial, uterine, and aortic smooth muscle cells were purchased from Promocell. The cells were maintained in complete Smooth Muscle Medium (Promocell) supplemented with 100 units mL^{-1} penicillin and 100 μg mL^{-1} streptomycin. Trypsin-EDTA (.05%) was used to re-suspend cells at the start of the experiment. Seeding and culturing on FLECS substrate was also done in Complete SMC 2 Medium (Promocell). The experiment comparing contractile responses of these three cell types was performed with 3rd passage cells, and the experiment correlating alpha smooth muscle actin with contraction was performed with 4th passage uterine smooth muscle cells.

Alpha smooth muscle staining

After an 8 hr culture on the soft substrates as described above, uterine smooth muscle cells were fixed with warmed 4% paraformaldehyde, permeabilized with 0.25% Triton X-100 (Sigma) for 10 mins and incubated with anti-alpha smooth muscle actin-FITC (Sigma) at a 1:200 dilution in PBS for 1 hr. Intensity was determined by sampling all of the pixel values of the loss-less .tif format images within the bounding box defined using uncontracted pattern dimensions, centered at the sites of patterns adhered to by cells.

Pharmacological studies in primary human airway smooth muscle cells:

Cell culture

Primary human airway smooth muscle (HASM) cells were a gift from Prof. Panettieri and were cultured as up to 4th passage as previously described[52,53]. Cells were seeding into a 96-well FLECS-plate at approx. 6000 cells per well and allowed to adhere for 2 hours. For experiments on stimulating contracting, serum was removed for 48 hours before pro-contractile agonists were added.

Pro-contractile agonists.

Endothelin-1, bradykinin (bradykinin acetate salt) and histamine were purchased from Sigma Aldrich. Endothelin-1 was dissolved in 1% acetic acid, histamine and bradykinin were dissolved in water. Each compound was aliquoted and frozen until the experiment, at which point they were diluted to the working concentration is serum-free HASM medium.

Drug delivery.

Endothelin-1 (100 nM), bradykinin (1 μM) and histamine (10 μM) were diluted to their working concentrations and dispensed directly into the wells containing pre-adhered and serum-starved HASM cells. For live videos, fixed sites in wells receiving the drugs were imaged at 1 minute intervals for 30 mins (4x objective, 1.5x eye-piece) on an incubated microscope. For quantitative analysis, the FLECS-plates were incubated for 20 minutes after drug delivery after which point each the wells of interest (4 wells per drug) were imaged using the Molecular Devices ImagXpress High Content Imager.

Blebbistatin titration.

Blebbistatin (Sigma Aldrich) was dissolved in DMSO to achieve working concentrations using 10 steps of 2-fold dilutions beginning with 25 μM. HASM cells were seeded 24 hrs prior to treatment with blebbistatin. On the day of the experiment, cells were stained with Hoechst, washed, treated with blebbistatin (1% DMSO final concentration), incubated for 30 mins and imaged live using the ImageXPress Micro XL High Content Imaging System.

Phagocyte experiments:

Macrophage Differentiation.

Human peripheral blood monocytes were isolated from blood taken from healthy adult donors using density gradient centrifugation with Histopaque®-1077 solution (Sigma) according to UCLA IRB protocol #14-000522. Collected mononuclear cells were washed in saline, resuspended in unsupplemented RPMI 1640 medium (Life Technologies) and allowed to adhere to the well surfaces within polystyrene 6-well-plates for 2 hrs. The wells were then washed to remove contaminating lymphocytes and refilled with warm RPMI 1640 medium supplemented with 20% heat inactivated FCS, 20 ng mL^{-1} M-CSF (Life Technologies), 100 units mL^{-1} penicillin and 100 μg mL^{-1} streptomycin. Monocytes were allowed to differentiate into macrophages (hMDM) for 7 days. All macrophages were used within this period as phagocytic force was significantly reduced in macrophages aged >14 days and completely suppressed in macrophages aged 21 days **(**Fig. 3-11). To begin an experiment, macrophages were dissociated from the well-

plates by incubation in StemPro® Accutase® (Life Technologies) for 30 mins at 37ºC, followed by vigorous pipetting up and down to complete dissociation. Macrophages were resuspended in RPMI 1640 medium supplemented with 10% heat inactivated FCS, 100 units mL^{-1} penicillin and 100 μg mL^{-1} streptomycin before seeding onto FLECS chips. Macrophages were imaged live without fixing in all experiments and Hoechst 33342 (1 μg mL^{-1}) was used to stain cell nuclei.

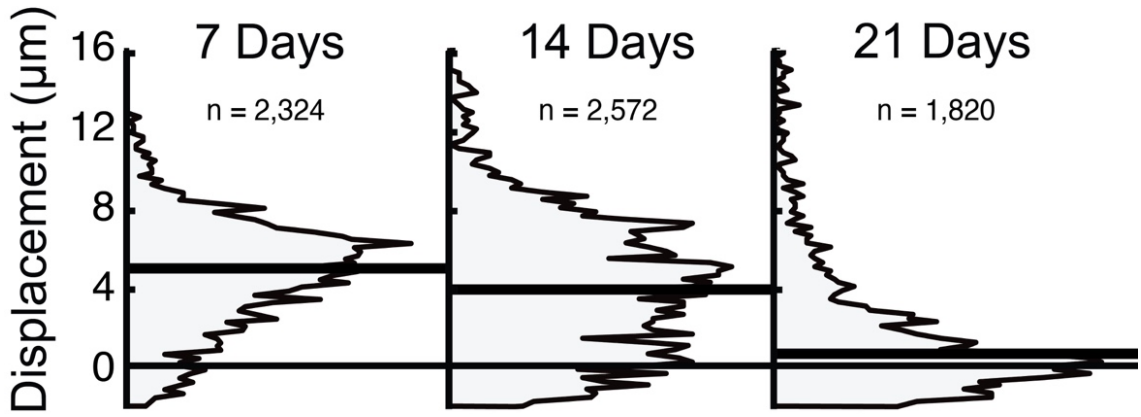

Figure 3-11: **Macrophages senesce following long term in vitro culture**.

Phagocytic forces produced by human monocyte-derived macrophages at different times after differentiation. Macrophages were seeded on hIgG cross patterns (50 μm diagonal, 10 μm bar thickness) for 6 hrs at 7 days, 14 days, or 21 days after initiating differentiation of monocytes. At 14 days, the phagocytic force response diminished substantially for a large portion of the macrophages and at 21 days, the large majority of macrophages applied little or no phagocytic force. For this reason, all macrophage experiments were performed using newly differentiated macrophages.

Dendritic Cell Differentiation.

Dendritic cells were prepared in the same manner as macrophages but using differentiation medium containing 100ng/mL GM-CSF and 50 ng/mL IL-4 instead of M-CSF.

Patterning Antibodies.

To pattern IgG `antibodies, a 45 μg mL^{-1} dansyl-conjugated bovine serum albumin and 45 μg mL^{-1} Alexa Fluor 488-conjugated bovine serum albumin solution was adsorbed to a stamp and stamped onto a dextran-coated wafer. After the substrates were coated with PDMS, cured, released and blocked with Pluronic F127 but before seeding macrophages, approximately 50 μL per 400 mm^2 of 25 μg mL^{-1} solution of human-mouse chimeric anti-dansyl IgG antibodies was spread over each patterned substrate and incubated for 3 hrs at RT. Excess antibody was then washed with saline. The human-mouse chimeric antibodies were developed by Morrison *et al*[54].

Density-Dependence Experiment.

Circular patterns with 54 μm diameters but with various degrees of filling were patterned with IgG as described above. Specifically, (i) a ring pattern with 10 μm thickness (inner diameter subtracted from the outer diameter), (ii) the same ring pattern encircling a symmetric cross shape with 10 μm bar thickness and (iii) a solid circle were patterned. PDMS was mixed at a 65:1 base to crosslinker ratio. Macrophages were imaged 6 hours after seeding.

Opsonin-Dependence Experiment.

Human recombinant vitronectin (Advanced Biomatrix), fibrinogen (Life Technologies), BSA (Life Technologies) both conjugated with Alexa Fluor 488, and hIgG (as described above) were patterned in cross shapes (50 μm diagonal and 20 μm bar thickness). The total quantities of each ligand were set to be approximately uniform by modulating the concentrations of the adsorbing ligands and confirmed by measuring fluorescent intensities of resulting transferred patterns **(**Table 3-1**).** Macrophages were dissociated as described, seeded, and imaged live 6 hours later. PDMS was mixed at both 67:1 and 71:1 base to crosslinker ratios.

Opsonin	**Degree of labeling (mol dye per mol protein), *DOL***	**Concentration used**	**Actual fluorescent intensity (a.u.), *FI***	**Fraction of patterned protein that is labeled, $Frac_{labeled}$**	**Relative surface molarity coefficient, C_{sm}***
BSA	**7**	**60 μg mL^{-1}**	**519 +/- 35**	**0.5**	**148.5**
Vitronectin	**6.25**	**30 μg mL^{-1}**	**963 +/- 45**	**1**	**154.1**
Fibrinogen	**6**	**10 μg mL^{-1}**	**1073 +/- 51**	**1**	**178.8**

Table 3-1: Summary of opsonin normalization procedure

**The relative surface molarity coefficient is simply the measured fluorescent intensity normalized by the degree of labeling (moles dye per mole of opsonin) and adjusted for the proportion of opsonin that was fluorescently labeled.*

$$C_{sm} = (FI / DOL) \times frac_{labeled}^{-1}$$

This coefficient reflects the relative amounts of each opsonin that were transferred to the substrates but does not indicate absolute molar quantity. The coefficients calculated for the substrates used in the opsonin-dependent phagocytosis experiment do not vary significantly between the three opsonins indicating similar molar quantities in the patterns of the final substrates that were used in experiments. Since only one-half of all present BSA was labeled with Alexa Fluor 488, the relative surface concentration was expected to be twice the amount predicted by the DOL. This factor of 2 is reflected in the relative surface molarity calculated for BSA.

Patterning equal quantities of different opsonins.

Testing the phagocytic force response of hMDMs as a function of opsonin type required patterning of 3 different ligands: vitronectin, fibrinogen, dansyl-BSA, (hIgG was not patterned but rather used to bind the dansyl-BSA in which the conjugated dansyl group served as the binding site for the IgG antibodies). To decouple the potential effects of differential opsonin quantities from opsonin type, we set out to equalize the molar quantities of each opsonin on our substrates. To accomplish this, each opsonin was labeled with the same fluorophore (Alexa Fluor 488) and the respective degree of labeling (DOL) along with the fluorescent intensities of the patterns, as a function of solution concentration (used in the adsorption step), were used to achieve the same final surface densities. For each fluorescence intensity measurement, 10X magnification and 2 s exposure times were used.

Fibrinogen.

Alexa Fluor 488-conjugated fibrinogen was purchased from Life Technologies (Catalog #F13191, Lot #1636855) with a DOL of 6. This was the same ligand as was used for the hMSC and dose-response experiments and was adsorbed to the PDMS stamps for 45 mins before being stamped onto the dextran-coated wafers for 5 mins. Three concentrations (30, 20 and 10 μg mL-1) were tested to create a concentration vs. fluorescent intensity curve.

BSA.

Alexa Fluor 488-conjugated BSA was purchased from Life Technologies (Catalog #A13100, Lot #1348652) with a DOL of 7. Alexa Fluor 488-conjugated BSA (AF488-BSA) was co-patterned with dansyl-BSA since the former was used for fluorescently visualizing the pattern while the latter contained the epitope (dansyl) targeted by our human-mouse chimeric antibody. Thus, the two BSA molecules were patterned in equal quantities at three concentrations (60, 30 and 20 μg mL-1 each) to create a concentration vs. fluorescent intensity curve. In addition to the general procedure, the PDMS stamps were plasma treated before adsorption to promote wetting and during stamping, the stamps were kept in contact with the dextran-coated wafers under weight for 20 min rather than 5 min.

HIgG.

BSA patterns were prepared as described with the addition of hIgG (50 µL of 25 µg mL^{-1} solution per 400 mm^2) after the release, sterilization and blocking steps.

Vitronectin.

Human recombinant vitronectin was purchased from Advanced Biomatrix (Catalog #5052) and conjugated with Alexa Fluor 488 in-house using Alexa Fluor 488 carboxylic acid, succinimidyl ester (Life Technologies) at a 8:1 fluorophore to protein molar ratio in PBS (4 hrs, 4C). Following the reaction, the vitronectin solution was dialyzed against PBS for 48 hours with PBS changes every 12 hours to remove unreacted dye. The DOL for the vitronectin-Alexa Fluor 568 conjugate was calculated to be 6.25 using absorbance readings taken at 494 and 280 nm, as prescribed in the manufacturer's manual provided with the conjugation kit from Life Technologies, and using 1.02 .mL mg^{-1} cm^{-1} as the extinction coefficient for vitronectin[55]. Three concentrations (40, 30 and 20 µg mL^{-1}) were tested to create a concentration vs. fluorescent intensity curve. Like with BSA, the stamps were plasma-treated before adsorption and the stamps were kept in contact with the dextran-coated wafers under weight for 20 mins.

BSA.

BSA was found to saturate in fluorescent intensity when 30 µg mL^{-1} and higher concentrations were used for each BSA conjugate. However, concentrations of 60 µg mL^{-1} produced the most consistent transfers so this concentration was chosen for BSA. This maximum BSA intensity was normalized by the DOL for BSA and adjusted by a factor of 2 to account for

the equal part of non-fluorescent BSA (dansyl-BSA). Referencing this target normalized intensity (termed the 'relative surface molarity coefficient'), along with the concentration vs. fluorescent intensity curves constructed for vitronectin and fibrinogen and their DOLs, we predicted the adequate concentrations to be 30 μg mL^{-1} and 10 μg mL^{-1} for vitronectin and fibrinogen, respectively.

Approximation of phagocytic forces:

Substrate stiffness measurement.

Cylindrical PDMS samples (67:1 and 71:1) were placed onto an Instron tensile tester (Model 5564, Norwood, MA) with a 2.5 N load cell and compressive testing of the sample was performed at strain rate of 1 mm/min for a total indentation of 1.5 mm. The data was used to generate load-displacement curves. The slope of the linear portion of the curve, the cross-sectional area of the indentation tip and the PDMS sample heights were used to calculate stiffness. Three samples of each stiffness were test after 1 week and after 3 weeks of curing (Fig. 3-12). The results showed no significant stiffening after 1 week indicating the polymer was fully cured at one week and these unchanging stiffness values could be used for modeling cellular traction forces. The mean calculated stiffnesses were used in force approximations.

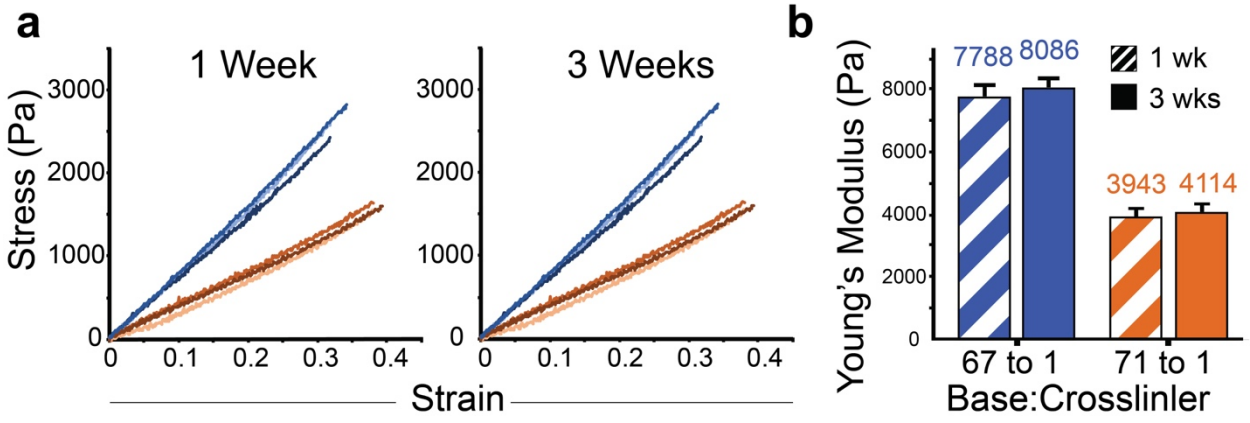

Figure S9. Mechanical testing of PDMS used in macrophage experiments.

PDMS samples at 67:1 and 71:1 base:crosslinker ratios were cured for 1 or 3 weeks, cut into cylinders and compression tested using an Instron 5564. Strain-stress curves ***(a)*** *and geometric characteristics of the sample and tip were used to compute the stiffness.* ***(b)*** *The stiffness did not increase between 1 week and 3 weeks of curing at 65 C for either formulation. These values were used for approximating the forces generated by phagocytosing macrophages.*

Finite element method modeling.

To approximate forces applied by phagocytosing macrophages on the ultra-soft substrates, the FLECS 'X' pattern was simulated using finite element model software, COMSOL (COMSOL, Inc.). Specifically, a single cross-shaped pattern corresponding to the experimental patterns (50 μm diagonal, 10 μm bar thickness) was simulated. We modeled the ultra-soft substrates as linear elastic materials with Young's moduli: 4000 Pa, 7900 Pa (corresponding to 71:1 and 67:1 PDMS rations, respectively) density: 970 kg/m^3, Poisson's ratio: .49999, and the forces exerted by macrophages as boundary loads directed tangentially between all pairs of adjacent terminals of the

'X' pattern. The substrate was modeled as a 150 μm by 150 μm film with thickness of 90 μm and was discretized into tetrahedral mesh elements. A 90 μm thickness was selected to minimize computational intensity associated with higher degrees of freedom, as thicknesses greater than 70 μm did not yield significant changes in pattern deflection for a given applied force. (Empirically, substrates were determined to be approximately 110 μm thick by using an automated fluorescent microscope to find the two focal planes containing either the embedded patterns or the glass substrate and calculating the distance between them). The bottom of the modeled substrate was assigned a fixed boundary condition (displacement = 0) and tangential forces ranging from 1 nN to 250 nN were applied to 5 μm by 10 μm regions on the top surface of the modeled substrate at the vertices of the pattern. In order to compute the pattern displacement due to an applied force, max values of the in-plane deformation were calculated on the four edges of the pattern region. Due to symmetry, the points of maximum displacement were located at the centerpoints of each terminal boundary, which is the same location the imaging analysis algorithm measures displacement.

For this model, the key assumptions of elasticity and linearity hold. Relaxation of contracted cells with the myosin inhibitor blebbistatin results in patterns returning to their unperturbed size and shape, suggesting elastic behavior and a lack of plastic deformation (Movie S4). Additionally, previous work has demonstrated that PDMS behaves as a linearly elastic material under quasi-static loading conditions[56]. Finally, the observed deflections of the substrate are small in comparison to the size of the substrate so we do not expect significant departures from linearity. This model is similar to that employed by Oakes PW, *et al.*[4] , though our system allows for direct measurement of substrate deflection, removing the need for including the cell in the simulation.

Macrophage drug panel

Experimental.

Cell culture and substrate preparation was identical to our earlier macrophage experiments, but using exclusively hIgG patterns. Chloroquine, CAL-101, and cytochalasin D were dissolved in medium or DMSO and delivered to FLECS-plate wells at final concentrations of 0.1, 1 and 10 μM either before macrophages were seeded, or after macrophages had maintained adhesion to the patterns for 24 hours. In the former case, imaging was done 24 hours later. In the latter, imaging was done 15 minutes after addition of the drug.

Analysis.

Since an inactive subpopulation of macrophages was prevalent in the overall population, we fitted a mixed Gaussian curve to each distribution using the open-source MATLAB function *peakfit.m* developed by Prof. Tom O'Haver from the University of Maryland. For obtaining the best fit, the two Gaussian widths were restricted to a minimum of 1 but were otherwise unconstrained. In each case (except with pre-treatment with cytochalasin D), two Gaussians were clearly identified in the best fit representing the inactive (near-zero contraction) and active populations. Overall curve fit error rates were low at <7% and R-squared values were all > 0.93. The central positions of the Gaussian's representing the active populations were used for quantifying the contractile capability of the macrophages following treatment with vehicle or drug.

Statistical Analysis:

For all statistical tests, P-values < 0.05 were considered significant, unless requiring multi-test corrections, in which case the appropriate Bonferoni correction was applied.

Mesenchymal stem cell experiment.

The Kruskal-Wallis test for non-parametric data was used to perform perform statistical analysis on the contractile distributions (implemented in MATLAB using the *kruskallwallis()* and *multcompare()* functions).

Pro-contractile stimulation of HASM cells.

Each condition (3 drugs and vehicle controls for each) was performed in 4 technical replicates. Drug treatments were compared to their vehicle controls using a two-tailed student's t-test applied to the medians of measured contractile distributions. The effects of the three drug treatments we're compared head-on using ANOVAs followed by pairwise two-tailed Bonferoni t-tests applied to the percentages of the population exhibiting positive contractile shifts.

Blebbistatin titration.

Each concentration of blebbistatin was tested in 4 technical replicates. Median contraction at each concentration was normalized by vehicle-treated contraction. GraphPad Prism 6 graphing

software was used to fit a sigmoid curve to the dose-response data and calculate the half maximal inhibitory concentration.

Macrophage experiments.

The Kruskal-Wallis test for non-parametric data was used to perform perform statistical analysis on the contractile distributions for the opsonin-dependence experiment. For the density dependence experiment, a one-way ANOVA ruled out any significant differences. For the macrophage drug panel, the central positons of active populations in each distribution (extracted using curve-fitting) were compared using ANOVAs followed by two-tailed Bonferoni t-tests. Each condition was performed in 4 technical replicates.

Bibliography

1. Munevar, S., Wang, Y. & Dembo, M. Traction force microscopy of migrating normal and H-ras transformed 3T3 fibroblasts. *Biophys. J.* **80,** 1744–1757 (2001).

2. Park, C. Y. *et al.* High-throughput screening for modulators of cellular contractile force. *Integr. Biol. Quant. Biosci. Nano Macro* **7,** 1318–1324 (2015).

3. Tan, J. L. *et al.* Cells lying on a bed of microneedles: An approach to isolate mechanical force. *Proc. Natl. Acad. Sci.* **100,** 1484–1489 (2003).

4. Oakes, P. W., Banerjee, S., Marchetti, M. C. & Gardel, M. L. Geometry Regulates Traction Stresses in Adherent Cells. *Biophys. J.* **107,** 825–833 (2014).

5. Rodriguez, M. L. *et al.* Measuring the contractile forces of human induced pluripotent stem cell-derived cardiomyocytes with arrays of microposts. *J. Biomech. Eng.* **136,** 051005 (2014).

6. Ricart, B. G., Yang, M. T., Hunter, C. A., Chen, C. S. & Hammer, D. A. Measuring Traction Forces of Motile Dendritic Cells on Micropost Arrays. *Biophys. J.* **101,** 2620–2628 (2011).

7. Legant, W. R. *et al.* Multidimensional traction force microscopy reveals out-of-plane rotational moments about focal adhesions. *Proc. Natl. Acad. Sci.* **110,** 881–886 (2013).

8. Polacheck, W. J. & Chen, C. S. Measuring cell-generated forces: a guide to the available tools. *Nat. Methods* **13,** 415–423 (2016).

9. Wang, N., Ostuni, E., Whitesides, G. M. & Ingber, D. E. Micropatterning tractional forces in living cells. *Cell Motil. Cytoskeleton* **52,** 97–106 (2002).

10. Rape, A., Guo, W. & Wang, Y. The Regulation of Traction Force in Relation to Cell Shape and Focal Adhesions. *Biomaterials* **32,** 2043–2051 (2011).

11. Tseng, Q. *et al.* A new micropatterning method of soft substrates reveals that different tumorigenic signals can promote or reduce cell contraction levels. *Lab. Chip* **11,** 2231–2240 (2011).

12. Tseng, P., Pushkarsky, I. & Carlo, D. D. Metallization and Biopatterning on Ultra-Flexible Substrates via Dextran Sacrificial Layers. *PLOS ONE* **9,** e106091 (2014).

13. Tseng, P. & Di Carlo, D. Substrates with Patterned Extracellular Matrix and Subcellular Stiffness Gradients Reveal Local Biomechanical Responses. *Adv. Mater.* **26,** 1242–1247 (2014).

14. Han, S. J., Bielawski, K. S., Ting, L. H., Rodriguez, M. L. & Sniadecki, N. J. Decoupling Substrate Stiffness, Spread Area, and Micropost Density: A Close Spatial Relationship between Traction Forces and Focal Adhesions. *Biophys. J.* **103,** 640–648 (2012).

15. Fu, J. *et al.* Mechanical regulation of cell function with geometrically modulated elastomeric substrates. *Nat. Methods* **7,** 733–736 (2010).

16. Kim, H. R., Appel, S., Vetterkind, S., Gangopadhyay, S. S. & Morgan, K. G. Smooth muscle signalling pathways in health and disease. *J. Cell. Mol. Med.* **12,** 2165–2180 (2008).

17. Torr, E. E. *et al.* Myofibroblasts exhibit enhanced fibronectin assembly that is intrinsic to their contractile phenotype. *J. Biol. Chem.* jbc.M114.606186 (2015). doi:10.1074/jbc.M114.606186

18. Arora, P. D. & McCulloch, C. A. Dependence of collagen remodelling on alpha-smooth muscle actin expression by fibroblasts. *J. Cell. Physiol.* **159,** 161–175 (1994).

19. Panettieri, R. A., Murray, R. K., DePalo, L. R., Yadvish, P. A. & Kotlikoff, M. I. A human airway smooth muscle cell line that retains physiological responsiveness. *Am. J. Physiol.* **256,** C329–335 (1989).

20. Maxwell, M. J., Goldie, R. G. & Henry, P. J. Ca2+ signalling by endothelin receptors in rat and human cultured airway smooth muscle cells. *Br. J. Pharmacol.* **125,** 1768–1778 (1998).

21. Hubmayr, R. D. *et al.* Pharmacological activation changes stiffness of cultured human airway smooth muscle cells. *Am. J. Physiol. - Cell Physiol.* **271,** C1660–C1668 (1996).

22. Limouze, J., Straight, A. F., Mitchison, T. & Sellers, J. R. Specificity of blebbistatin, an inhibitor of myosin II. *J. Muscle Res. Cell Motil.* **25,** 337–341

23. Straight, A. F. *et al.* Dissecting Temporal and Spatial Control of Cytokinesis with a Myosin II Inhibitor. *Science* **299,** 1743–1747 (2003).

24. Renkawitz, J. & Sixt, M. Mechanisms of force generation and force transmission during interstitial leukocyte migration. *EMBO Rep.* **11,** 744–750 (2010).

25. Protrusive and Contractile Forces of Spreading Human Neutrophils. Available at: http://www.sciencedirect.com/science/article/pii/S0006349515006608. (Accessed: 5th September 2016)

26. Linder, S. & Wiesner, C. Tools of the trade: podosomes as multipurpose organelles of monocytic cells. *Cell. Mol. Life Sci. CMLS* **72,** 121–135 (2015).

27. Labernadie, A. *et al.* Protrusion force microscopy reveals oscillatory force generation and mechanosensing activity of human macrophage podosomes. *Nat. Commun.* **5,** 5343 (2014).

28. Bashour, K. T. *et al.* CD28 and CD3 have complementary roles in T-cell traction forces. *Proc. Natl. Acad. Sci. U. S. A.* **111,** 2241–2246 (2014).

29. Barda-Saad, M. *et al.* Dynamic molecular interactions linking the T cell antigen receptor to the actin cytoskeleton. *Nat. Immunol.* **6,** 80–89 (2005).

30. Basu, R. *et al.* Cytotoxic T Cells Use Mechanical Force to Potentiate Target Cell Killing. *Cell* **165,** 100–110 (2016).

31. Pacheco, P., White, D. & Sulchek, T. Effects of Microparticle Size and Fc Density on Macrophage Phagocytosis. *PLOS ONE* **8,** e60989 (2013).

32. Wertek, F. & Xu, C. Digital response in T cells: to be or not to be. *Cell Res.* **24,** 265–266 (2014).

33. McNally, A. K., Jones, J. A., Macewan, S. R., Colton, E. & Anderson, J. M. Vitronectin is a critical protein adhesion substrate for IL-4-induced foreign body giant cell formation. *J. Biomed. Mater. Res. A* **86,** 535–543 (2008).

34. Labernadie, A., Thibault, C., Vieu, C., Maridonneau-Parini, I. & Charrière, G. M. Dynamics of podosome stiffness revealed by atomic force microscopy. *Proc. Natl. Acad. Sci. U. S. A.* **107,** 21016–21021 (2010).

35. Gordon, S. & Taylor, P. R. Monocyte and macrophage heterogeneity. *Nat. Rev. Immunol.* **5,** 953–964 (2005).

36. Perry, D. G., Wisniowski, P., Daugherty, G. L., Downing, J. & Martin, W. J. Nonimmune phagocytosis of liposomes by rat alveolar macrophages is enhanced by vitronectin and is vitronectin-receptor mediated. *Am. J. Respir. Cell Mol. Biol.* **17,** 462–470 (1997).

37. Soon, C. F., Tee, K. S., Youseffi, M. & Denyer, M. C. T. Tracking Traction Force Changes of Single Cells on the Liquid Crystal Surface. *Biosensors* **5,** 13–24 (2015).

38. Tsang, P. H., Li, G., Brun, Y. V., Freund, L. B. & Tang, J. X. Adhesion of single bacterial cells in the micronewton range. *Proc. Natl. Acad. Sci.* **103,** 5764–5768 (2006).

39. Vidarsson, G., Dekkers, G. & Rispens, T. IgG Subclasses and Allotypes: From Structure to Effector Functions. *Front. Immunol.* **5,** (2014).

40. Goh, Y. S. *et al.* Human IgG isotypes and activating Fcγ receptors in the interaction of Salmonella enterica serovar Typhimurium with phagocytic cells. *Immunology* **133,** 74–83 (2011).

41. Kaplan, G. Differences in the Mode of Phagocytosis with Fc and C3 Receptors in Macrophages. *Scand. J. Immunol.* **6,** 797–807 (1977).

42. Hackam, D. J., Rotstein, O. D. & Grinstein, S. in *Advances in Cellular and Molecular Biology of Membranes and Organelles* (ed. Gordon, S.) **5,** 299–319 (JAI, 1999).

43. Schlam, D. *et al.* Phosphoinositide 3-kinase enables phagocytosis of large particles by terminating actin assembly through Rac/Cdc42 GTPase-activating proteins. *Nat. Commun.* **6,** 8623 (2015).

44. Beemiller, P. *et al.* A Cdc42 Activation Cycle Coordinated by PI 3-Kinase during Fc Receptor-mediated Phagocytosis. *Mol. Biol. Cell* **21,** 470–480 (2010).

45. Papakonstanti, E. A. *et al.* Distinct roles of class IA PI3K isoforms in primary and immortalised macrophages. *J. Cell Sci.* **121,** 4124–4133 (2008).

46. Lee, D. J., Cox, D., Li, J. & Greenberg, S. Rac1 and Cdc42 are required for phagocytosis, but not NF-kappaB-dependent gene expression, in macrophages challenged with Pseudomonas aeruginosa. *J. Biol. Chem.* **275,** 141–146 (2000).

47. Castellano, F., Montcourrier, P. & Chavrier, P. Membrane recruitment of Rac1 triggers phagocytosis. *J Cell Sci* **113,** 2955–2961 (2000).

48. Massol, P., Montcourrier, P., Guillemot, J.-C. & Chavrier, P. Fc receptor-mediated phagocytosis requires CDC42 and Rac1. *EMBO J.* **17,** 6219–6229 (1998).

49. Ganesan, L. P. *et al.* The Serine/Threonine Kinase Akt Promotes Fcγ Receptor-mediated Phagocytosis in Murine Macrophages through the Activation of p70S6 Kinase. *J. Biol. Chem.* **279,** 54416–54425 (2004).

50. Papakonstanti, E. A., Ridley, A. J. & Vanhaesebroeck, B. The p110δ isoform of PI 3-kinase negatively controls RhoA and PTEN. *EMBO J.* **26,** 3050–3061 (2007).

51. Goedecke, N., Bollhalder, M., Bernet, R., Silvan, U. & Snedeker, J. Easy and Accurate Mechano-profiling on Micropost Arrays. *J. Vis. Exp. JoVE* (2015). doi:10.3791/53350

52. Panettieri, R. A. Isolation and culture of human airway smooth muscle cells. *Methods Mol. Med.* **56,** 155–160 (2001).

53. Koziol-White, C. J. *et al.* Inhibition of PI3K promotes dilation of human small airways in a rho kinase-dependent manner. *Br. J. Pharmacol.* (2016). doi:10.1111/bph.13542

54. Morrison, S. L., Johnson, M. J., Herzenberg, L. A. & Oi, V. T. Chimeric human antibody molecules: mouse antigen-binding domains with human constant region domains. *Proc. Natl. Acad. Sci.* **81,** 6851–6855 (1984).

55. Characterization of the Denaturation and Renaturation of Human Plasma Vitronectin. II. Investigation Into the Mechanism of Formation of Multimers. *PubMed Journals* Available at: https://ncbi.nlm.nih.gov/labs/articles/8663085/. (Accessed: 24th February 2017)

56. Vanlandingham, M. R., Chang, N.-K., Drzal, P. L., White, C. C. & Chang, S.-H. Viscoelastic characterization of polymers using instrumented indentation. I. Quasi-static testing. *J. Polym. Sci. B Polym. Phys.* **43,** 1794–1811 (2005).

Chapter 4:

Connecting single-cell force generation to organ models and *in vivo* responsiveness

In Chapter 3, we introduced the FLECS platform, a powerful high-throughput assay that provides data on cellular contractility for hundreds of thousands of cells simultaneously, at the single-cell level. We demonstrate its utility in profiling the functional mechanical forces generated through not only cellular level processes such as mechanosensing by mesenchymal stem cells or phagocytosis by human macrophages and dendritic cells, but also of those generated by individual myocytes which *in vivo* operate as cohesive ensembles comprising whole organs. In particular, we examined the tonic contractility of primary human smooth muscle cells isolated from human airways (bronchial/tracheal), human aorta, and human myometrium, as well as some of their contractile responses to challenges with pro-contractile agonists. Beyond the clear applications this tool should have in basic biological research, we concluded Chapter 3 by proposing to use this system as a screening and drug discovery tool, with particular emphasis on chronic organ-level disorders tied to aberrant cellular force generation.

Currently, there is a level of healthy skepticism in the field of *in vitro* models which dictates that higher-order cellular organization is a requirement if the said *in vitro* models are to to be physiologically relevant. This current thinking extends into force biology as well, where there is a lack of agreement regarding the overall usefulness of single-cell contractility measurements in the context of drug discovery and drug testing. While animal models or possibly next-generation organ-on-a-chip models will continue bridging discovery-stage findings to clinical studies by way of preclinical validation, it is clear that cells individually possess the molecular machinery necessary for generating force, and therefore – we believe – organ-level force generation could

rationally be deconstructed into the collective contributions of the many individually contracting cells comprising the organ. We, thus, expect that statistically significant analysis of force generation at the cellular level, and of the effects of small molecules, genes, or other agents on single-cell contractility, to have valuable implications on our understanding of organ-level force generation, and on drug development for diseases occurring at level of the organ.

In support of this rationale, this chapter provides novel data that directly ties cellular level force generation, as measured by our FLECS platform, to force-related pathophysiology at the organ-level, and demonstrates a bidirectional parallelism in the single-cell and *in vivo* responsiveness to both contractile agonist and antagonists. In particular, we show that pro-contractile asthmatic agonists known to induce bronchoconstriction in patients also induce rapid shortening of single airway smooth muscle cells, and further, that a long-acting beta agonist comprising the standard treatment regimen for many asthmatics reverses this single-cell shortening in a dose-dependent manner. We also demonstrate that a novel therapeutic strategy for inducing bronchodilation by selective PI3K inhibition, which we first verify in a precision-cut lung slices, takes effect at the single-cell level. Taken together, these data indicate that in the case of airway bronchoconstriction, the pathophysiology originates with force generation at the single-cell level. We expect a strong link between single-cell and organ level force generation to exist for other conditions as well.

Introduction

Asthma, a disorder characterized by airway inflammation and hyperresponsiveness, globally contributes to substantial morbidity and mortality[1]. Bronchodilators may provide either

rescue-level treatment or chronic management therapy by acting to reverse airway smooth muscle (ASM) shortening and dilating airways. Although these agents are effective in preventing or reversing obstruction of airflow, there are a number of limitations facing these therapeutics. These include further increases in sensitivity to agents causing bronchoconstriction[2], receptor tachyphylaxis[3,4] and non-uniform responses attributed to polymorphisms in β_2-adrenergic receptors (β_2AR)[5]. The volume of patients with poor asthma management continues to indicate a significant unmet need for novel approaches, and perhaps new molecular pathways, for controlling asthma-related symptoms and morbidity[5,6].

Phosphoinositide-3 kinases (PI3K), first discussed in the previous chapter, constitute a family of kinases that phosphorylate membrane phospholipids, and as we and others have shown, have a clear role in force-generation during phagocytosis. Prior work has also shown that PI3K has roles in smooth muscle contractility, in particular, that PI3K inhibition ahead of stimulation with pro-contractile agonists attenuated contraction of smooth muscle, as well as calcium flux[7], and other contractile signaling pathways[8,9]. In this study, we posit that PI3Kδ inhibition directly dilates human small airways. In this collaborative work, we use human precision cut lung slice (hPCLS) – isolated but intact lung tissue- to first show that reversal of carbachol-induced bronchoconstriction with PI3K inhibitors or a selective ROCK inhibitor (Y27632)[10] is comparable to that induced by formoterol, a β_2AR agonist. We follow up on this organ-level analysis using FLECS cytometry to show that the shortening of individual airway smooth muscle cells induced by pro-contractile agonist bradykinin can be robustly attenuated by a commonly prescribed long acting beta agonist at the single-cell level. We then validate the contractility-attenuating effects of PI3K inhibition, suggested by the hPCLS experiment, at the single-cell level, and show that the rescue effect of PI3K inhibition is quantitatively comparable to that of formoterol.

Methods

Materials

Carbachol (CCH - carbamoyl choline chloride), formoterol (formoterol fumarate dihydrate), bradykinin (bradykinin acetate salt) were purchased from Sigma Aldrich (St. Louis, MO). LY294002 was purchased from Cayman Chemical Company (Ann Arbor, MI) and CAL-101 was purchased from Selleck Chemicals (Houston, TX). Y27632 was purchased from Enzo Life Sciences (Farmingdale, NY).

Isolation and culture of human airway smooth muscle

HASM cells were derived from tracheas obtained from the National Disease Research Interchange (NDRI) (Philadelphia, PA) and from the International Institute for the Advancement of Medicine (IIAM) (Edison, NJ). HASM cell culture was performed as described previously[11]. The cells were cultured in Ham's F-12 medium supplemented with 10% FBS, 100 U/ml penicillin, 0.1 mg/ml streptomycin, and 2.5 mg/ml amphotericin B, and this medium was replaced every 72 hr. HASM cells in subculture during passages 1–5 were used, because these cells retain the expression of native contractile protein, as demonstrated by immunocytochemical staining for smooth muscle actin and myosin[12]. The HASM cells were derived from donors with fatal asthma or from donors who were age- and gender-matched without asthma.

Generation of PCLS and airway dilation assays

Human precision cut lung slices (hPCLS) were prepared as previously described[2]. Briefly, whole human lungs from non-asthma donors were dissected and inflated using 2% (wt/vol) low melting point agarose. Once the agarose set, the lobe was sectioned, and cores of 8 mm diameter were made. The cores that contained a small airway by visual inspection were sliced at a thickness of 350 μm (Precisionary Instruments VF300 Vibratome, Greenville, NC) and collected in wells containing supplemented Ham's F-12 medium. The cores generated were randomized as to the location in the lungs they were derived from, so the slices generated came from throughout the lungs and not one specific area. This generated variation in the slices both from within a single donor, but also accounts for variation from donor to donor. Suitable airways (≤1-mm diameter) on slices were selected on the basis of the following criteria: presence of a full smooth muscle wall, presence of beating cilia, and unshared muscle walls at airway branch points to eliminate possible counteracting contractile forces. Each slice contained ~98% parenchyma tissue; hence, all airways situated on a slice had sufficient parenchymal tissue to impart basal tone. Slices containing contiguous segments of the same airway served as controls and were incubated at 37°C in a humidified air-CO_2 (95-5%) incubator. Sections were rinsed with fresh media 2-3 times on *day 1* and *day 2* to remove agarose and endogenous substances released that variably confound the production of inflammatory mediators and/or alter airway tone[2]. Airways from each core were randomized to the different treatment groups prior to the start of the experiment. Airways were constricted to a dose response of carbachol (10^{-8} – 10^{-5} M), then dilated to one of the following (10^{-11} – 10^{-4} M): diluent (DMSO), formoterol, isoproterenol, LY294002, CAL-101 or Y27632. DMSO alone did not induce airway dilation at the concentrations tested (data not shown).

To assess luminal area, lung slices were placed in a 12-well plate in media and held in place using a platinum weight with nylon attachments. The airway was located using a microscope (Nikon Eclipse; model no. TE2000-U; magnification, ×40) connected to a live video feed (Evolution QEi; model no. 32-0074A-130 video recorder). Airway luminal area was measured using Image-Pro Plus software (version 6.0; Media Cybernetics) and represented in units of square micrometers[2]. After functional studies, the area

of each airway at baseline and at the end of dose the response was calculated using Image-Pro Plus software. Maximal airway dilation (E_{max}), sensitivity of the airways to contractile agonist - log of the effective concentration to induce 50% airway dilation (Log EC_{50}), and the integrated response to dilatory agonist – area under the curve (AUC) were calculated from the dose response curves generated. The hPCLS were derived from non-asthma donors. Airway dilation was calculated as the per cent reversal of maximal bronchoconstriction.

Contractility measurements of isolated human airway smooth muscle cells

FLECS substrates were prepared as described in chapter 3. Briefly, soft silicone elastomer films were micro-patterned with fibronectin and fluorescent fibrinogen in uniform 'X' shapes (70 μm diagonal by 10 μm thick). These substrates were prepared using a robust sacrificial approach to facilitate covalent embedding of the ECM molecules into the film as previously described[13]. The non-patterned regions were blocked using 0.5% Pluronic F-127 preventing cell adhesion outside of the fibronectin patterns. Isolated cells adhering to these 'X' –shaped micro-patterns exerted tonic traction forces or stimulated contraction forces resulting in deformations of the micro-patterns (Fig. 4-2a). Dimensions of contracted micro-patterns, which correspond directly to the force applied on them by adhered cells, relative to the original unperturbed dimensions were used to assess cellular contractile responses to the tested compounds. Prior to stimulation, isolated HASM cells were seeded on the soft substrates, allowed to adhere and serum-starved for 48 hr. Cells were then stimulated with bradykinin (10^{-6} M, 15 min) to induce contraction of the cell, and treated with 0.5% v/v DMSO in medium (control) or formoterol or CAL-101 (10^{-10}, 10^{-7}, or 10^{-4} M). Each condition was performed in triplicate wells for a non-asthmatic HASM cell line. The fluorescent micro-patterns were imaged immediately before stimulation with bradykinin for a

baseline reading, and approximately 15 minutes after administration of the treatments. Cell nuclei were stained with Hoechst 33342 prior to imaging and only the patterns co-localized with exactly one stained nucleus were used in the analysis. Following these studies, MATLAB was used to measure each individual pattern and generate distributions of the relative contractions of the patterns for each treatment case. Using the medians of these distributions, the relative relaxation was calculated as the percent reversal from maximal contraction (Fig. 4-2b). Bradykinin was administered at 10^{-4} M in the movies summarized in Fig. 4-3, but lowered to 10^{-6} M in the experimental data shown.

Statistical analysis

Graph Pad Prism software was used to determine statistical significance evaluated by a paired Students *t*-test for two groups or analysis of variance (ANOVA) for multiple groups. *P* values of <0.05 were considered significant. For lung slice analysis (Fig. 4-1), slices were not compared to themselves for each treatment group so non-parametric ANOVAs (Kruskal-Wallis test) were used for data analysis, with Dunn's post-test. Non-parametric Mann Whitney tests were used after ANOVAs established significance to compare each inhibitor to formoterol, and conditions within a given inhibitor. Single cell contractile data was analyzed by two-tailed students t-tests. SigmaStat and Graphpad Prism programs were used in statistical analyses.

Results

PI3K inhibition reverses carbachol-induced constriction of human small airways in a dose-dependent manner.

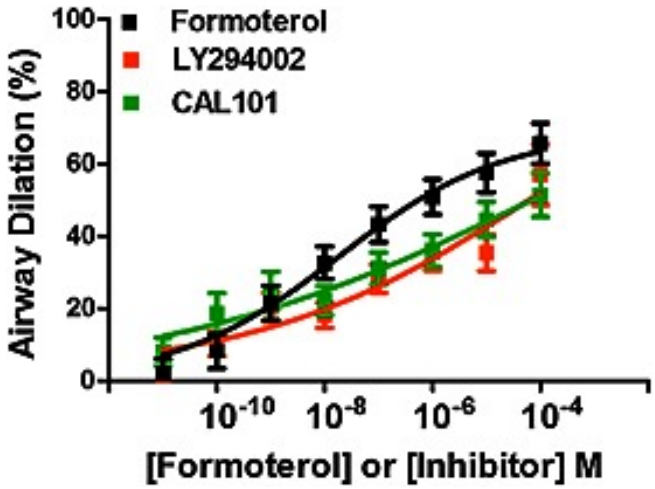

Figure 4-1: PI3K inhibition reverses carbachol-induced bronchoconstriction in a dose-dependent manner in hPCLS.

Airways were preconstricted to carbachol (10−8–10−4 M) prior to dilation to LY294002, CAL-101 or formoterol (10−11–10−5 M). Maximal airway dilation (Emax, ANOVA, P = 0.03) and AUC (P = 0.004) for each inhibitor was significantly different than formoterol-induced dilation. Data are representative of n ≥ 5 donors, 26–33 slices per condition, with bars representing mean + SEM.

To determine if inhibition of PI3K dilates pre-contracted small human airways, PCLS were prepared from donors with no history of lung disease. PCLS airways were treated with carbachol to induce bronchoconstriction and then treated with increasing doses of LY294002, CAL-101, or formoterol to evaluate airway dilation (Fig. 4-1). Both LY294002 and CAL-101 markedly reversed was not to the same level as to the β agonist formoterol. Further, we evaluated ROCK and PI3K inhibitor-induced airway dilation and detected responses as early as 5-10 min, which

were sustained through 30 min following a single dose of inhibitor. Pretreatment with these inhibitors had little effect on carbachol-induced calcium transients in HASM cells (data not shown). These data indicate that inhibition of the p110 subunit of PI3K, and specifically of p110δ is bronchodilatory and that the mechanism likely involves events distal to the activation of GPCRs mediating bronchoconstriction in human airways.

PI3K inhibition reverses bradykinin-induced shortening of single HASM cells.

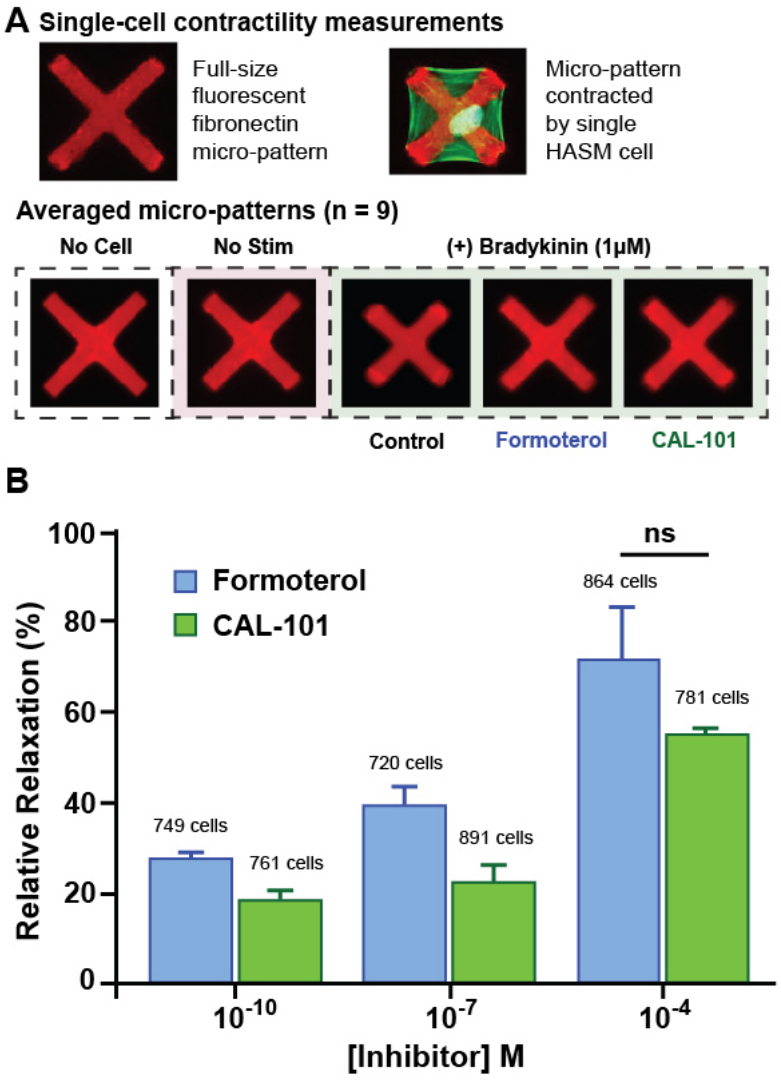

Figure 4-2: PI3K inhibition reverses bradykinin-induced shortening in

isolated HASM cells.

Cells were stimulated to contract with bradykinin (10^{-6} M) prior to treatment with 0.5% v v^{-1} DMSO control, or formoterol or CAL-101(10^{-10}, 10^{-7} and 10^{-4} M). (A) Representative images of fibronectin micro-patterns on ultra-soft silicone elastomer films. Top: typical non-contracted and contracted micro-patterns. HASM F-actin is shown in green. Bottom: averaged patterns for each treatment case generated from one pattern taken from each of the nine imaging sites used per sample. (B) Quantification of cell relaxation to formoterol or CAL-101 (10^{-10}, 10^{-7} and 10^{-4} M) following bradykinin contraction. Bars represent mean of the triplicates + SEM, with each column representing ≥720 cells analyzed per triplicate well measurement from a single donor. $P < 0.05$ was considered significant.

To determine if inhibition of PI3K reverses contractile agonist-induced shortening at the single-cell level, cells were seeded onto FLECS substrates, stimulated with bradykinin to induce shortening and then treated with increasing doses of CAL-101 or formoterol. Relaxation of the cells was evaluated, and we show that CAL-101 reversed bradykinin-induced shortening comparable to maximal levels induced by formoterol (Figs. 4-2 and 4-3).

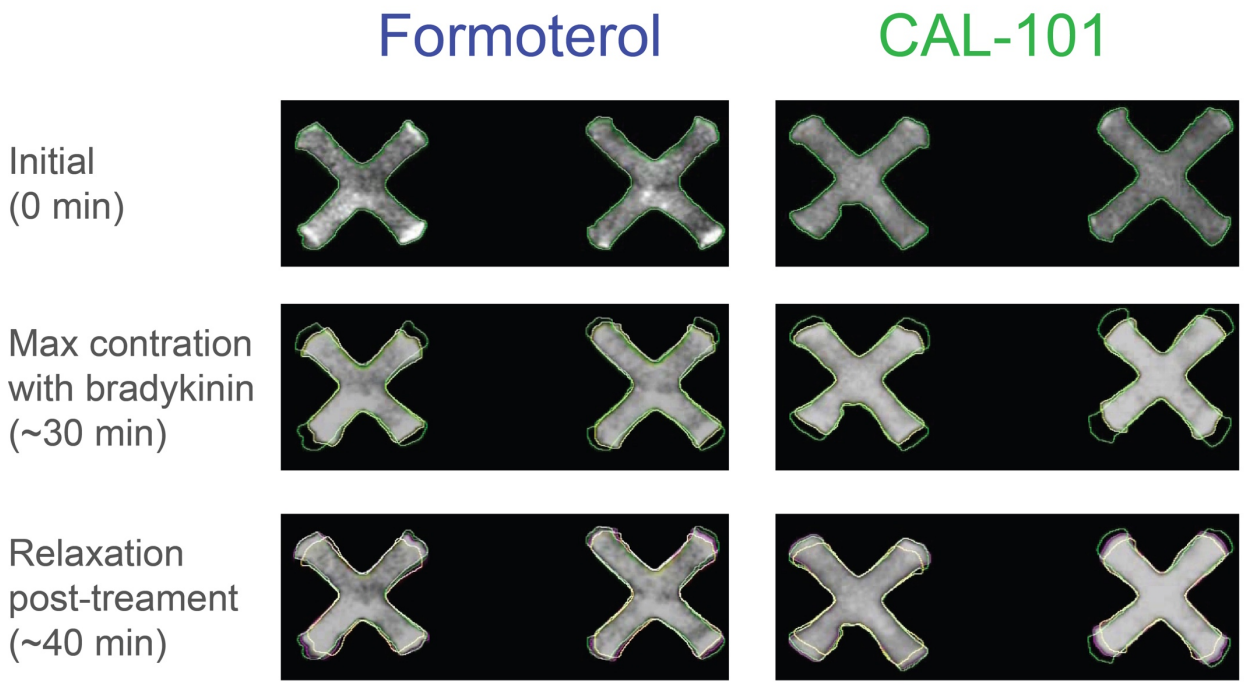

Figure 4-3: Live monitoring of pharmacological reversing of bradykinin-induced shortening in isolated HASM cells with formoterol and CAL-101. *Representative frames from videos taken from the experiments described in Fig.4-2. Individual adhered HASM cells already at steady-state are stimulated to contract with 10^{4}M bradykinin. After approximately 30 mins, they reach a maximal contracted state. At this point, a treatment of 10-4 M formoterol or bradkykinin initiated a reversal in cell contractility as quickly as 10 mins in.*

Conclusion

In this work, we have shown that single-cell contractility data obtained using the FLECS force-phenotyping system is highly relevant to *in vivo* physiology of airway obstruction disease. As in the previous chapter, we first showed that asthmatic pro-contractile agonist bradykinin,

which is among the molecular triggers of bronchoconstriction in patients, also induces a shortening effect in individual HASM cells. The significance of this finding is that it distills some of the complexity of the cascade of events leading to bronchoconstriction down to the cellular level, where experimentation, screening, and general analysis is simpler, higher-throughput, and does not require extensive approvals.

Next, we showed that formoterol, a treatment belonging to the class of long-acting beta agonists (LABAs) that is commonly used in patients, produced a restorative effect on bradykinin-contracted single HASM cells. This indicates that such rescue treatments may in some cases take effect at the single-cell level, thus inviting further use of this cellular *in vitro* FLECS assay for drug discovery for asthma management therapies, and perhaps other disorders pertaining to aberrant smooth muscle cell contractility.

Lastly, we used the FLECS system to corroborate the finding that a selective PI3K inhibitor, CAL-101, reverses bronchoconstriction of organ-like precision cut lung slices, and that this restorative effect, too, takes place at the individual cell level. Further, we observe that at that cellular level, PI3K inhibition appears to have very comparable potency to formoterol.

We conclude this chapter by underscoring the optimism this data provides for the use of such *in vitro* disease models and screening systems as the FLECS force-phenotyping platform and the clinical and commercial impact our system could have on drug development.

Bibliography

1. Vijverberg SJ, Hilvering B, Raaijmakers JA, Lammers JW, Maitland-van der Zee AH, Koenderman L (2013). Clinical utility of asthma biomarkers: from bench to bedside. *Biologics : targets & therapy* 7**:** 199-210.

2. Cooper PR, Lamb R, Day ND, Branigan PJ, Kajekar R, San Mateo L*, et al.* (2009). TLR3 activation stimulates cytokine secretion without altering agonist-induced human small airway contraction or relaxation. *American journal of physiology. Lung cellular and molecular physiology* 297**:** L530-537.

3. 3. Kraan J, Koeter GH, vd Mark TW, Sluiter HJ, de Vries K (1985). Changes in bronchial hyperreactivity induced by 4 weeks of treatment with antiasthmatic drugs in patients with allergic asthma: a comparison between budesonide and terbutaline. *The Journal of allergy and clinical immunology* 76**:** 628-636.

4. 4. Cheung D, Timmers MC, Zwinderman AH, Bel EH, Dijkman JH, Sterk PJ (1992). Long-term effects of a long-acting beta 2-adrenoceptor agonist, salmeterol, on airway hyperresponsiveness in patients with mild asthma. *The New England journal of medicine* 327**:** 1198-1203.

5. Drazen JM, Silverman EK, Lee TH (2000). Heterogeneity of therapeutic responses in asthma. *British medical bulletin* 56**:** 1054-1070.

6. Barnes PJ (1995). Beta-adrenergic receptors and their regulation. *American journal of respiratory and critical care medicine* 152**:** 838-860.

7. Jiang H, Abel PW, Toews ML, Deng C, Casale TB, Xie Y*, et al.* (2010). Phosphoinositide 3-kinase gamma regulates airway smooth muscle contraction by modulating calcium oscillations. *The Journal of pharmacology and experimental therapeutics* 334**:** 703-709.

8. Su X, Smolock EM, Marcel KN, Moreland RS (2004). Phosphatidylinositol 3-kinase modulates vascular smooth muscle contraction by calcium and myosin light chain phosphorylation-independent and -dependent pathways. *American journal of physiology. Heart and circulatory physiology* 286**:** H657-666.

9. Wang Y, Yoshioka K, Azam MA, Takuwa N, Sakurada S, Kayaba Y*, et al.* (2006). Class II phosphoinositide 3-kinase alpha-isoform regulates Rho, myosin phosphatase and contraction in vascular smooth muscle. *The Biochemical journal* 394**:** 581-592.

10. Ishizaki T, Uehata M, Tamechika I, Keel J, Nonomura K, Maekawa M*, et al.* (2000). Pharmacological properties of Y-27632, a specific inhibitor of rho-associated kinases. *Molecular pharmacology* 57**:** 976-983.

11. Panettieri RA, Murray RK, DePalo LR, Yadvish PA, Kotlikoff MI (1989a). A human airway smooth muscle cell line that retains physiological responsiveness. *The American journal of physiology* 256**:** C329-335.

12. Panettieri RA, Jr., Murray RK, DePalo LR, Yadvish PA, Kotlikoff MI (1989b). A human airway smooth muscle cell line that retains physiological responsiveness. *Am. J. Physiol. Cell Physiol.* 256**:** C329-C335.

13. Tseng P, Pushkarsky I, Di Carlo D (2014). Metallization and biopatterning on ultra-flexible substrates via dextran sacrificial layers. *PloS one* 9**:** e106091.

Chapter 5:

Towards high-throughput functional phenotypic screening of cellular force generation

In Chapter 1, we highlighted the need for a tool that can provide access to cellular force generation and that could be used by both biological researchers and by industrial pharmaceutical companies to better understand force biology and to have a means to begin discovering and developing therapies that work to correct abnormal or malfunction force generation. We then outlined five specific requirements that such a tool must meet if it is to provide real value to both communities. In Chapter 2, we described an enabling microfabrication approach which we then built upon in Chapter 3 to develop the FLECS force-phenotyping system. In particular, we demonstrated how we satisfied each requirement we set forth.

The FLECS system confers tight control over many cellular parameters through the implementation of cell micropatterning. In this way, cell-cell contact, cell spread area, and localization of force is tightly controlled. The signal is also shown to be robust, since we are directly measuring geometric changes in cell-adhered micropatterns that could not feasibly be produced in any other manner. We achieve high-throughput since large arrays of cell-adhesive micropatterns enable the simultaneous analysis of extremely high cell counts. Furthermore, the simple calculation that is to be made for each cell can be well-defined algorithmically, and executed using a machine, thus enabling semi-automation of the procedure. Next, sensitivity is conferred by tuning the pattern sizes and substrate stiffnesses to maximize the dynamic range of the system for each specific cell type or behavior of interest. Finally, we demonstrate a straightforward procedure for implementing the FLECS substrates in a wellplate format that can directly integrate into laboratory automation workflows.

We then demonstrated several valuable use-cases in which FLECS can facilitate new research focusing on force biology, including phagocytic forces, smooth muscle contractility and its correlation with molecular markers, and even cardiac contractility. This body of work demonstrates the kind of utility FLECS can provide to the research community.

In Chapter 4, working with a fully qualified system, we demonstrate the value that single-cell contractility measurements can provide, and the direct link they hold to physiology occurring *in vivo*. In this final chapter, we apply the FLECS platform to serve the drug developer community by realizing its high-throughput screening and drug discovery potential.

High-throughput screening in drug discovery

Starting in the late 1980s and early 1990s, the marriage of laboratory automation and drug discovery efforts spawned a new approach known as high-throughput screening (HTS)[1]. In this approach, automated equipment that was designed to perform routine laboratory functions in experiments continued to see improvement and was implemented to run large-scale drug screens at throughputs vastly eclipsing what was previously possible. In particular, robotics that could load wellplates, dispense compounds, transfer plates between incubators and imaging systems, and high-content imaging systems themselves became the workhorses in drug discovery. HTS approaches, where the speed and quantity became the focus, has continued to grow industrially and today, there exist dozens of large manufacturers, and their distributors, that constantly innovate on these products to improve precision, longevity and performance in general. In addition, large communities and societal organizations that promote education of screening and laboratory automation act to serve as valuable resources to the field.

In simplest terms, the HTS approach can be divided into two general strategies: (1) Target-

based and (2) phenotypic screening.

Target-based screening

Target-based screening takes the approach of first identifying a "druggable" molecular target, and then screening for compounds that "hit" that target. Target identification can be done in a number of ways, but generally involves identifying a robust physiological link between a cellular component and a disease process. Next, the general mechanism by which the target is linked to the disease process should be described so it is known what modification must be made to the target to produce a therapeutic effect. If this information is available, the screen proceeds by looking for compounds with high-affinity to the known targets. For years, this appeared to be the strategy of choice in the community. However, this approach could potentially exhaust a given target, and will not be useful in identifying new targets.

Phenotypic screening

Phenotypic screening uses cell-based assays to identify compounds that objectively act to modify a cellular phenotype or observable trait or process in whole, live cells. In this approach, if the test compound modifies a phenotype, this is seen directly, unlike with target-based screening. Importantly, phenotypic screens can be very useful in bolstering the target-based approach since it is capable of identifying whole new classes of targets and pathways, which can be funneled back into the target-based workflow. The main challenges facing phenotypic screening are the need for a robust assay that clearly conveys the phenotype of interest, and one that can be scaled to meet the HTS workflow.

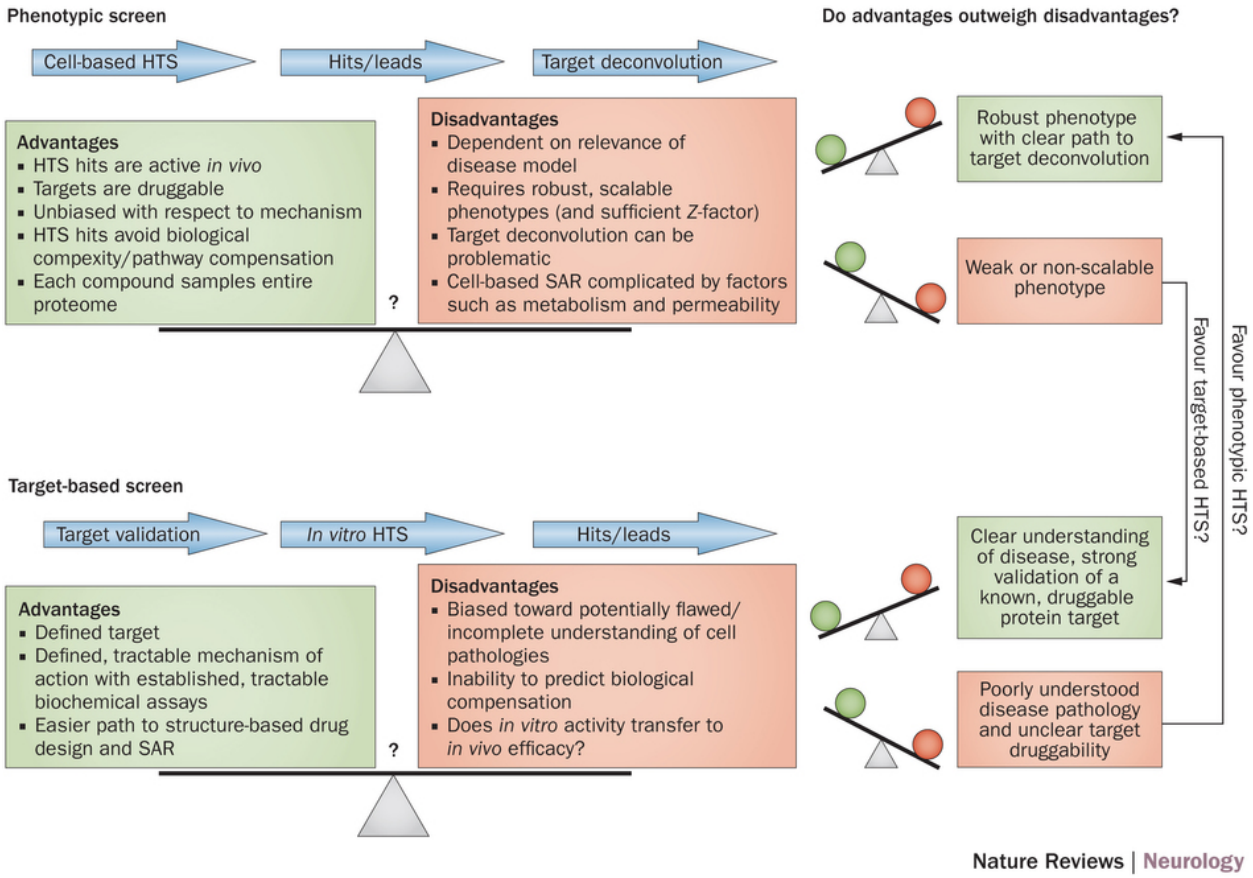

Figure 5-1: Phenotypic vs Target-based screening approaches

Adapted from ref 2 with permission for Nature Publishing Group.

Both screening approaches have unique advantages as well as unique obstacles that must be overcome for success. For a given indication, the decision of which strategy to implement must be made after careful consideration of the both the knowledge available surrounding a potential target(s), and the strength and robustness of a potential assay(s..

Notably, given the balance between the advantages, ease of use, and productivity of the two strategies, a 2012 analysis revealed that *phenotypic assays have been more successful for small*

molecule first-in-class medicines than target-based assays, due to their unbiased identification of new MMOAs[3]. As detailed in Chapter 1, the resistance and desensitization to treatment associated with asthma and hypertension, two of the most common high-burden chronic diseased associated with aberrant force generation, create a pressing need for new classes of medicines. Furthermore, as we have shown in Chapters 3 and 4, the FLECS assay has been developed to possess all of the requisites of a successful phenotypic screening platform. Here, we conclude this work by briefly showing the progress we have made in implementing FLECS in a true HTS workflow.

Pilot HTS Screen

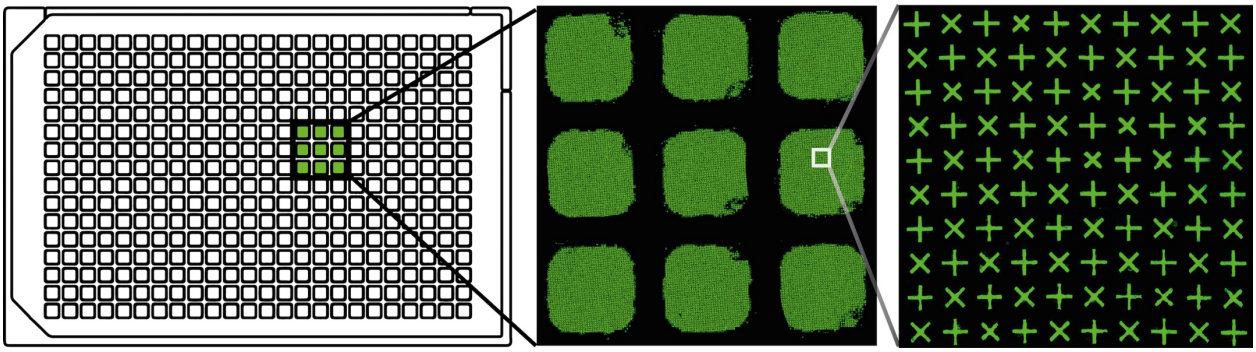

Figure 5-2: Schematic and fluorescent images of FLECS-functionalized wells on a 384-wellplate

A fully FLECS- functionalized 384-wellplate that is prepared in the same single-step process as a 96 well-plate. This implementation is used to conduct HTS operations for the discovery of therapeutic mediators of cellular contractility using laboratory automation.

First, we scaled the FLECS wellplate from a 96-well to a 384-well implementation (Fig. 5-2).

Using these consumables, we seed primary human airway or vascular smooth muscle cells, giving them 24 hours to achieve steady-state contractions. Next, using an automated workflow, we dispense 384 compounds, including controls, into the plates, and finally, image the cells at a later time-point to observe any effects on their contractility. A pilot screen for mediators of airway smooth muscle cell contractility is shown in Fig. 5-3.

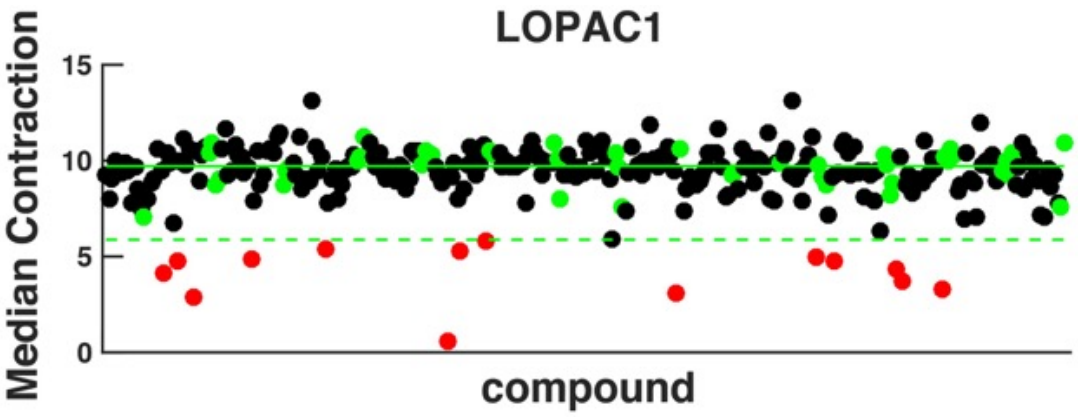

Figure 5-3: Results from a pilot screen of HASM contractility using LOPAC 1

LOPAC 1260 – Library of Pharmacologically Active Compounds – consist of FDA approved and well-characterized compounds, and is often used to validate screening platforms. Consisting of 1260 compounds, the library is designed to be implemented in just four separate 384-wellplates. This figure shows the results of screening using the first of the four wellplates comprising LOPAC 1260 – "LOPAC 1." Each point represents a well in the wellplate. Green points indicate control wells and red indicate hits, defined by the standard three-standard deviation cutoff.

In this LOPAC 1 screen, we identified compounds with known molecular mechanisms of action (MMOA) on the contractile pathway such as Y-27632 (ROCK inhibitor) and DPO-1 (K-channel blocker), as well unexpected compounds, indicating the potential of this screening methodology to uncover new MMOAs. Moving forward, we will continue applying FLECS as a phenotypic screening assay in HTS workflows, to support the efforts of developing novel therapies for diseases resulting from malfunctioning cellular force generation. Hits obtained in the initial screen will be validated with rigorous follow-up including IC50 characterization and determination of therapeutic index. Toxicity counter-screens on cardiac cells will also be performed. As we have demonstrated in Chapters 3-5, the FLECS force-phenotyping platform has the potential to strengthen drug development efforts focusing on the restoration of normal cellular force generation at the i) high-throughput screening, ii) lead generation, and iii) toxicity screening stages.

Bibliography

1. Macarron, R. Critical review of the role of HTS in drug discovery. *Drug Discovery Today* **11,** 277–279 (2006).

2. Khurana, V., Tardiff, D. F., Chung, C. Y. & Lindquist, S. Toward stem cell-based phenotypic screens for neurodegenerative diseases. *Nature Reviews Neurology* **11,** 339–350 (2015).

3. Swinney, D. C. Phenotypic vs. target-based drug discovery for first-in-class medicines. Clin. Pharmacol. Ther. 93, 299–301 (2013).